3D FE Seismic analysis of a monopile-supported offshore wind turbine in a non-liquefiable soil deposit

Vlad Văcăreanu

Thesis committee
Assistant Prof. **Federico Pisanó,** Prof. **Ken Gavin,** Assistant Prof. **Apostolos Tsouvalas,** M.Sc. **Evangelos Kementzetzidis**

TU Delft Delft University of Technology

Challenge the future

3D FE seismic analysis of a monopile-supported offshore wind turbine in a non-liquefiable soil deposit

Vlad Vacareanu

Committee members

Assistant Professor Federico Pisanò

Professor Ken Gavin

Assistant Professor Apostolos Tsouvalas

M.Sc. Evangelos Kementzetzidis

A thesis presented for the degree of
Master of Science

Geotechnical Engineering
Tu Delft University of Technology
Netherlands

29.01.2019

Abstract

This work presents a numerical study on the dynamic response of monopile-supported offshore wind turbines (OWTs) under seismic loading conditions. For this purpose the realistic design of a 8 MW OWT is considered as ideally located in a layered, non-liquefiable site off the coast of Japan. This choice allowed to employ available site characterisation and seismic records from the well-known Japanese KiK-net.

Modelling highlights are reported about the development of a dynamic, fully 3D FE model, in which the soil is described as a water-saturated elasto-plastic medium. The well-established SANISAND bounding surface formulation is adopted to reproduce the hydro-mechanical cyclic response of coarse-grained materials at the site considered, with model parameters derived via back-analysis of available seismic records.

The seismic performance of the OWT is studied in relation to real seismic input of different intensity, accounting for the effect of combined horizontal and vertical components. Although in a non-liquefiable site, pore pressure effects are clearly visible in the simulation results and affect the observed interaction between soil and foundation. The likely coexistence of seismic and SLS wind/wave loading is also considered for completeness.

The numerical study leads to some interesting conclusions regarding the interaction between monopile head stiffness and seismic/cyclic soil response, and its impact on the motion and strength mobilisation along the OWT structure. In particular, some fundamental differences between the dynamics induced by wind/wave loading and seismic input are put in evidence.

More generally, it is also shown how existing analysis approaches developed in the context of earthquake geotechnical engineering prove still suitable to support modern offshore wind developments in seismically active regions.

Acknowledgements

The research described in this thesis could not have been realized without the contribution of many people. First of all, I would like to express my special appreciation to Federico Pisanò for his expert guidance, his insightful comments, the fruitful conversations, his continuous support and interest throughout all of the steps of this work. His unending willingness to produce valuable research and his understanding during the misfortunes met, have been catalytic.

Secondly, I would like to express my gratitude to Evangelos Kementzetzidis, who, even though being a first year PHD, proved to be extremely knowledgeable in the field of computation soil dynamics and provided me with tremendous help during the thesis. He has been like a daily supervisor, being only one message away from an office visit whenever I needed it.

I would also like to thank Apostolos Tsouvalas, with whom I have worked closely during the year, being his student assistant in the "Structural Response to Earthquakes" course, and who helped us with his expert insight into structural dynamics every time we ran into trouble.

Additionally, I would like to thank Ken Gavin for his careful guidance and expert advices.

Last but not least, I am deeply grateful to my father who has also contributed to my work based on his years of experience in the field of earthquake engineering and always pushed me further and to my family and friends for always offering me support when things got heavy.

Vlad Vacareanu
Delft, January 2019

Contents

List of Figures

List of Tables

1 Introduction

Recently, climate change has become a hot topic in the scientific community. While a few decades ago environmental sustainability was an unknown term to many, nowadays societies are determined to reduce their carbon footprint.

Due to this, harvesting energy from offshore wind has become a booming industry, with more and more countries taking part in the movement. Europe is still the dominant force in offshore wind, while other continents like America and Asia are starting to consider it a very feasible solution in dealing with the environmental problem aforementioned.

According to WindEurope [1], formerly known as the E.W.E.A. wind accounted for 44% of all new power installations in Europe during H1[2] of 2016. All the OWTs and 97% of those installed in 2015 were founded on large monopile foundations.

One of the most dynamic offshore wind markets at this particular moment is the Asian Market. For this thesis, the focus will be on Japan.

The Carbon Trust [3] emphasizes that Japan is the world's third largest economy and has the second largest electricity market in the OECD (Jones & Kim,2013). Japan is still one of the world's largest CO_2 emitters, mainly due to its concentration of manufacturing industries. Before the Fukushima nuclear disaster, the government's Energy Plan from 2010 was to increase the nuclear share in the electricity mix to about 50% by 2030 (The Japan Times, 2013).

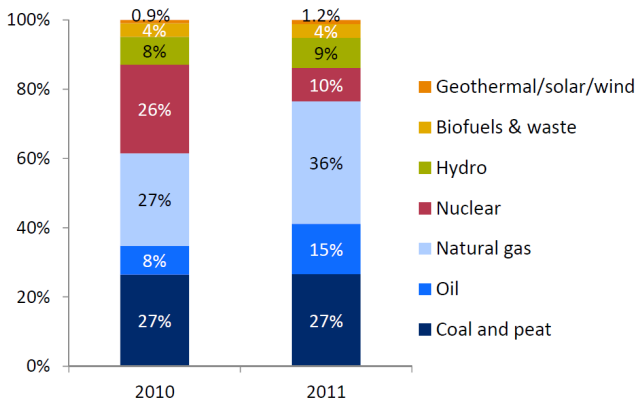

Figure 1: Japan's electricity generation by source (International Energy Agency 2012).

In Figure1 Japan's electricity generation by source is presented. As seen, in 2011, the year of the Tsunami, average electricity generation shifted to almost 70% fossil fuels and 10% nuclear (International Energy Agency, 2012). Since Japan has limited fossil fuel resources, this drastic change in energy supply meant that they had to increase their liquid natural gas imports which amounted to approximately $100 million each day (Franco, 2013).

According to the Ministry of Environment, Japan has an onshore wind power potential of 280GW and 1600GW for offshore potential (Arakawa & Ueda,2012). Hokkaido and Tohoku have the highest offshore wind potential, but the electricity demand in these regions is comparably low, with a very limited interconnection capacity.

Japan Wind Power Association (JWPA) [4] has drawn a Road map for the Wind Power goals in the foreseeable future. The road map can be seen in Figure 2.

[1] www.windeurope.org
[2] First half of a financial year
[3] www.carbontrust.com
[4] http://jwpa.jp/

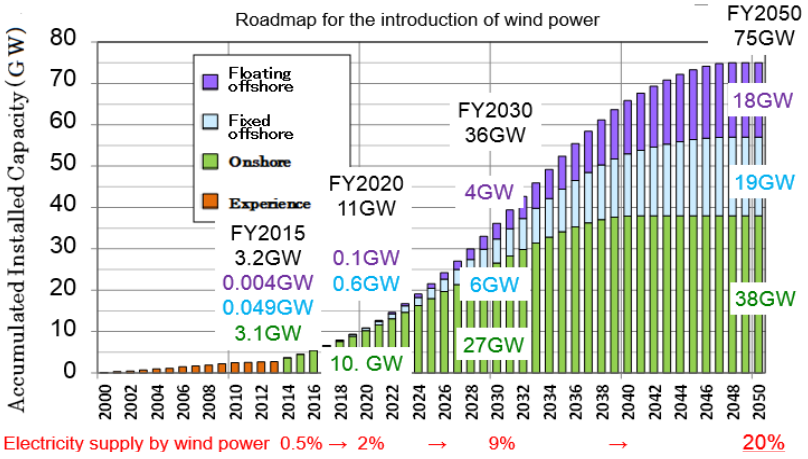

Figure 2: Roadmap for the Wind Power Introduction for Japan, proposed by the JWPA

By means of Figure 2, one can conclude that the Japanese are extremely ambitious regarding their wind energy output in the nearby future, aiming for 20% of energy being wind energy by 2050. Furthermore, this encourages scientific research into the particularities of offshore wind turbines in this area, research to whom this thesis aims to contribute.

1.1 This study

The main aim of this study is to investigate the earthquake response of offshore wind turbines both independently and combined with wind and waves. The research in the field is very sparse, as OWTs so far have been largely employed in non-seismic areas (i.e. North Sea). Nowadays, with offshore wind energy becoming relevant in seismically active areas, such as North America or Asia, seismic investigations need to be undertaken.

Consideration of the seismic loading on OWTs is a relatively new field, as turbines were considered to be insensitive to earthquake excitation due to their long natural periods (Witcher, 2005; Bazeos et al., 2002). Nevertheless, as recently demonstrated by Kourkoulis et al. (2014), while turbines will not fail in ULS, accumulated deflections in SLS can become a problem . The research in the field from a structural engineering point of view is rather sparse, especially for vertical excitation, which has been proven to lead to high accelerations at the top of the tower, where all the fine tuned equipment is located (Kjørlaug, 2013).

Although seismic shaking is not critical in terms of the ultimate limit state, it may lead to substantial accumulation of foundation rotation. Combined with the accumulation of rotation due to cyclic environmental loading, the latter may challenge the serviceability of the OWT, potentially leading to a reduction of its service life (Anastasopoulos and Theofilou, 2016).

It is worth mentioning that although not covered in this work, soil liquefaction hazard is certainly one to consider in OWT foundation design.

Kiyomiya et al. (2002) studied the combination of wind and earthquake loads. The mean wind velocities and large scale earthquake events were simulated from a Weibull distribution. It was proven that there is an extremely low probability of storms and large-scale earthquakes occurring simultaneously. Thus, it was concluded that the use of mean wind velocity was reasonable when combining wind and earthquakes.

This study is able to shed light in all the aforementioned aspects as it introduces a very realistic design of an 8-MW offshore wind turbine, subjected to three ground motions with different PGAs (peak ground accelerations). Displacement and rotation at the monopile head are monitored throughout the analysis. The analysis time coincides with the significant duration of the respective earthquake, plus 10-20 seconds after the motion stops in order to capture the steady state.

Size of OWT The offshore industry is constantly shifting towards larger OWTs (Figure 3). Almost annually the press covers stories about large OWTs setting the record for higher energy production with:

- 5-MW Gamesa turbine in Spain (2014 / monthly production record)[5] ;
- 8-MW MHI Vestas Offshore wind prototype turbine in Denmark (2014 / daily production record)[6] ;
- 9-MW MHI Vestas Offshore wind prototype turbine in Denmark (2017 / daily production record)[7] ;

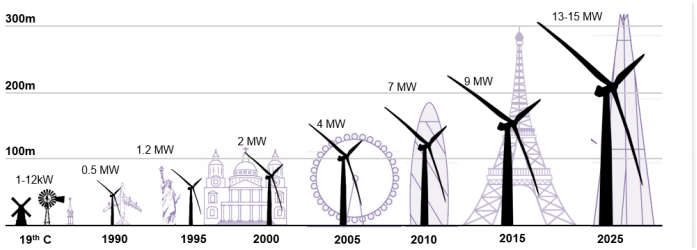

Figure 3: Evolution of wind turbine heights and output, (source: Bloomberg Finance).

For research to remain relevant it has to follow the market trends especially on such technical issues. In that context, the current study examines an 8-MW offshore wind turbine which is sketched in Figure 5.

1.2 Current practice

Katsanos et al. (2016) compiled a state of the art review on wind turbines and seismic hazard.

Commonly, seismic loads are quantified either via response spectra, which are associated with the modal response spectrum analysis (MRSA) or by the time-history representation of earthquake excitations, which are the required input motions for the more accurate method of response history analysis (RHA).

The frequency-based analysis method is sensitive to the damping ratio selected for the structural analysis of wind turbines. When using MRSA, the structural damping is considered identical to the damping ratio of the response spectrum, which is usually taken at 5%. However, this is not the case, especially for parked wind turbines, where the absence of aerodynamic daping led the supporting towers to experience low damping, i.e., 0.5-2.0% of the critical damping (Valamanesh and Myers, 2014b).

On the contrary, the time domain analysis method (RHA) accounts for the actual damping of the system, which consists mainly of the structural, aerodynamic and soil damping, respectively.

Witcher (2005) found that the typical damping ratio of 5%, correspondent to a code-based MRSA, led to a significantly lower response in case of parked wind turbines. The results were

[5] `www.offshorewind.biz`
[6] See footnote 3
[7] `www.mhivestasoffshore.com`

similar to RHA only in the case of operating turbines, where the damping would be indeed around 5%.

Regarding the wind turbines, the interaction between their foundations and the surrounding soil media has been recently identified as a critical aspect for analysis and design purposes, because it has large impact on the dynamic characteristics of the wind turbine, both on land and offshore (Lombardi et al., 2013; Damgaard et al., 2014). More specifically, both the mode shapes and the natural frequencies of a wind turbine may be changed because of the SSI, which further affects the system's damping.

Kaynia (2018) looked into seismic considerations in the design of offshore wind turbines. The paper adresses the use of foundation macro-elements for earthquake response of wind turbines under lateral earthquake excitation and highlights the vulnerability of wind turbines to vertical excitation due to their high vertical natural frequencies. In case of these loading conditions, addition of radiation damping leads to significantly more economical design. Also, it is proven that soil nonlinearity and pore pressure generation can lead to settlement and permanent tilting of offshore wind turbines on mono-bucket foundations. According to the above, the importance of performance-based analyses in seismic design of OWTs is clearly highlighted.

Risi et al. (2018) presented an analytical procedure to evaluate the seismic assessment of steel monopile-supported offshore wind turbines, which is the typical choice in countries affected by earthquakes. Different earthquakes types have been chosen (i.e. crustal, inslab and interface) Both the serviceability limit state, reached when the chord rotation exceeds 0.5 degrees, and the ultimate limit state, reached when either yielding or local buckling were considered. The following conclusions have been reached:

1. The analyzed structural typology is particularly sensitive to extreme crustal and interface records;

2. Higher modes are not negligible, especially if SSI is explicitly modelled;

3. Frequency content of records associated to deformable soil induces an increased seismic fragility with respect to stiffer soil;

4. Lack of proper SSI modeling leads to an overestimation of the seismic capacity of about 60% and 70% for the SLS and ULS, respectively;

5. Local buckling can occur;

6. SLS is frequently reached when subjected to severe strong motions.'

In conclusion, RHA is the superior method of analysis for wind turbines, as their damping ratios are different from the classical code damping ratio. With progress in numerical model efficiency and computational power, the time required to run those should reduce.

For the research presented in this thesis, 3D Finite element simulations have been employed, using time history analyses.

Initially, a soil column was modelled in order to tune the geotechnical parameters. With those modelled, the full 3D simulations involving the soil and the turbine could be run using OPENSEES. A detailed presentation of the procedure is found in the following sections.

2 Integrated soil-monopile-turbine 3D FE modelling

2.1 Low frequency dynamics of saturated soils

2.1.1 Governing equations and numerical solution

Following the work by Zienkiewicz and coworkers (Zienkiewicz et al., 1999), the so-called *u–p* formulation is here adopted to describe the dynamic HM response of the soil around the monopile. The *u–p* approach relies on the assumptions of (i) small soil deformations, (ii) incompressible soil grains, (iii) solid and fluid phases with constant densities and, importantly, (iv) negligible fluid acceleration. While more theoretical background can be found, for instance, in Zienkiewicz et al. (1980); Zienkiewicz and Shiomi (1984); Zienkiewicz et al. (1999), the following conceptual/practical reasons lead to adopt the *u–p* formulation in OWT applications:

– neglecting fluid inertia has proven accurate for low loading frequencies (Zienkiewicz et al., 1980; López-Querol et al., 2008). This limitation, widely accepted in earthquake dynamics (Zienkiewicz et al., 1999), seems still "harmless" in the presence of wind/wave loading (i.e. frequencies lower than 0.5 Hz);

– compared to other mathematical formulations, the FE approximation of the *u–p* model features the least number of nodal unknowns (Zienkiewicz and Shiomi, 1984; Jeremić et al., 2008), positively impacting the computational costs of numerical analysis.

Using standard matrix notation (Helnwein, 2001), the *u–p* differential system couples the global equilibrium of the mixture (Equation (1a)) with the mass balance of the fluid phase (Equation (1b)):

$$\nabla \cdot \left(\boldsymbol{\sigma}' - p\mathbf{1}\right) + \rho\mathbf{g} - \rho\ddot{\mathbf{u}} = \mathbf{0} \tag{1a}$$

$$\dot{\varepsilon}_{vol} + \frac{n}{K_f}\dot{p} + \nabla \cdot \left[\mathbf{k}\left(-\nabla p + \rho_f \mathbf{g}\right)\right] = 0 \tag{1b}$$

where the scalar equation (1b) already includes the momentum balance and the Darcy flow of the fluid. In system (1), $\mathbf{u}$, $\boldsymbol{\sigma}'$, ε_{vol} and n are the displacement, effective stress, volumetric strain and porosity of the soil solid skeleton; ρ is the mass density of the solid–fluid mixture[8]; K_f and ρ_f are the bulk modulus and mass density of the fluid; $\mathbf{k}$ and $\mathbf{g} = [0, 0, g]^T$ represent the permeability tensor and the gravity acceleration field, respectively. Further, ∇ and $\nabla\cdot$ denote gradient and divergence operators, dots stand for time derivatives and $\mathbf{1} = [1, 1, 1, 0, 0, 0]^T$ is the vector representation of the Kronecker second–order tensor. Tensile effective stresses and compressive pore pressure are taken as positive in the analytical formulation, whereas numerical results will be plotted according to the standard Soil Mechanics convention – positive compressive stresses and pore pressure.

Isotropic permeability is assumed throughout this work, so that a single scalar permeability k value can be used:

$$\mathbf{k} = k \begin{bmatrix} 1 & 0 & 0 \\ 0 & 1 & 0 \\ 0 & 0 & 1 \end{bmatrix}, \quad k = \frac{k^{darcy}}{\rho_f g} \tag{2}$$

where the relationship between k (dimension [L^3TM^{-1}]) and the Darcy permeability k^{darcy} employed in standard Soil Mechanics (dimension [LT^{-1}]) is also made explicit. It should also be noted that both $\boldsymbol{\sigma}'$ and ε_{vol} are ultimately functions of the displacement field $\mathbf{u}$, so that $\mathbf{u}$ and p are the only actual unknowns in (1).

[8] $\rho = (1 - n)\,\rho_s + n\rho_f$ and is obtained as the porosity–weighted average of the solid and fluid densities.

2.1.2 FE formulation and technology

The weak forms of Equations (1a)–(1b) can be discretised in space according to the standard Galerkin–FE method (Zienkiewicz and Taylor, 2000), featuring the approximations $\mathbf{u} \approx \mathbf{N}_u \mathbf{d}$ and $p \approx \mathbf{N}_p \mathbf{p}$ for the displacement and the pore pressure fields ($\mathbf{N}_u$ and $\mathbf{N}_p$ are arrays of interpolation functions). The space–discretisation process leads to the following discrete form of system (1) (Zienkiewicz and Shiomi, 1984):

$$\overbrace{\mathbf{M}\ddot{\mathbf{d}}}^{\text{mixture inertiae}} + \overbrace{\int_\Omega \mathbf{B}^T \boldsymbol{\sigma}' d\Omega}^{\text{soil internal forces}} - \overbrace{\mathbf{Q}\mathbf{p}}^{\text{pore pressure forces}} = \overbrace{\mathbf{f}_{u,\Omega}^{ext} + \mathbf{f}_{u,\Gamma}^{ext}}^{\text{mixture external forces}} \tag{3a}$$

$$\overbrace{\mathbf{Q}^T \dot{\mathbf{d}}}^{\text{soil dilation/compaction}} + \overbrace{\mathbf{S}\dot{\mathbf{p}}}^{\text{fluid compressibility}} + \overbrace{\mathbf{H}\mathbf{p}}^{\text{seepage}} = \overbrace{\mathbf{f}_{p,\Gamma}^{ext} + \mathbf{f}_{p,\Omega}^{ext}}^{\text{fluid external fluxes}} \tag{3b}$$

where the relevant matrices/vectors are defined as:

$$\mathbf{M} = \mathop{\mathsf{A}}_{m=1}^{N_{el}} \left(\int_{\Omega^e} \mathbf{N}_u^T \rho \mathbf{N}_u d\Omega^e \right) : \text{mixture mass matrix} \tag{4a}$$

$$\mathbf{Q} = \mathop{\mathsf{A}}_{m=1}^{N_{el}} \left(\int_{\Omega^e} \mathbf{B}^T \mathbf{1} \mathbf{N}_p d\Omega^e \right) : \text{HM coupling matrix} \tag{4b}$$

$$\mathbf{S} = \mathop{\mathsf{A}}_{m=1}^{N_{el}} \left(\int_{\Omega^e} \mathbf{N}_p^T \frac{n}{K_f} \mathbf{N}_p d\Omega^e \right) : \text{fluid compressibility matrix} \tag{4c}$$

$$\mathbf{H} = \mathop{\mathsf{A}}_{m=1}^{N_{el}} \left(\int_{\Omega^e} \boldsymbol{\nabla} \mathbf{N}_p^T \mathbf{k} \nabla \mathbf{N}_p d\Omega^e \right) : \text{permeability matrix} \tag{4d}$$

$$\mathbf{f}_u^{ext} = \mathbf{f}_{u,\Omega}^{ext} + \mathbf{f}_{u,\Gamma}^{ext} = \mathop{\mathsf{A}}_{m=1}^{N_{el}} \left(\int_{\Omega^e} \mathbf{N}_u^T \rho \mathbf{g} d\Omega^e \right) + \mathop{\mathsf{A}}_{m=1}^{N_{el}} \left(\int_{\Gamma^e} \mathbf{N}_u^T \mathbf{t} d\Gamma^e \right) : \text{mixture external force vector} \tag{4e}$$

$$\mathbf{f}_p^{ext} = \mathbf{f}_{p,\Omega}^{ext} + \mathbf{f}_{p,\Gamma}^{ext} = - \mathop{\mathsf{A}}_{m=1}^{N_{el}} \left(\int_{\Omega^e} \boldsymbol{\nabla} \mathbf{N}_p^T \rho_f \mathbf{k} \mathbf{g} d\Omega^e \right) + \mathop{\mathsf{A}}_{m=1}^{N_{el}} \left(\int_{\Gamma^e} \mathbf{N}_p^T \mathbf{q} d\Gamma^e \right) : \text{fluid external flux vector} \tag{4f}$$

In the above definitions, $\mathbf{t}$ and $\mathbf{q}$ denote the vectors of surface traction and flux for the solid and the fluid phases, respectively, $\mathbf{B}$ is the standard matrix of solid compatibility, and A is the matrix/vector assembly operator (Hughes, 1987). In Equation (3a), the internal force term is implicitly associated with the global (tangent) stiffness matrix, while additional viscous damping could be generated either at the constitutive level (viscous soil behaviour) or through numerical Rayleigh damping (Chopra, 1995; Zienkiewicz et al., 1999).

As for the FE technology, the interpolation functions in $\mathbf{N}_u$ and $\mathbf{N}_p$ cannot be chosen arbitrarily, but have to fulfil the so-called *inf–sup* condition (Babuška, 1973; Brezzi, 1974; Pastor et al., 1999). In particular, if the fluid compressibility and the skeleton permeability are small, then "checkerboard" oscillation modes and locking in the pressure field may arise, and thus jeopardise the accuracy/reliability of numerical predictions. Unfortunately, the *inf–sup* condition is

not satisfied by elements allowing for equal-order interpolation of $\mathbf{u}$ and p, unless *ad hoc* stabilisation techniques are adopted. The need for reduced computational costs in 3D computations motivated significant research efforts on the search for stabilised low–order FEs, as documented by Zienkiewicz et al. (1999) and, more recently, Preisig and Prévost (2011); McGann et al. (2012, 2015); Zhang et al. (2016). It should also be recalled that – quoting Preisig and Prévost (2011) – "methods that work well for incompressible elasticity, such as Bbar (Hughes, 1987) or elements that satisfy the LBB-condition, do not guarantee oscillation-free results in the case of poromechanics".

In this work, the low-order eight-node hexahedral element with single-point quadrature (H1-P1ssp) recently proposed by McGann et al. (2015), implemented in OpenSees framework as SSP-BrickUP element, is adopted. H1-P1ssp brick elements feature:

- reduced integration and stabilisation of spurious hourglass modes;
- enhanced assumed strain field for remedying volumetric and shear locking;
- analytical pre–integration for the terms stabilising the solid phase response, resulting in increased computational efficiency;
- linear interpolation functions for both $\mathbf{u}$ and p, and non-residual–based stabilization scheme to cope with undrained/incompressible responses in dynamic HM problems (Huang et al., 2004).

All the items in the above list contribute to the stability, accuracy and efficiency of H1-P1ssp elements, which may be now regarded as a low–order alternative to H2-P1 elements for larger and/or more refined discrete models. The FE results presented in the following will demonstrate the suitability of the H1-P1ssp element formulation, here applied for the first time to the analysis of offshore wind systems.

The aforementioned non-residual–based stabilization produces an additional laplacian term in Equation (3a) (McGann et al., 2015):

$$\mathbf{Q}^T\dot{\mathbf{d}} + \left(\mathbf{S} + \tilde{\mathbf{H}}\right)\dot{\mathbf{p}} + \mathbf{H}\mathbf{p} = \mathbf{f}^{ext}_{p,\Gamma} + \mathbf{f}^{ext}_{p,\Omega}, \quad \text{where:} \quad \tilde{\mathbf{H}} = \mathop{\mathbb{A}}_{m=1}^{N_{el}} \left(\int_{\Omega^e} \boldsymbol{\nabla}\mathbf{N}_p^T \alpha \boldsymbol{\nabla}\mathbf{N}_p d\Omega^e \right) \tag{5}$$

preventing the well-known numerical issues associated with vanishing compressibility and permeability matrices ($\mathbf{S}$ and $\mathbf{H}$ in (4)). On the practical side, setting the numerical coefficient α in (5) corresponds with deciding on the "amount of stabilisation" injected into the discrete system (3): too low or too high α values would result in either ineffective or excessive[9] stabilisation. In what follows, the suggestion by Huang et al. (2004); McGann et al. (2012, 2015) will be taken as a reference:

$$\alpha = \frac{\alpha_0 h_{el}^2}{G_s + \frac{4}{3}K_s} \tag{6}$$

where h_{el} is, heuristically, the average element size within the FE mesh, G_s and K_s are the bulk and shear moduli of the soil skeleton, whilst α_0 is a scalar coefficient in the range of 0.1–0.5.

2.2 Elastic-plastic modelling of cyclic sand behaviour

The numerical analysis of seismically loaded OWT systems is strictly connected to the modelling of cyclic soil behaviour. In the last decades, numerous cyclic soil models have been formulated in the framework of different plasticity theories, including *multi-surface plasticity*, *bounding surface*

[9]Excessive stabilisation is meant as an unrealistic/unphysical attenuation of the pore pressure field, due to the laplacian/diffusive nature of the stabilising term (5).

plasticity, *generalized plasticity*, *hypoplasticity* and *hyperplasticity*. A number of valuable contributions are here worth citing, such as – to mention only a few – Mróz et al. (1978); Prévost (1985); Zienkiewicz et al. (1985); Pastor et al. (1985); Wang et al. (1990); Borja and Amies (1994); Manzari and Dafalias (1997); Gajo and Wood (1999); Puzrin and Houlsby (2001); Papadimitriou and Bouckovalas (2002); Elgamal et al. (2003); Houlsby and Mortara (2004); Dafalias and Manzari (2004); Dafalias et al. (2006); Taiebat and Dafalias (2008); Yang and Elgamal (2008); Andrianopoulos et al. (2010); Pisanò and Jeremić (2014); Taborda et al. (2014); Seidalinov and Taiebat (2014); Tasiopoulou and Gerolymos (2016). Comprehensive overviews on cyclic soil modelling are given, for instance, by Prévost and Popescu (1996), Zienkiewicz et al. (1999), di Prisco and Wood (2012) and Corti et al. (2016).

2.2.1 CSSM modelling of cyclic sand behaviour

The present study relies on the bounding surface plasticity model of (Dafalias and Manzari, 2004) building up on their previous work (Manzari and Dafalias, 1997) which was extended to account for the effect of fabric changes in sand during shear loading.

The main features included in the constitutive model are hereafter summarized, see (Figure 4):

- a stress ratio ($\boldsymbol{r}$), deviatoric ($\boldsymbol{s}$) over hydrostatic (p), controlled formulation, with no "hydrostatic" yield loci present as in (Wang et al., 1990), which is assumed valid in sands as long as no crushing of grains takes place;
- kinematic hardening formulated upon the back-stress ratio ($\boldsymbol{\alpha}$);
- an independent of J_3 deviatoric stress invariant, very small in size and circular on the π plane yield surface;
- the critical state theory of soils is included though the *state parameter* ψ , originally proposed by (Been and Jefferies, 1985; Wood et al., 1994) to account for effective confinement stress level and void ratio effects on sand response;
- bounding M^b surface formulation (Li and Dafalias, 2000; Manzari and Dafalias, 1997) which allows to model the softening response of dense samples but also reverse and cyclic modelling response simulation by moving into stress space as a function of *state parameter* ψ;
- phase transformation surface M^d (Tatsuoka and Ishihara, 1974; Ishihara et al., 1975) introduced to distinguish dilative and compactive soil response, which moves in stress space with reference to the critical state line M according to the *state parameter* ψ;
- softening response is modelled by a stress ratio related hardening modulus which depends on the distance of back stress ratio tensor $\boldsymbol{\alpha}$ and the back stress ratio of the projection of the normal to the yield surface upon the bounding surface $\boldsymbol{\alpha}_\theta^b$;
- a fabric dilatancy tensor $\boldsymbol{z}$ which allows for enhanced contractile response upon reversal of loading after a loading phase which induces dilatancy , due to changes in the fabric of non-cohesive soils, which agrees with observations made by (Nemat-Nasser and Tobita, 1982; Nasser, 1980);

By incorporating CSSM, the model of Manzari and Dafalias, hereafter refereed to as SaniSand2004, is able to describe the response of sands in a variety of effective confinement stresses and states. Accounting for the long time histories analysed in this study, the involvement of CSSM ensures realistic modelling of response in regions around the monopile where high stress ratios ($\boldsymbol{s}$) will be an agent for non-negligible plastic volumetric strains.

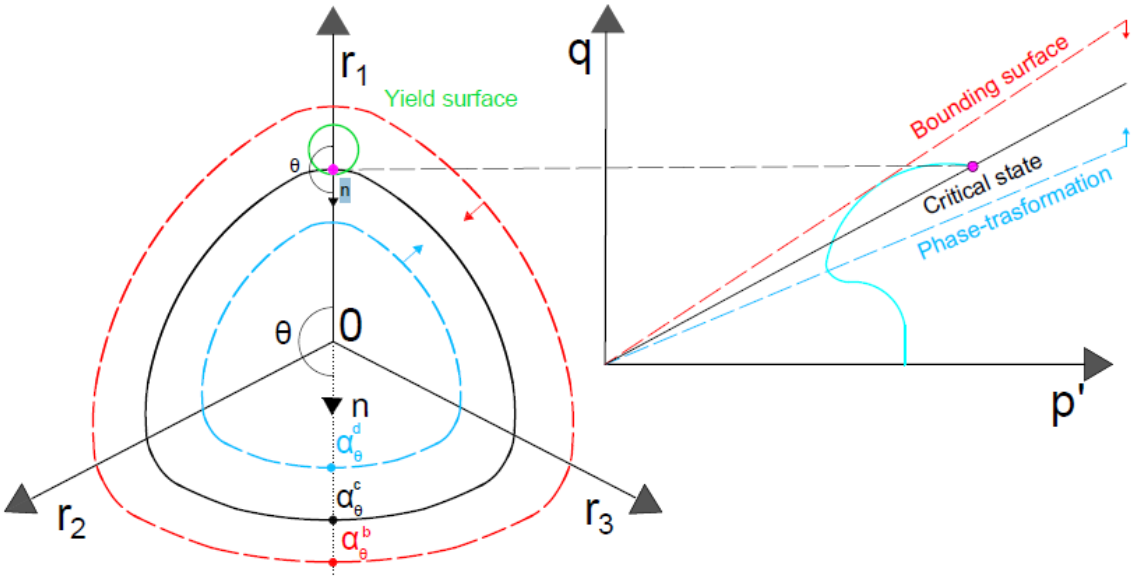

Figure 4: a) Schematic of yield, critical, dilatancy and bounding surfaces on the stress ratio π plane b) a representation of a stress path from an undrained triaxial compression. In the latter, the main effect of dilatancy and bounding surfaces can be seen which in reality are mobile in stress space while in both figures both surface positions do not correspond to the stress state depicted. (Kementzetzidis, 2017)

2.3 Monopile and wind turbine

Structure For research to remain relevant it has to follow the market trends especially on such technical issues. In that context, the current study examines an 8-MW offshore wind turbine (Figure 5). The design was provided by Siemens Wind Power A/S with some details being highly confidential. The development of the structral model was quite intricate including detailed description of the evolution of stiffness across its height.

The structure above the mudline (tower and a part of the monopile) was simulated with approximately 160 elastic Timoshenko beam elements with consistent mass matrices describing the mass of the tower shell. Such elements incorporate the Timoshenko beam theory which accounts for shear deformations. The foundation part was modelled with 8-node hexahedral *SSpBrick*, Stabilized Single point integration elements ($H1ssp$) implemented in OpenSees by Chris McGann, Pedro Arduino, and Peter Mackenzie-Helnwein at the University of Washington. $H1ssp$ elements are stabilized by the inclusion of an enhanced strain field which results in an element free of volumetric and shear locking. Elimination of shear locking allows the user to implement a coarser mesh by improving accuracy in bending dominated problems as in this study.

Local concentrated masses were simulated as lumped modelling equipment and structural masses (flanges, transition piece, boat landing and working platforms, ladders etc.). The RNA (rotor-nacelle assembly) mass was modelled by including the total mass as lumped and the rotational inertia I_M associated with nacelle mass imbalances.

Pile-soil interface The sharp discontinuity in hydro-mechanical properties at the soil-foundation interface needs to be carefully handled in most geotechnical problems, including the numerical analysis of laterally loaded piles. As done by Cuéllar et al. (2014) in the context of OWTs, zero-

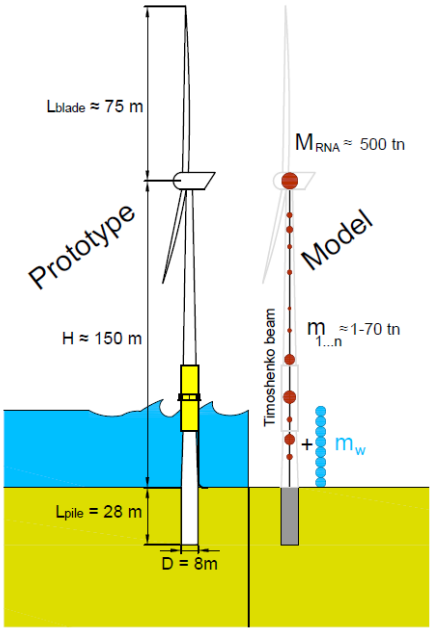

Figure 5: Important information about the OWT simulated in this study (left), along with a depiction of how its was simulated in this numerical analysis (right). (Kementzetzidis, 2017)

thickness interface elements (also termed joint elements) (Goodman et al., 1968; Zienkiewicz et al., 1970) can be introduced at the soil-monopile contact in combination with a suitable shear/tensile behaviour, possibly allowing for soil-steel sliding/detachment. In this work, the soil-monopile interface is treated according to the simpler approach by Griffiths (1985), i.e. by using thin continuum (SSP) elements to model the physical steel-to-soil transition. As this work intends to simulate heavy lateral loading in which the zero-toe kick condition, which was proposed by (WindEnergie, 2005) and critised by (Achmus et al., 2009), is expected to be breached, interface on the pile tip was introduced to simulate a band of intensely plastified soil operating under residual strength. The interface layer lateral to the pile has a thickness of 32cm while the pile tip layer is also 32 cm. A weaker and thus more deformable soil material was assigned for the interface layer by reducing parameters as the elastic stiffness G_0 and the stress ratio of the critical state line by 2/3 and 3/4 respectively.

Damping Viscous damping was introduced into the simulation solely on the structural members (monopile foundation and tower), more analytically:

- Soil's contribution to damping is either though radiation damping (dissipation of waves in an ever-increasing continuum) or hysteretic damping which is an intrinsic material property of the soil. Both damping sources do not require direct implementation as they are introduced either from the geometry and the constitutive model respectively.

- Material damping (steel) was implemented following the provisions of (En, 1991). A damping ratio $\zeta_{steel} = 0.19\%$ is attributed to all steel sections in frequencies between 0.1 and 80 Hz via the rayleigh damping approach.

- Aerodynamic damping is a dominant source of damping in the fore-aft direction during power production. However it is far less significant for parked and feathered rotors (Tarp-Johansen et al., 2009; Valamanesh and Myers, 2014a; Shirzadeh et al., 2013). In case of a

significant earthquake load, one would expect the turbine to be parked to avoid generating extra stresses in the system. In this context, aerodynamic damping was not accounted for in this study.

- Hydrodynamic damping was added according to (Leblanc and Tarp-Johansen, 2010) which in turn was based on (Tarp-Johansen et al., 2009). This study renders the dominant source of water-induced damping is wave radiation. Furthermore they deduct that an offshore wind turbine with a natural frequency of 0.3 Hz pile diameter of 4.7m located at 20m water depth would approximately have 0.12% critical damping induced from wave radiation. These numbers differ from the OWT examined in this study, but in the lack of further information a critical damping of $\zeta_w = 0.12\%$ was given to the water mass nodes below the seabed.

The inertial influence of the water was implemented by inserting nodal lumped masses following Newman (1977), by introducing an additional water mass (added mass) equal to:

$$m_w = 2\rho_w \frac{\pi D^2}{4} h \tag{7}$$

that is equal to twice the water mass occupying the submerged OWT volume (ρ_w is the water mass density, h is the height between two consequent water mass nodes). As shown in Figure 5, m_w is then evenly distributed as lumped masses along the underwater beam nodes of the OWT.

2.4 Space/time discretisation and solution algorithms

The time integration of the non-linear equation system (3) requires suitable algorithms for (i) global time marching, (ii) step increment solution, and (iii) stress-point integration.

Global time marching Time marching relates to the update of all the relevant field variables from their (known) value at time t_n to time t_{n+1}, over the step increment Δt. Here, the most widespread algorithm in Solid Dynamics – the Newmark integration method (Newmark, 1959) – is been employed. The required integration parameters are set to $\beta = 0.6$ and $\gamma = (\beta + 1/2)^2/4 = 0.3025$, yielding unconditionally stable time integration (in linear problems) and high-frequency dissipation Hughes (1987).

Step increment solution The implicit Newmark algorithm along with the non-linear equations (3a)–(3b) require an iterative solution scheme for each step increment, usually belonging to the Newton–Raphson family (De Borst et al., 2012). The accelerated Krylov–Newton algorithm described by Scott and Fenves (2003) is here fruitfully exploited, resulting in faster convergence by greatly decreasing the number of Jacobian evaluations per step increment (Carlson and Miller, 1998).

Stress-point integration In the presence of non-linear constitutive equations, a numerical integration scheme is needed to update stresses, strains and hardening variables over the step increment Δt. The selection of a suitable time step size Δt is discussed by Jeremić et al. (2009); Watanabe et al. (2016), also in relation to the use of highly non-linear soil models. The soil model adopted in this study (see Section 2.2) is integrated via the standard forward Euler explicit algorithm (Sloan, 1987).

Space/time discretization Suitable domain size and mesh density must be chosen wisely to ensure the proper description of the pore pressure and the displacement fields in space. A proper mesh and timestep have been chosen via sensitivity analyses.

2.5 S-transform and frequency shifts

In order to estimate the eigen frequencies of the response of the OWT, it is of common practise to look into the displacement time history of the hub. There are many ways to express a displacement time history in terms of its frequency content. Most usually the Fourier amplitude spectrum is utilized, which is calculated among the entire motion time-history under the assumption of periodicity. That is directly related to the fact that the FT (Fourier Transform) represents data as a sum of sinusoidal waves which oscillate indefinitely, not localized in either in time nor space. Thus, evolution of the amplitude spectrum over time is neglected in such an approach. Besides neglecting information regarding the timing of frequency shifts, having a signal whose frequency content changes in time, results in a "noisy" FT. That effect is substantially amplified for the cases at which the frequency content of the signal varies greatly over time.

The authors wanted a tool that would allow for capturing abrupt changes of frequency content over time, so that frequency shifts related to either changes of excitation frequencies or changes in soil stiffness, could be recorded. In that perspective the short time Fourier transform (STFT) could have been utilized, which results from a series of FTs applied upon a moving window on the signal. The STFT results in good resolution in the frequency domain but time resolution is rather poor. Wavelets are wave like oscillations with finite duration that can be fixed both in time and space by scaling and shifting the wavelets in the time domain. While the wavelet transform could be suitable for the task, they offer a poorer frequency resolution than the S (Stockwell)-transforms (Kramer et al., 2016) utilized in this study. The S-transform, (Equation 8) (Stockwell et al., 1996), was introduced as an extension of the continuous wavelet transform and is based on shifting a frequency-dependent Gaussian window in time (Equation 9). Thus, S-transforms are able to provide frequency dependent resolution for better capturing of the lower and the higher harmonics of a signal.

$$S(\tau, f) = \int_{-\infty}^{\infty} u(t)w(t-\tau, f)e^{-2i\pi ft}dt \tag{8}$$

As described, the most usual window w is Gaussian one which seen below:

$$w(\tau, f) = \frac{|f|}{k\sqrt{2\pi}}e^{-\frac{f^2t^2}{2k^2}} \tag{9}$$

where f is the frequency, t is time, τ is the time at which the window is fixed and k is a scaling factor greater than zero that controls the number of oscillations in a window. Higher values of k result in higher frequency but a poorer time resolution. In this study the S-transforms are produced with k=0.2. After numerous attempts, for this specific case, it was realized that such a value corresponds to the most desired trade-off that results in a discrete frequency resolution (narrow S-transform width in the frequency domain) but also allows capturing abrupt changes of frequency over time.

3 Site Description

3.1 Site choice

Considering that the aim of the thesis is to see the response to natural hazards of offshore wind turbines in Japan, a soil profile in Offshore Japan was desired. Unfortunately, no detailed soil profile in offshore Japan could be found, so soil profiles along coastal Japan have been investigated. This is acceptable, though, as it will not be possible to use monopiles very far from the shore given the high water depths. For this, the NIED (National Research Institute for Earth Science and Disaster Resilience) database has been employed. This database contains Strong-motion

Seismograph Networks across all of Japan. A collection of all the stations in Japan correspondent to this database can be seen in Figure 6.

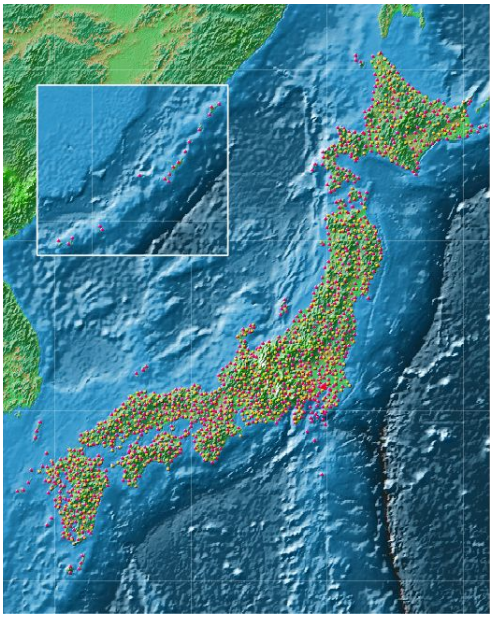

Figure 6: List of sites present in the NIED database, depicted as colourful dots on the map. (source: `http://www.kyoshin.bosai.go.jp`)

Out of the stations presented above, coastal stations have been investigated for the presence of sand. The reason for wanting a sandy site is looking into the earthquake response and liquefaction potential of the combined structure-soil model. After thorough investigation, station FKSH14 was chosen. The position of this specific site is depicted in Figure 7.

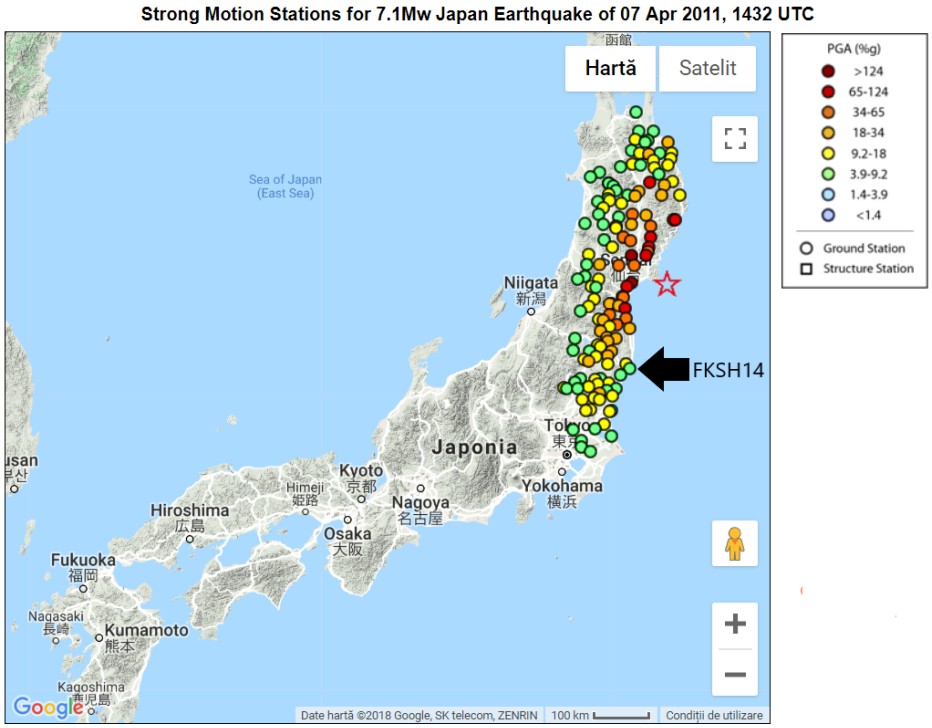

Figure 7: Stations that have recorded significant motions during the 7th of April 2011 earthquake and PGA recorded at these stations. (source: `https://strongmotioncenter.org`)

The stratigraphy at the station is presented in Figure 8

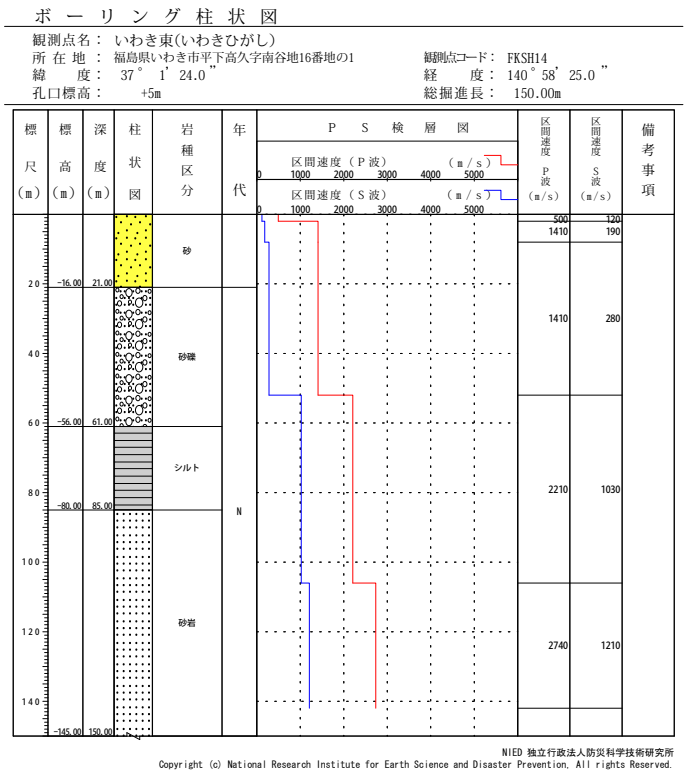

Figure 8: Stratigraphy and velocity profiles for FKSH 14 station. (source: `http://www.kyoshin.bosai.go.jp`)

Table 1: Borehole Description

Stratum	Depth(m)
Sand	0-21
Sandy Gravel	21-61
Silt	61-85
Sandstone	85-150

The depths of the strata can be seen in Table 1.

3.2 Geotechnical characteristics at site

Not many geotechnical parameters at this specific site could be found in general, so the ones that could be found have been adopted, while the others were obtained by backtracking.

The NIED database provided the soil characteristics presented in the table below.

Table 2: Borehole Geotechnical data

No	Thickness (m)	Depth(m)	V_p (m/s)	V_s (m/s)
1	2.00	2.00	500.00	120.00
2	6.00	8.00	1410.00	190.00
3	44.00	52.00	1410.00	280.00
4	54.00	106.00	2210.00	1030.00
5	...	...	2740.00	1210.00

According to Roten et al. (2014) the soil at station FKSH14 has a high liquefaction resistance ($CRR_7.5 = 0.5$) and exhibited dilation pulses of up to 0.4g during the Tohoku earthquake (2011). Using this observation, we can conclude that we are dealing with a sand with a high relative density, as loose sands are prone to liquefaction.

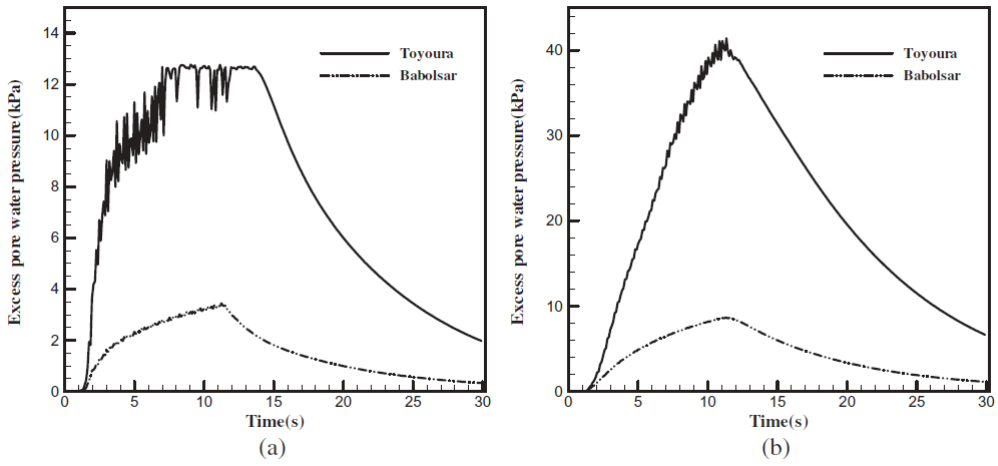

Figure 9: Comparison of time histories of excess pore pressure Toyoura and Babolsar sand during centrifuge test: (a) depth of 1.25m; (b) depth of 5.0m (source: Zahmatkesh and Janalizadeh Choobbasti (2017))

The constitutive model employed in this thesis is the SaniSand model.

SaniSand cannot be calibrated only against site investigation data, but lab tests are needed. As lab tests are not available, a reasonable pre-made calibration has been chosen.

Zahmatkesh and Janalizadeh Choobbasti (2017) proposed 3 different sand types, each with a list of parameters to be employed during the analysis. Various material tests have been done on these different sand types in order to observe their behaviour. According to Figure 9, Babolsar is the most dilative sand of them all, due to the fact that it accumulates the least excess compressive pore pressures. As expected, the sand closer to the surface (depth of 1.25m) accumulates less excessive pore pressures due to the lower overburden stress and also a richer and higher frequency content (more "jiggliness" in the graph compares to the 5.0m case). It should be noted that in Figure 9, the permeabilities of both sands ave been assumed identical, so the difference in results comes strictly from the parameters models. As it will be shown in the next section, the parameters have been fine tuned in order to match the reality at station FKSH-14.

4 Numerical model calibration

4.1 1D Soil Column

Boundary conditions In order to tune the soil parameters, a 1D soil column was modelled using OPENSEES. The full depth of the borehole (150m) was modelled, using the parameters presented in the previous chapter. The reason for modelling the 1D soil column is to do an "inverse analysis" approach to identify soil parameters from the dynamic response of the actual layered deposit. A depiction of the boundary conditions and the model can be seen below:

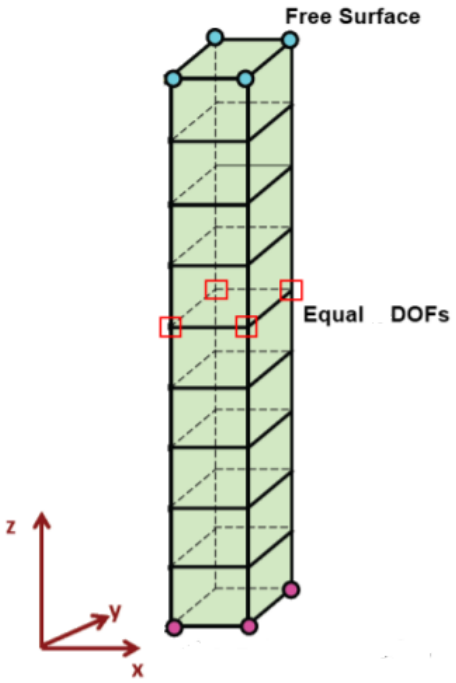

Figure 10: Depiciton of the boundary conditions employed for the 1D soil column (source: Pisano 2018)

The boundary conditions are as follows:

- Shear beam boundary condition;
- The model is allowed to drain at the top;
- Earthquake displacement time history in all three directions applied at the bottom;

The reason for applying displacement time histories instead of acceleration time histories is to eliminate the need for dashpots at the bottom of the model that would be used to model soil impedance. By applying displacement directly, it acts as a boundary condition itself, that incorporates the impedance of the soil beneath.

Material Models The material models used for the model are as follows:

- Sand is modelled as a Manzari Dafalias material using the OpenSees predefined Manzari Dafalias material and changing the parameters to those of Babolsar Sand;
- Gravel is modelled similarly to the sand, but with a different void ratio, permeability and unit weight;

- Due to their very high stiffness, the silt and the sandstone are both modelled as elastic-isotropic one-phase materials using dynamic properties directly inferred from site data

Element type Considering that we are interested in the pore pressure evolution in both the sand and gravel layer, those have been modelled as two phase elements "SSPbrickUP", while the silt and the sandstone have been modelled as one phase "SSPbrick" elements.

In the following section, let us take a look into the choice of seismic motions.

4.2 Choice of seismic motions

The reasoning behind the choice of ground motions was to have a strong one that pushes the soil into the non-linear regime, a medium intensity one that might trigger some non-linearity and a low intensity one that would keep the soil in the linear regime.

Using the NIED database, the following ground motions have been chosen:

1. 2011 Tohoku strong ground motion recorded at FKSH14 station with a PGA = 480 gal ;
2. Ground motion recorded at FKSH14 station with a PGA = 255 gal;
3. Ground motion recorded at FKSH14 station with a PGA = 125 gal.

Above, the displacement time histories at both the top and the bottom of the borehole are presented for each of the three ground motions. By taking a closer look at Figure 11, one can see that for the Tohoku Earthquake, at the borehole the displacement in the North-South direction is the highest, peaking at almost 0.2m. The smallest displacement are, as one would expect in the vertical direction with a maximum of around 0.05m. Also, the vertical motion contains higher frequencies, which can easily be shown with a Fourier Transform.

By comparing Figure 11 with Figure 14, it is obvious that the soil domain amplifies the motion (0.2m in NS direction at borehole compared to 0.3m at top) , resulting in bigger displacements at the top compared to the bottom. It has been long known that soft soils amplify seismic waves, but the phenomenon is not completely understood for stiff soils (Roten et al., 2014). Similar results are observed for the other two ground motions.

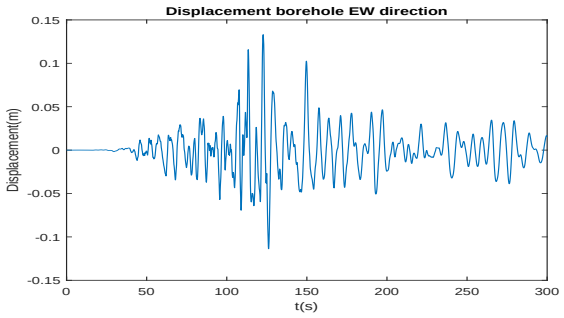

(a) EW

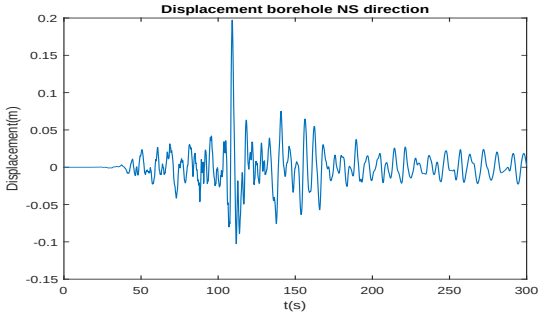

(b) NS

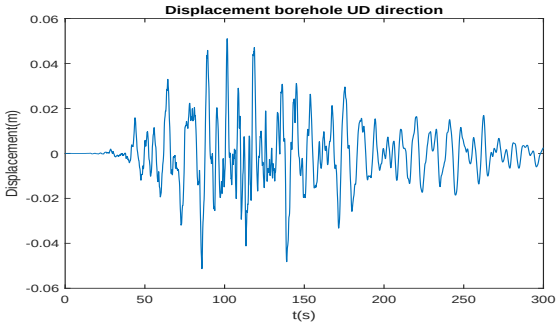

(c) UD

Figure 11: Displacement time histories at bottom of borehole Tohoku Earthquake

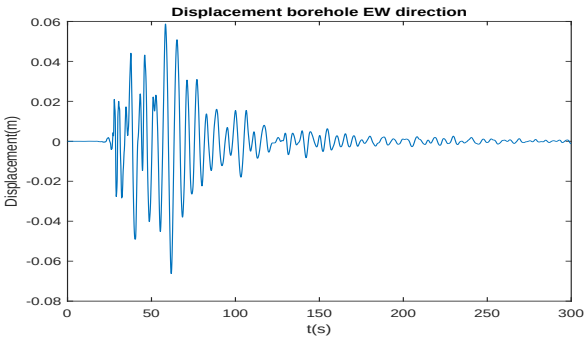

(a) EW

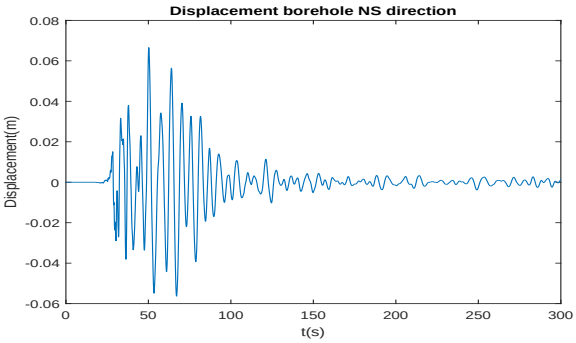

(b) NS

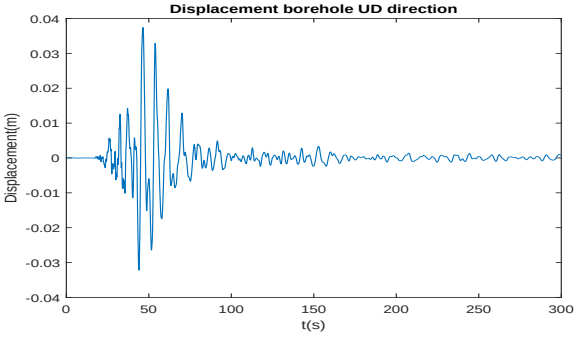

(c) UD

Figure 12: Displacement time histories at bottom of borehole 255gal Earthquake

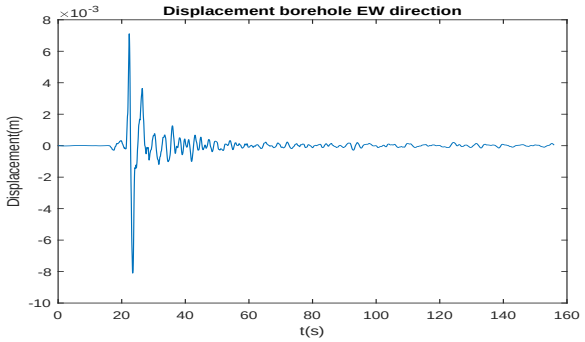

(a) EW

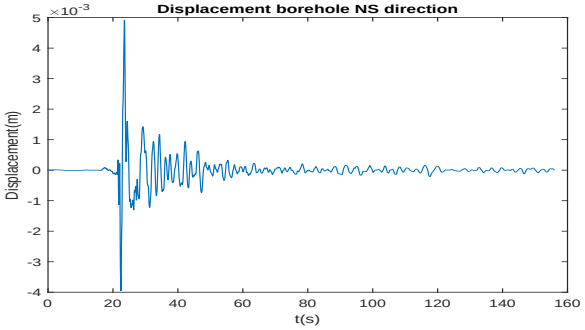

(b) NS

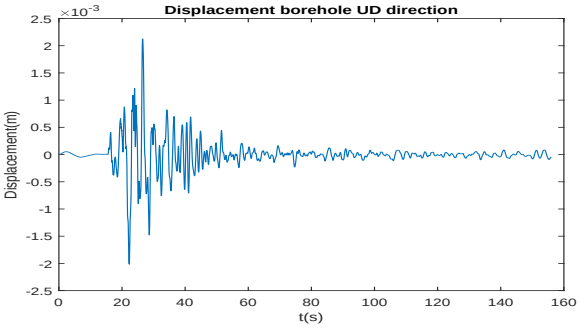

(c) UD

Figure 13: Displacement time histories at bottom of borehole 125gal Earthquake

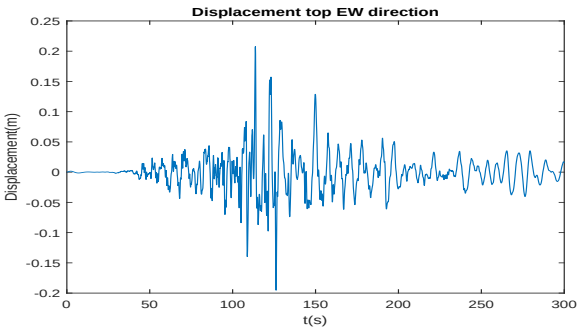

(a) EW

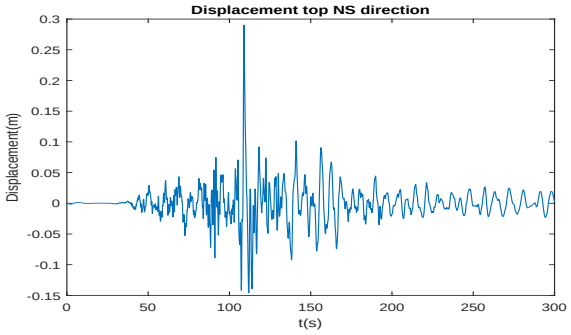

(b) NS

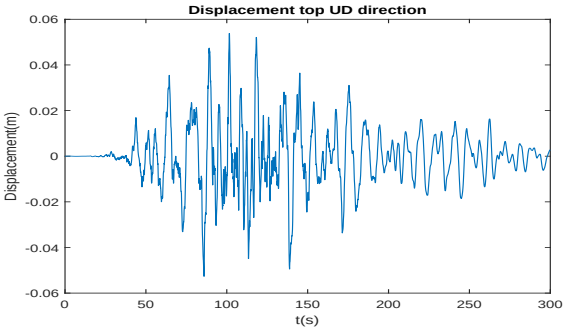

(c) UD

Figure 14: Displacement time histories at top of borehole Tohoku Earthquake

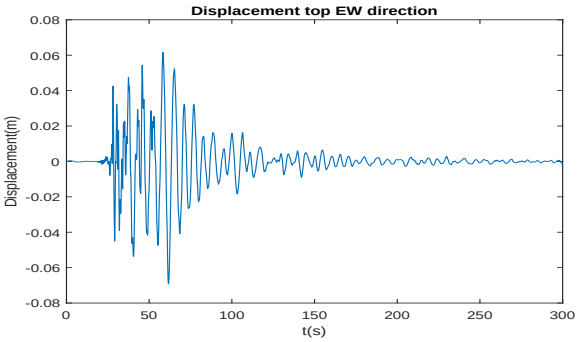

(a) EW

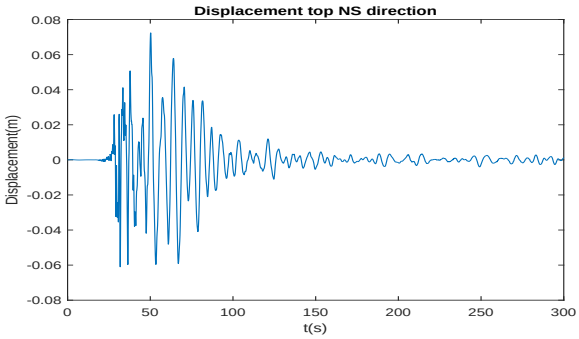

(b) NS

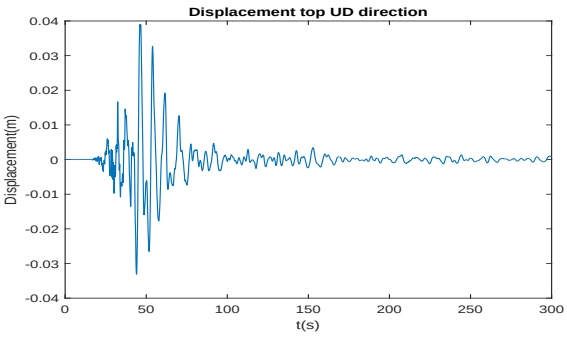

(c) UD

Figure 15: Displacement time histories at top of borehole 255gal Earthquake

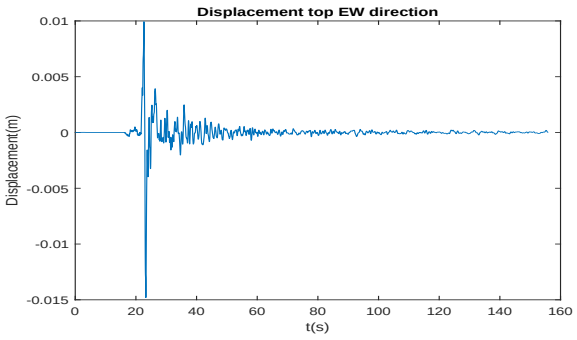

(a) EW

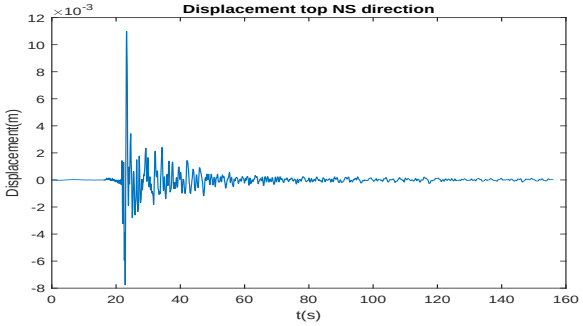

(b) NS

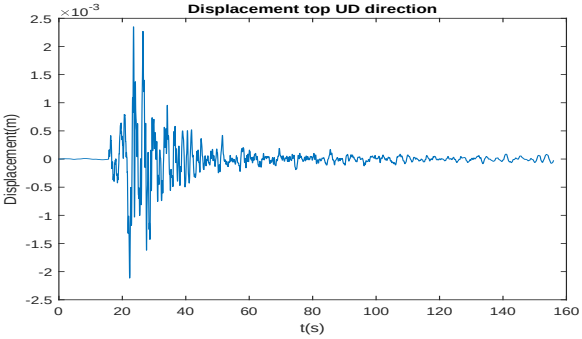

(c) UD

Figure 16: Displacement time histories at top of borehole 125gal Earthquake

4.3 Model calibration

4.3.1 Mesh calibration

In order to chose a convenient mesh size, one needs to decide how many elements should be used per one wavelength. As a general rule of thumb, 8 to 10 elements per wavelength give adequate results.

Usually, the highest frequency component of a seismic motion is the vertical component. A Fourier transform was used in order to observe the highest frequency present in the vertical motion of the Tohoku Earthquake:

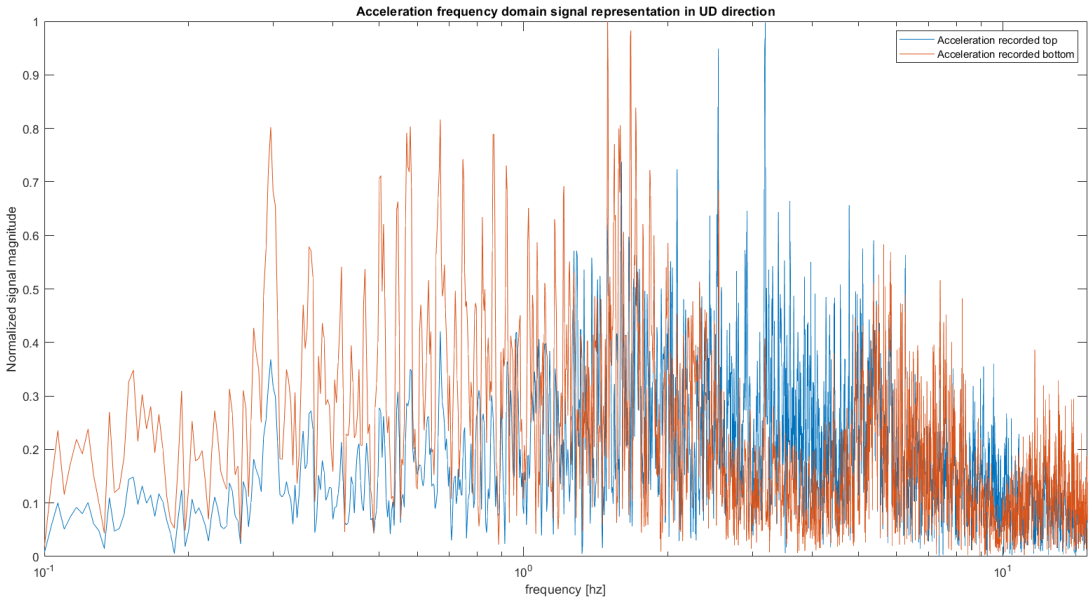

Figure 17: FFT of the UD component of the Tohoku earthquake at the top and at the bottom of the soil column

By taking a close look at Figure 17, it can be seen that most of the energy is concentrated under 10 Hz, so the highest frequency that was chosen to be well resolved is 10 Hz.

Using Table 2 and performing a weighted average of depths and shear wave velocities, the following values were obtained:

Table 3: Shear wave velocities

Stratum	V_S (m/s)
Sand	239
Sandy Gravel	448
Silt	1030
Sandstone	1152

The next step was determining the wavelength of the highest resolved frequency which is determined with the following formula:

$$\lambda_{min} = \frac{V_{s_{min}}}{f_{max}} \tag{10}$$

With this, the element size could be determined with Equation 11

$$h_{element} = \frac{\lambda_{min}}{n_{ele}} \tag{11}$$

In the equation above, n_{ele} refers to the number of elements that one wishes to capture per one wavelength.

In the end, an element size of 2.625m in all directions was adopted.

A sensitivity analysis was performed, where the highest frequency that was chosen to be well resolved was 100 Hz, and the results were similar.

4.3.2 Time step calibration

The time step for equation solving has been chosen equal to the one of the recording (0.01s). In case the solution has high gradients at different points in time, the solver will reduce the time step in order for the solution to converge.

4.4 Material model calibration

The silt and the sandstone were easily modelled as one-phase elastic-isotropic materials with the following characteristics:

Table 4: Silt and sandstone material characteristics

Stratum	E (kPa)	ν (-)	ρ (kg/m^3)
Silt	6.9e6	0.495	2200
Sandstone	8.7e6	0.495	2200

Notice that ν is taken as 0.495 as the approach is one-phase total stress to model nearly undrained elastic behaviour.

The shear modulus,G, was determined with the following formula:

$$G = \rho V_s^2 \tag{12}$$

and the elastic modulus, E, was determined with the formula presented in Equation 13

$$E = 2G(1 + \nu) \tag{13}$$

For the sand and the gravel, Sanisand 2004 has been adopted (Dafalias and Taiebat, 2016). The calibration started from the properties of Babolsar sand (Zahmatkesh and Janalizadeh Choobbasti, 2017), which can be seen in table 5:

Initially, a trial run was done for the 1D soil column using the standard description above for both the sand and the gravel layer. The displacements at the top of the soil column were compared with the ones recorded by the station. The response of the numerical model was much "looser" than the one recorded by the station, resulting in significantly bigger displacements. After this observation was done, calibration of the parameters of Manzari Dafalias was started in order to match the numerical result at the top with the recorded motion at the top. The process was laborious and governed by trial and error.

As mentioned earlier, according to Roten et al. (2014), the sand at the site is hardly liquefiable, which points us to a sand of high stiffness and high relative density. The gravel at the site also shown no signs of liquefaction, so the same reasoning applies.

The void ratios for the sand and the gravel that give the best fit are as follows:

Table 5: Babolsar sand characteristics (Zahmatkesh and Janalizadeh Choobbasti, 2017)

	Variable	Value
		Babolsar sand
Elasticity	G_0	100
	ν	0.05
Critical state	M	1.45
	c	0.682
	λ_c	0.018
	e_0	0.781
	ξ	0.7
Yield surface	m	0.01
Plastic modulus	h_0	50.99
	c_h	1.248
	n^b	7.51
Dilatancy	A_0	0.48
	n^d	7.51
Fabric-dilatancy tensor	z_{max}	35
	c_z	700

- $e_{sand} = 0.55$
- $e_{gravel} = 0.40$

Zahmatkesh and Janalizadeh Choobbasti (2017) propose the following minimum and maximum void ratio for Babolsar sand: $e_{min} = 0.526$, $e_{max} = 0.8$

Regarding the sandy gravel, Evans and Zhou (1995) proposed the following ranges of void ratio, depending on gravel content:

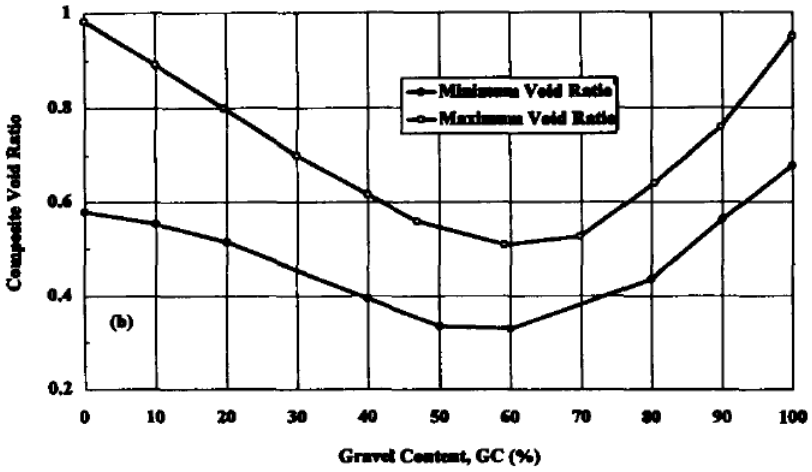

Figure 18: Void ratio of a sand-gravel mixture depending on gravel content (Evans and Zhou, 1995)

Due to unavailability of clear information on the gravel content of the mixture, a minimum void ratio of 0.35 and a maximum void ratio of 0.55 are chosen. With the information above, the relative density of the gravel and the sand, respectively, can be calculated with the following

formula:

$$R_D = \frac{e_{max} - e}{e_{max} - e_{min}} \tag{14}$$

which resulted in the following void ratios:

- R_D sand = 91.2%
- R_D gravel = 75%

The rest of the parameters have been tuned taking into account that gravels generally have a stiffer response than sands, and they are more permeable.

The other parameters for the sand and the gravel in comparison with the standard Babolsar sand parameters are presented in the table below:

Table 6: Final Manzari Dafalias parameters

	Variable	Value		
		Babolsar sand	Sand	Gravel
Elasticity	G_0	100	180	220
	ν	0.05	0.3	0.3
Critical state	M	1.45	1.65	1.90
	c	0.682	0.682	0.682
	λ_c	0.018	0.018	0.018
	e_0	0.781	0.781	0.781
	ξ	0.7	0.7	0.7
Yield surface	m	0.01	0.01	0.01
Plastic modulus	h_0	50.99	50.99	50.99
	c_h	1.248	1.248	1.248
	n^b	7.51	7.51	7.51
Dilatancy	A_0	0.48	0.008	0.008
	n^d	7.51	7.51	7.51
Fabric-dilatancy tensor	z_{max}	35	35	35
	c_z	700	700	700

As it can be seen in the table above, both the sand and the gravel are much stiffer than the standard Babolsar sand.

Regarding permeabilities, the optimal values were also found by trial and error. Due to the cyclic nature of the load and the dilative behaviour of the material, the excess pore pressure development is not monotonous. In the case of loose sand, a low permeability would lead to high contractive excess pore pressures, which would lead to stiffness degradation of the soil, resulting in a looser response (higher displacements). In the case of dilative accumulation of excess pore water pressures, the soil will become stiffer, resulting in a stiffer response (lower displacements). Due to the highly non-monotonous nature of the pore pressure evolution and the high coupling between the void ratio and permeability, choosing the permeabilities was not a straight forward task.

The following values gave the best fit:

- k_{sand} = 3.0e-4 m/s
- k_{gravel} = 1.0e-2 m/s

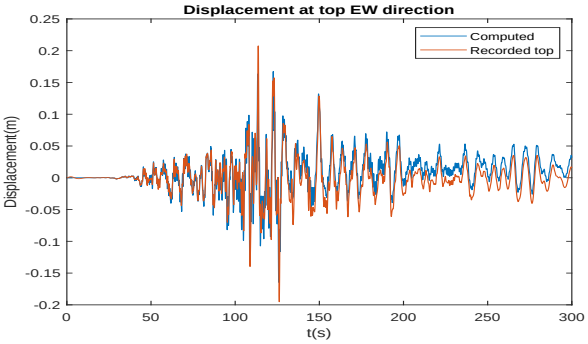

(a) EW

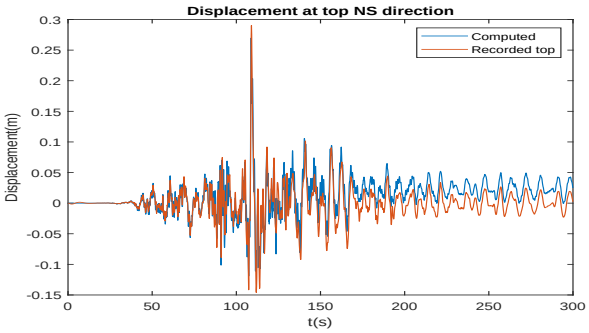

(b) NS

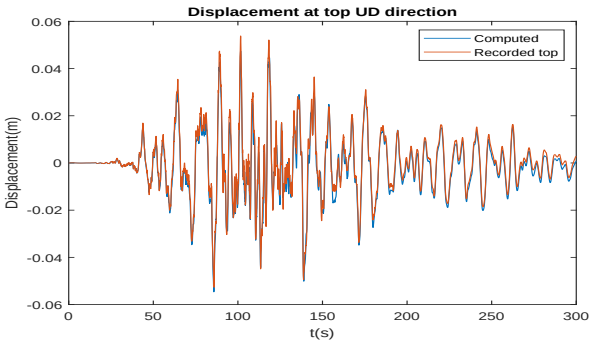

(c) UD

Figure 19: Computed vs recorded displacement Tohoku

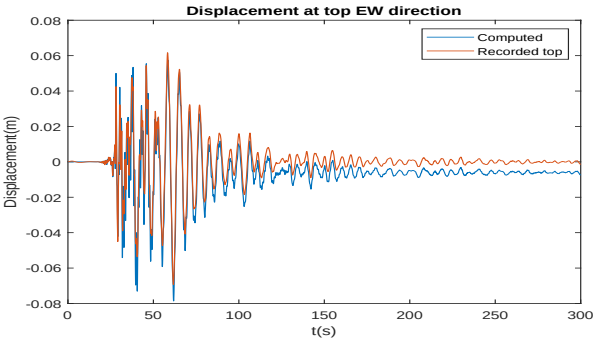

(a) EW

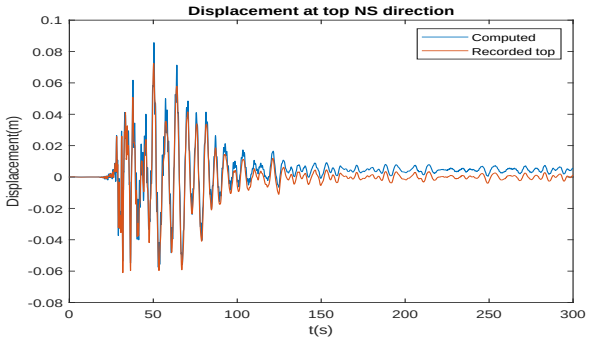

(b) NS

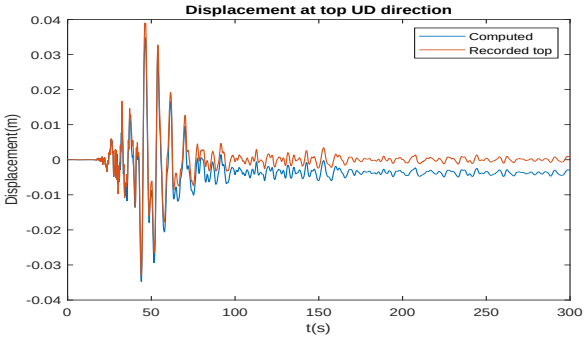

(c) UD

Figure 20: Computed vs recorded displacement 255 gal

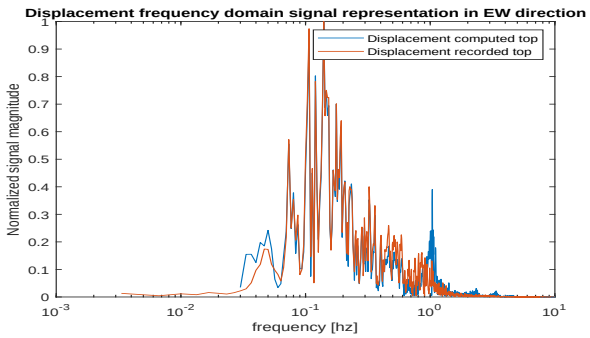

(a) EW

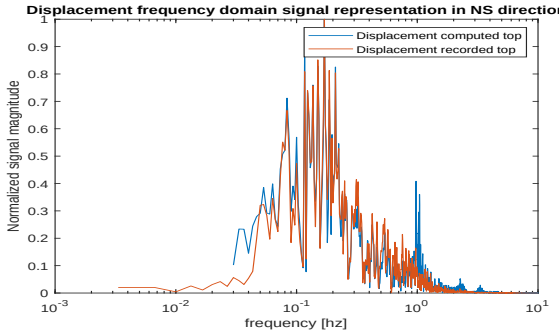

(b) NS

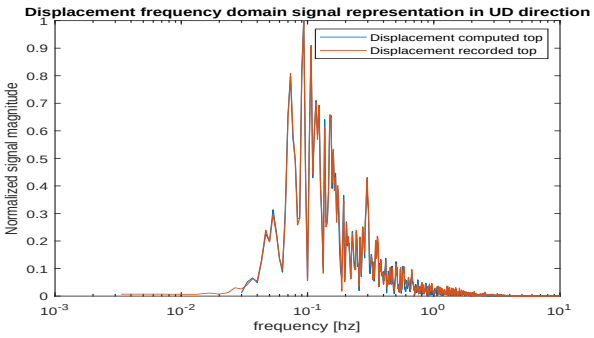

(c) UD

Figure 21: FFT computed vs recorded displacement Tohoku

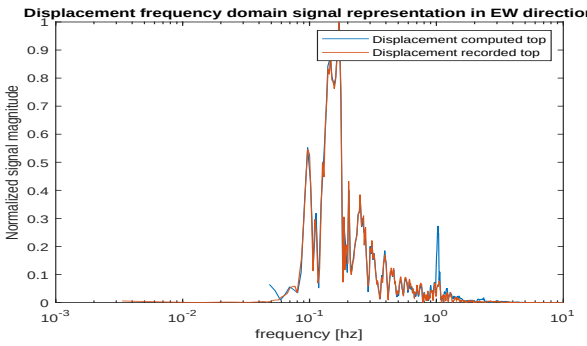

(a) EW

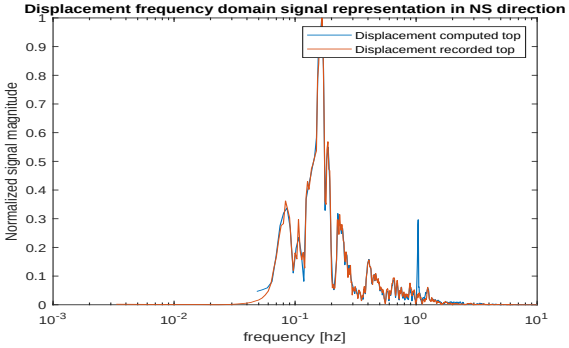

(b) NS

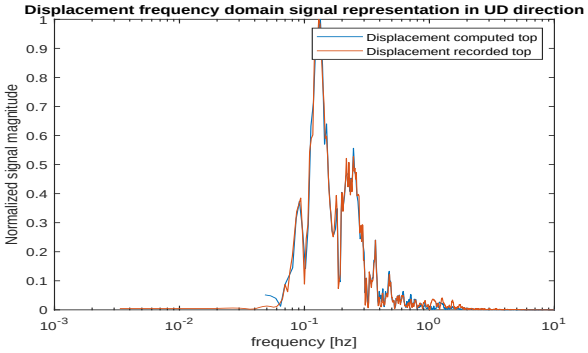

(c) UD

Figure 22: FFT computed vs recorded displacement 255 gal

For validation of the numerical model, the Tohoku earthquake and the 255gal earthquake have been used. The comparison between the computed motion and the recorded motion in terms of displacements is found in Figures 19 and 20.

The computed results fit satisfactory the recorded result, with only a slight over-estimation of displacements in the case of the computational model.

Another vertification that should be done is checking the frequency content of the computed signal against the recorded one. This has be done in Figures 21 and 22.

By taking a closer look at the results of the Fourier transforms, one can see that there is good correspondence between the frequency content of the computed and of the recorded motion. The only noticeable difference between those two is that the computed motion also contains energy at higher frequencies (i.e. 1Hz). This is caused by the fact that an onshore borehole is used for an offshore model, where saturation is not complete until the top, so shear wave velocity is different, resulting in the different frequency content.

The results above prove that the suggested calibration is satisfactory.

4.5 Reduced model

Due to the very big height of the soil domain (150m), transitioning the soil column to a full 3D model would require extensive computational power and time. In order to avoid this, an investigation has been done if it would be possible to remove the silt and sandstone layers from the problem. The reason for this is that those layers are so stiff, that the ratio between the displacements at the top of silt layer and the input displacements is almost one. It is known that loose layers amplify seismic motions, while a very stiff medium would have almost a rigid body motion, not amplifying the seismic waves. For this, the displacement at the interface between the silt layer and the gravel layer is compared to the input motion at the bottom.

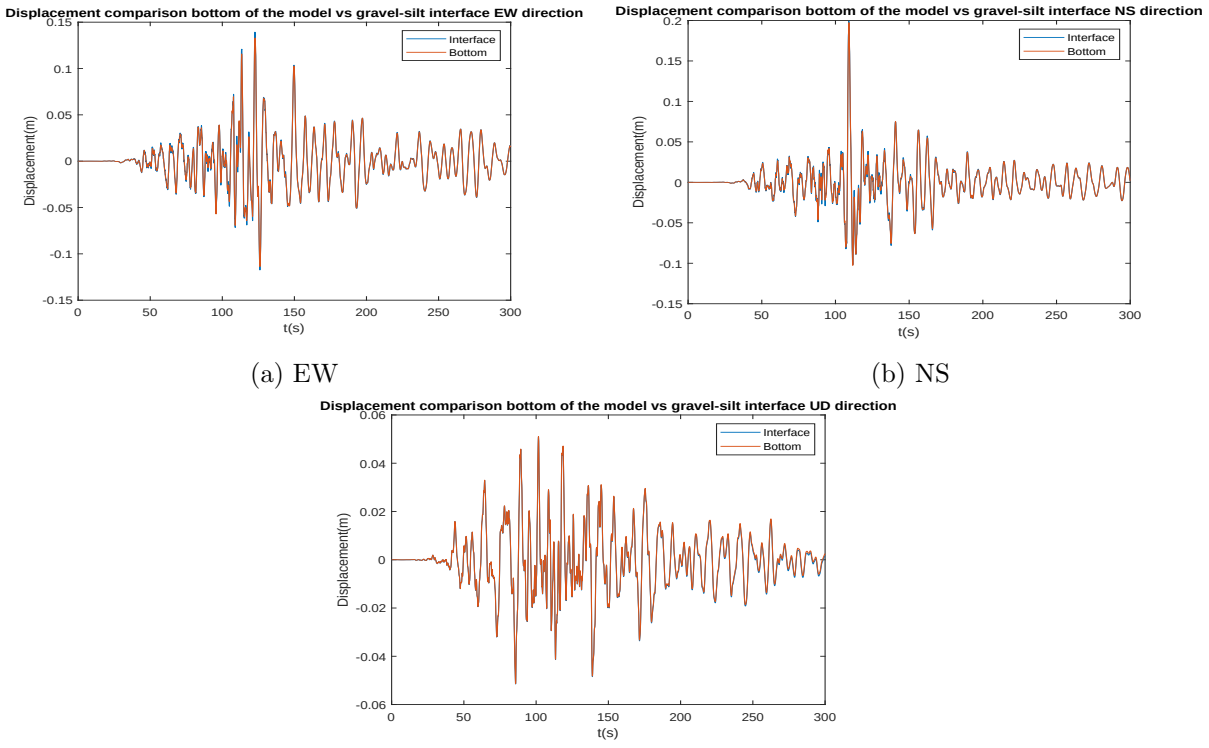

(a) EW

(b) NS

(c) UD

Figure 23: Displacement comparison bottom of model vs silt-gravel interface Tohoku

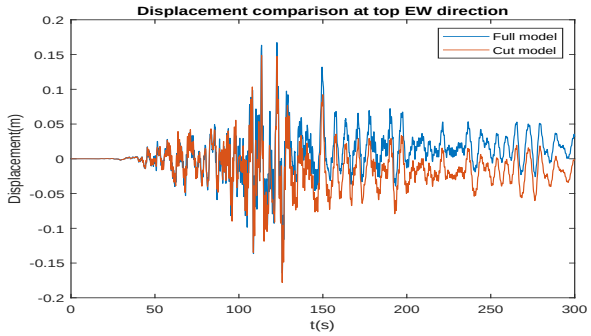

(a) EW

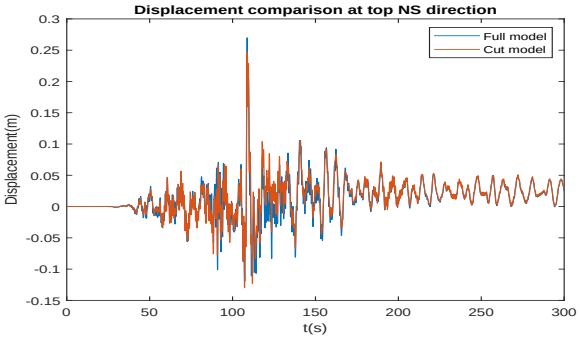

(b) NS

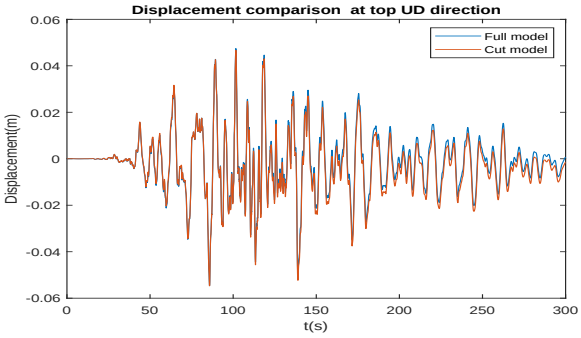

(c) UD

Figure 24: Displacement comparison full vs reduced model at top of the sand layer Tohoku

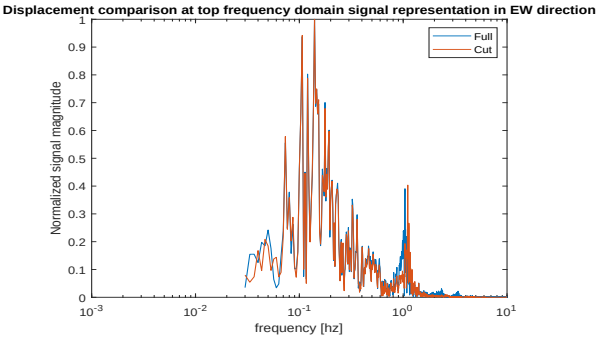

(a) EW

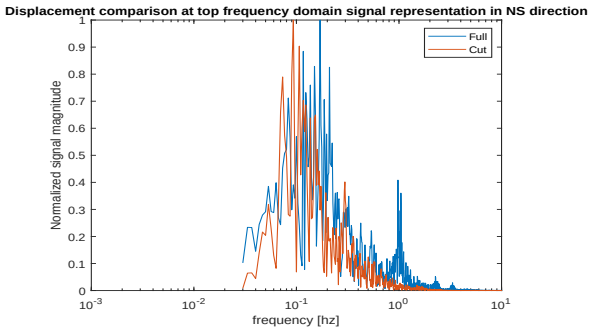

(b) NS

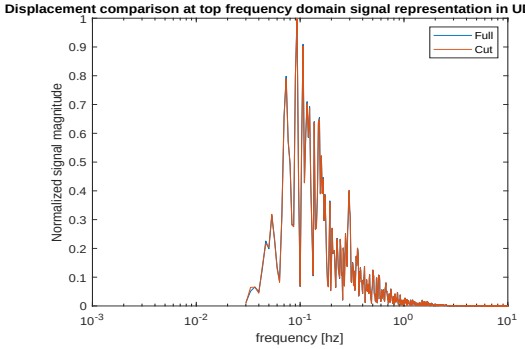

(c) UD

Figure 25: FFT displacement comparison full vs reduced model at top of the sand layer Tohoku

As depicted in Figure 23, the stiff bottom layers do not amplify significantly the seismic motion, thus, the displacements at the silt-gravel interface are very similar to the ones at the bottom of the model.

In order to confirm the theory that the silt and sandstone layers can be removed from the model, a new model has been created.

The model contains only the sand and gravel layers. The displacement time history used as input for the bottom of the sandstone layer, is now used at the bottom of the gravel. The comparison between the results at the top of the sand layer in the two models can be seen in Figures 24 and 25. From a displacement value point of view, the match is good in the NS and UD direction, but the new model does not offer a good match in the EW direction. From a frequency content point of view, the model offers a good match in the EW and UD directions, but not in the NS direction. In the NS direction, there is significantly more energy in higher frequencies compared to the recording. This can also be confirmed by taking a look at the "jigglyness" of the displacement graph in the NS direction. Jigglyness is directly related to high frequency content.

In the next section, the full 3D model development will be presented.

5 Loads

5.1 Environmental loads

After the model has been calibrated as shown in the previous sections, wind and wave loads were generated. Kiyomiya et al. (2002) concluded that in combination with earthquake loads, SLS wind and wave should be used , as the probability of an earthquake occurring at the same time as ULS wind and waves is extremely small.

For this, the procedure presented in Corciulo et al. (2017) was used.

The assumptions are that wind and wave thrusts, F_{wind} and $F_{wave}(i)$ depend on wind velocity and system geometry, (ii) depend on the application of empirical aero- and hydrodynamic factors and (iii) are co-directional. Also, the effect of rotor revolution on wind speed is neglected. Wind thrust can be calculated according to Equation 15.

$$F_{wind} = \frac{1}{2} A_R C_T \rho_{air} V_{wind}^2 \tag{15}$$

where A_R is the swept area of the rotor (m^2), ρ_{air}=1.2 kg m^{-3}, V_{wind} is the wind speed (ms^{-1} and $C_T = 0.688$ (empirical wind thrust coefficient). By postulating a sustained wind field, an equilibrium sea state is assumed. A Pierson-Moskowitz wave spectrum is postulated to quantify the wave energy S associated with each frequency f, see Equation 16:

$$S(f) = \frac{\alpha g^2}{(2\pi f)^5} exp\left(-\beta \left(\frac{g}{2\pi f V_{wind}^{19.5m}} \right)^4 \right) \tag{16}$$

where $\alpha = 0.0081$ and β=0.74 are empirical constants, $g = 9.81 ms^{-2}$, $V_{wind}^{19.5m}$ = wind speed at 19.5m above sea level. Wind speeds can be extrapolated from a reference measurement using a power law formulation. Wave frequency f_s (at maximum spectral amplitude) and wave height H_S (distance between crest and though) are shown in Equation 17

$$\begin{aligned} f_s^4 &= \frac{4\beta}{5} \left(\frac{g}{2\pi V_{wind}^{19.5m}} \right)^4 \\ H_s &= 2\sqrt{\frac{\alpha}{\beta}} \frac{\left(V_{wind}^{19.5m}\right)^2}{g} \end{aligned} \tag{17}$$

The mono harmonic sea state defined by f_s and H_s can be transformed into a hydroynamic thrust F_{wave} using the Morison equation with drag and intertial force components as shown in Equation 18

$$\begin{aligned} F_{wave}^D &= \rho_w g \frac{C_d D}{8} H_S^2 \left(\frac{1}{2} + \frac{KH}{sinh\ 2\ kH}\right) \\ F_{wave}^I &= \rho w g \frac{C_m \pi D^2}{8} H_S\ tanh\ kH \end{aligned} \tag{18}$$

The overturning moments with respect to he mudline are shown in Equation 19.

$$\begin{aligned} M_{wave}^D &= \rho_w g \frac{C_d D}{8} H_S^2 \left(\frac{H}{2} + \frac{2(kH)^2 + 1 - cosh\ 2\ kH}{4k\ sinh\ 2\ kH} \right) \\ M_{wave}^I &= \rho_w g \frac{C_m \pi D^2}{8} H_S H \left(tanh\ kH + \frac{1}{kH} \left(\frac{1}{cosh\ kH - 1} \right) \right) \end{aligned} \tag{19}$$

C_d and C_m, the drag and inertia coefficients are taken as 0.65 and 1.6 respectively. H is the height of the water column (m), D is the monopile diameter (m), ρ_w is the seawater density (1025 kg m^-3) and k is the wave number, related to the wave length (λ_w). An explicit approximation of k is presented in Equation 20.

$$k = \frac{\omega^2}{g\left(tanh\left(\left(\frac{2\pi\sqrt{\frac{H}{g}}}{T}\right)^{\frac{3}{2}}\right)\right)^{\frac{2}{3}}} \tag{20}$$

where $T = \frac{2\pi}{\omega}$. The drag and inertial components of the wave thrust will be out of phase, therefore resultant mudline forces and moments are calculated using the Square Root Sum of Squares (SRSS).

$$\begin{aligned} F_{wave} &= \sqrt{(F^I_{wave})^2 + (F^D_{wave})^2} \\ M_{wave} &= \sqrt{(M^I_{wave})^2 + (M^D_{Wave})^2} \end{aligned} \tag{21}$$

In order to able to generate the loads, a wind time history had to be employed. Tsuchiya et al. (2006) recorded the direction and speed of the wind using a platform for natural gas mining, 37 km far from a coastline in the Pacific Ocean. The platform was located on the wast sea of the Tohoku district, northeast part of Japan. The platform has a trussed tower, and a windmill-type anemometer. The sensor height is 94 m above the sea level. The annual wind speed average was 7.5 m/s and the turbulence intensity was 8%.

Using the information above and the software "FAST" [10] from NREL, wind time histories for 10 seconds, 40 seconds and 70 seconds have been generated.

A 5 second ramp up time has been used for the wind time history to avoid going from static conditions to a fully developed wind field instantly. Loading the turbine like that would lead to numerical instability, so a ramp up is chosen (Corciulo et al., 2017).

With the wind time history generated, the other quantities could be obtained as well. It is important to note that from an analytical perspective, a wind time history should be 600 seconds long in order to correctly capture all frequencies. Wind and wave loads are not the main scope of this thesis, so this has been overlooked. The results can be seen in the figures below.

[10] `https://nwtc.nrel.gov/FAST`

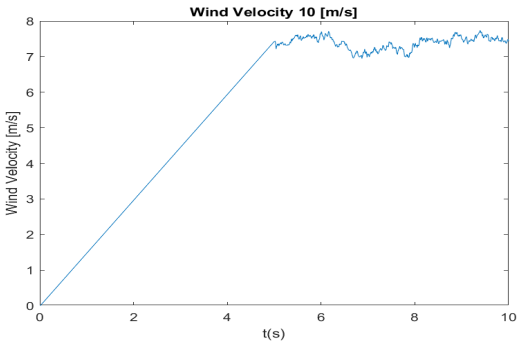

(a) 10 seconds

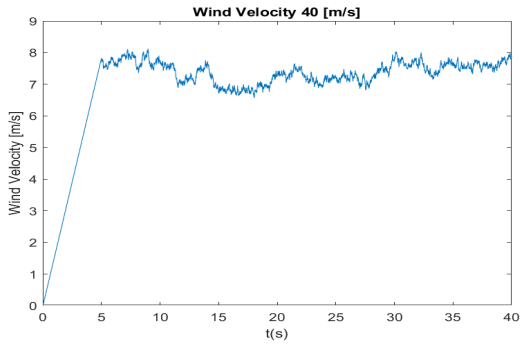

(b) 40 seconds

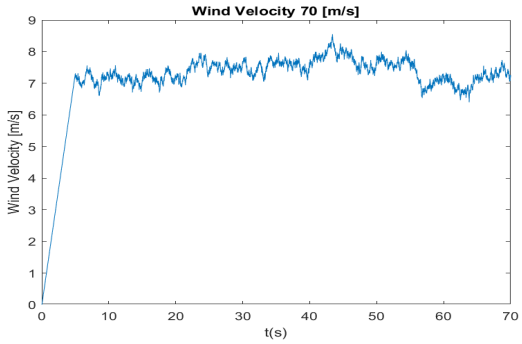

(c) 70 seconds

Figure 26: Wind speed time histories

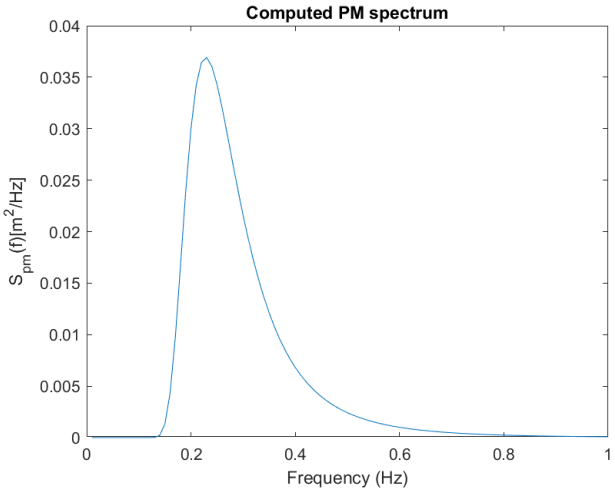

Figure 27: Pierson-Moskowitz wave spectrum

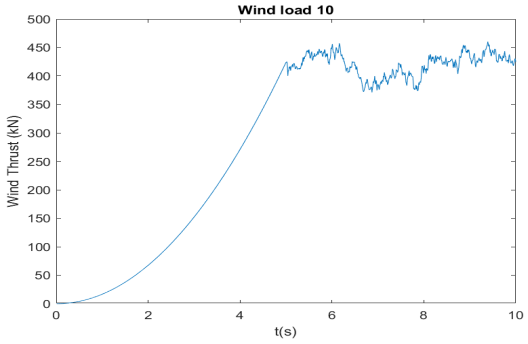

(a) 10 seconds

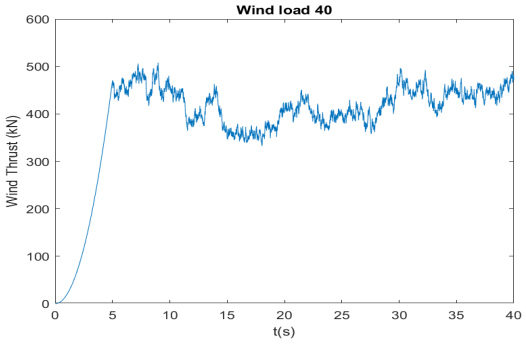

(b) 40 seconds

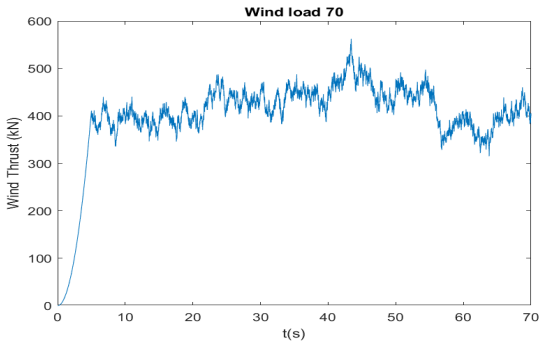

(c) 70 seconds

Figure 28: Wind load time histories

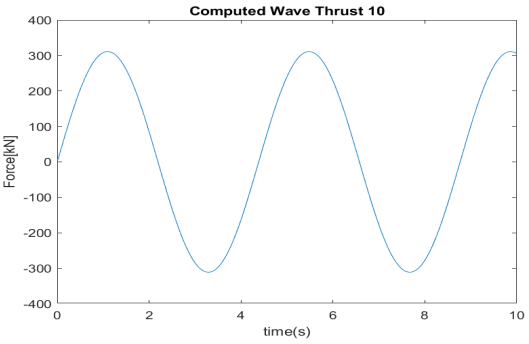

(a) 10 seconds

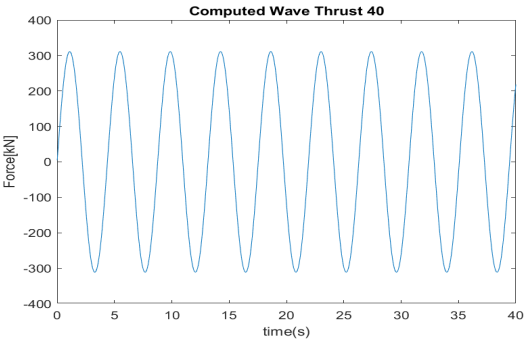

(b) 40 seconds

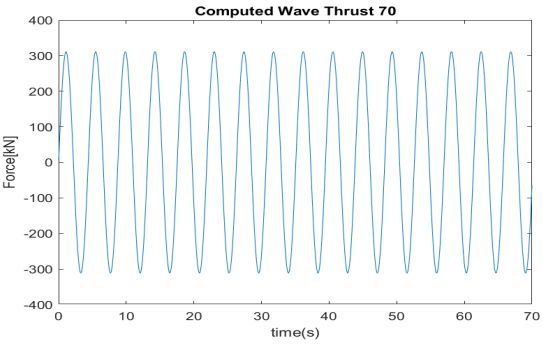

(c) 70 seconds

Figure 29: Wave load time histories

After the calculation was done, the following results were obtained:

- Significant wave height, H_s=0.77 m
- Lever arm of wave load, δ_{F_s} = 30 m

Considering that the average water depth at the location is 30m, the wave load has been directly applied at sea level. The wind load has been applied at the hub.

In the next section, tuning of the earthquake loads will be presented.

5.2 Earthquake loads

The Earthquake time histories have been already shown in section 4. Due to the size of the model, running 300 seconds simulations is very time consuming. Thus, it was decided to only apply the time history correspondent to the the significant duration of the earthquake. The significant duration of the earthquake is the time period in which 5% to 95% of the energy is released. For each of the earthquakes, the 5% and 95% times are as follows:

- 70-140 seconds for Tohoku;
- 28-68 seconds for 255 gal;
- 22-32 seconds for 125 gal;

In order to have some insight into the steady state, another 10 seconds of analysis have been run in the case of the 10 seconds motion, and another 20 seconds have been run in the case of the 40 seconds motion. After the significant-duration of the earthquake was over, all loads were removed, including environmental loads.

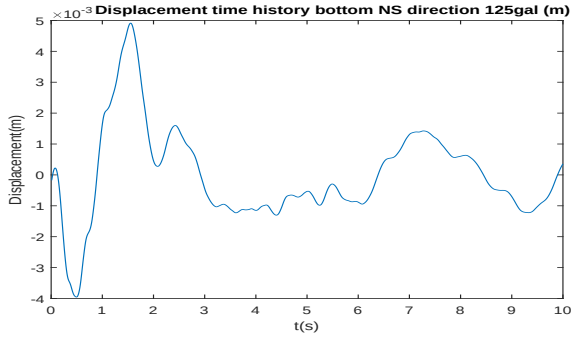

(a) 125 gal

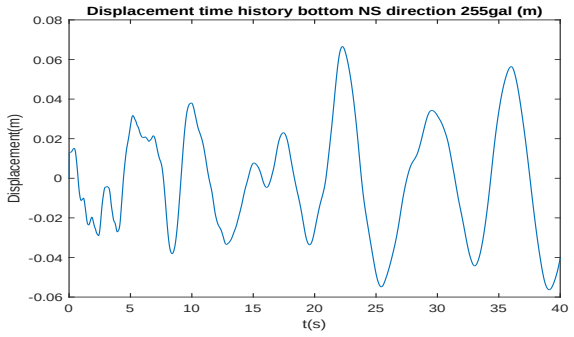

(b) 255 gal

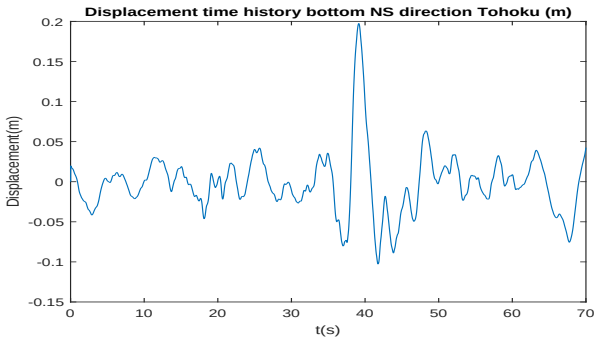

(c) Tohoku

Figure 30: Significant duration ground motions NS direction

The seismic motions presented above will be used as input in the 3D numerical model.

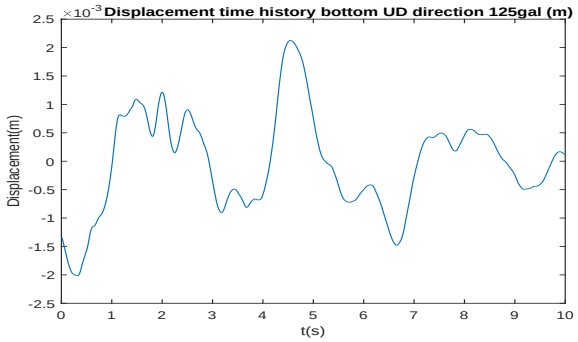

(a) 125 gal

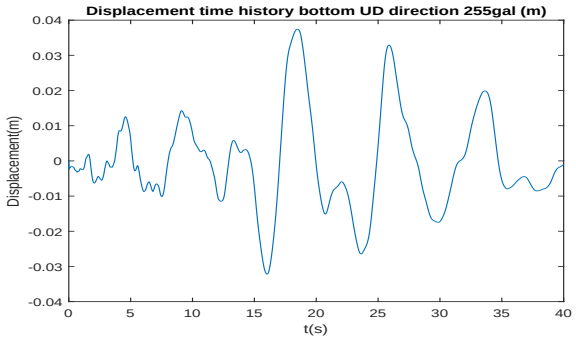

(b) 255 gal

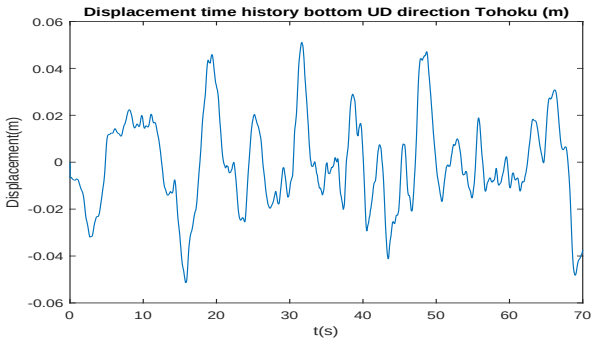

(c) Tohoku

Figure 31: Significant duration ground motions UD direction

6 Non-linear performance under combined loading

6.1 3D model geometry

The details regarding the model have been discussed in the previous sections. The geometry of the model is presented in the figure below:

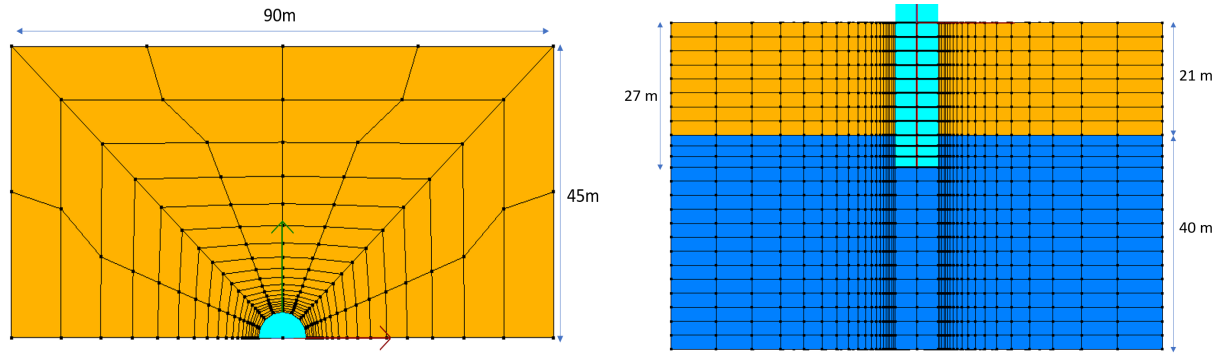

(a) XY plane view (b) XZ plane view

Figure 32: Geometry of soil domain

The choice of the soil domain size was governed by the avoidance of reflections at the boundaries of the soil domain. The dimension of the elements has been kept close to the ones used for the soil column, the elements being 2.5m in all directions. Close to the pile, a finer mesh has been used to capture the high gradients of the studied parameters. "PARAVIEW" [11] has been used as a post processor to track the displacements at the boundary of the soil domains. This geometry proved optimal for accuracy of results and computational time.

6.2 Dynamic sand-monopile interaction

Excess pore pressure In total, 13 analyses have been run, namely:

1. 125 gal earthquake only, both vertical and horizontal components;
2. 125 gal horizontal component earthquake only;
3. 125 gal earthquake, both vertical and horizontal components, combined with environmental;
4. 125 gal horizontal component earthquake combined with environmental;
5. 255 gal earthquake only, both vertical and horizontal components;
6. 255 gal horizontal component earthquake only;
7. 255 gal earthquake, both vertical and horizontal components, combined with environmental;
8. 255 gal horizontal component earthquake combined with environmental;
9. Tohoku earthquake, 480 gal, earthquake only, both vertical and horizontal components;
10. Tohoku horizontal component earthquake only;
11. Tohoku earthquake, both vertical and horizontal components, combined with environmental;
12. Tohoku horizontal component earthquake combined with environmental;

[11] https://www.paraview.org/

13. Environmental loading only.

By employing the 'U-P' formulation and the SaniSand 2004 model, pore pressure evolves due to (i) changes of the mean stress, (ii) drainage conditions, (iii) change of soil volume occurring under plastic shear loading controlled by a non-associative flow rule. In order to study the soil response, six different control points have been defined:

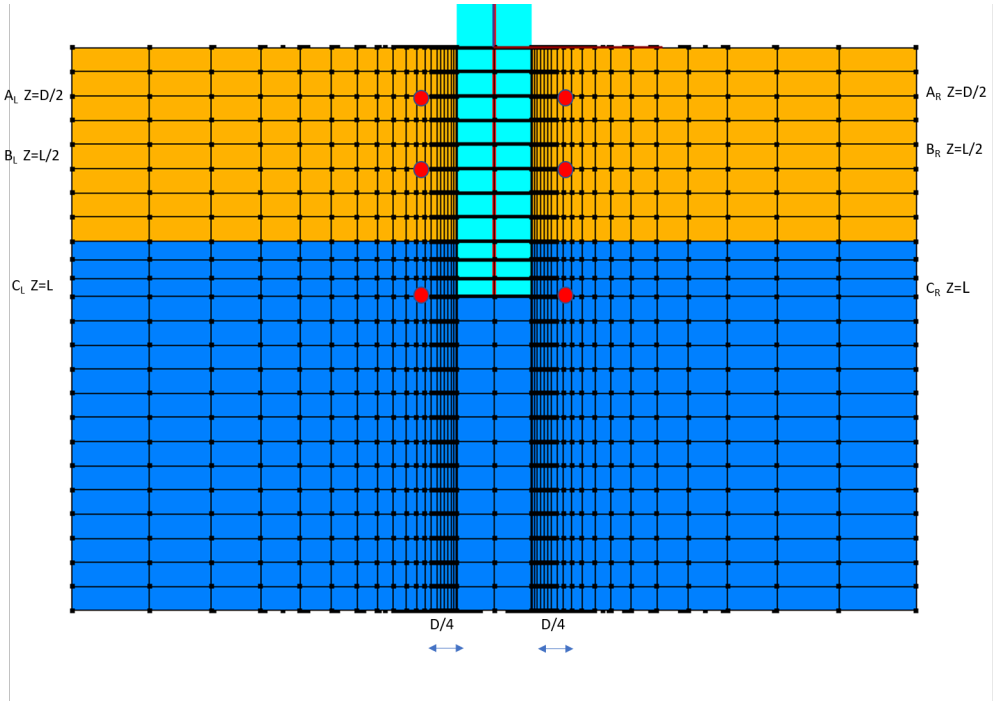

Figure 33: Positioning of the control points

.

One efficient way to track liquefaction in the soil is to plot u/p, where u is the pore water pressure and p is the total mean stress. If u/p=1, it means that there is no shear strength left in the soil, thus making the soil behave like a fluid and liquefying. In the case of a loose soil, this is possible. In the case studied in this thesis, due to the soil being very dense, this limit is not reached. Also, it should be noted that in a classical one way loading problem, there will always be a passive side (soil that is pushed away) and an active side (soil that slides towards the pile). In this classical case, the passive side will experience positive excess pore pressure due to shearing from the pile, while the soil behind the pile will experience negative excess pore pressures due to it "relaxing" and becoming less confined while the pile is moving away from it. As it can be seen, there is much more variation around the mean u/p ratio in the case of control points A_l and A_r. This happens because the soil at those points has a more pronounced dilative behaviour due to the small overburden pressure. At control points C_l and C_r this behaviour is much less pronounced due to the high overburden stress coming from the soil above, limiting its dilative behaviour. The high fluctuation around the mean is also explained by the cyclic nature of the load. After the soil is contracted to one side, upon load reversal, due to the new particle arrangement, it will be prone to dilation in the other direction.

The u/p evolution over time for the 3 earthquakes and the environmental loading only can be seen in Figures 34, 35, 36 37.

In order to study the influence of the presence of the vertical component and the environmental loads, let us plot u/p at control point A_R for all the 4 cases involving the Tohoku Earthquake (Figure 38).

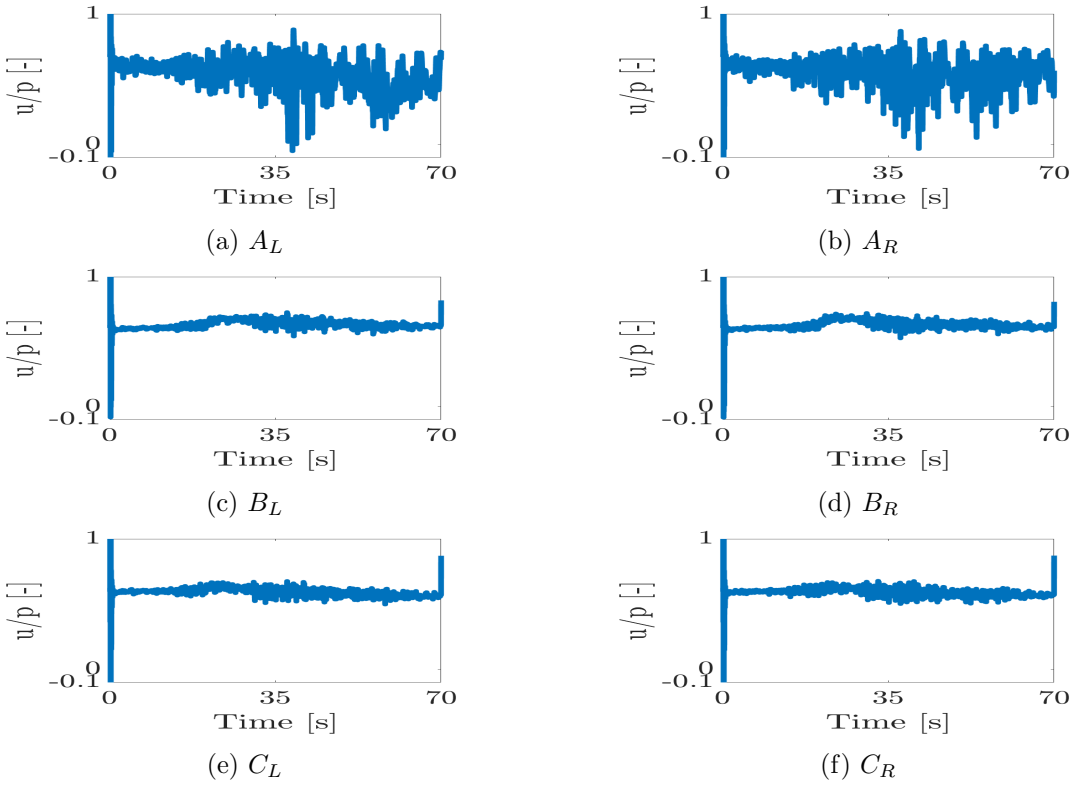

(a) A_L (b) A_R

(c) B_L (d) B_R

(e) C_L (f) C_R

Figure 34: u/p for all control points, Tohoku.

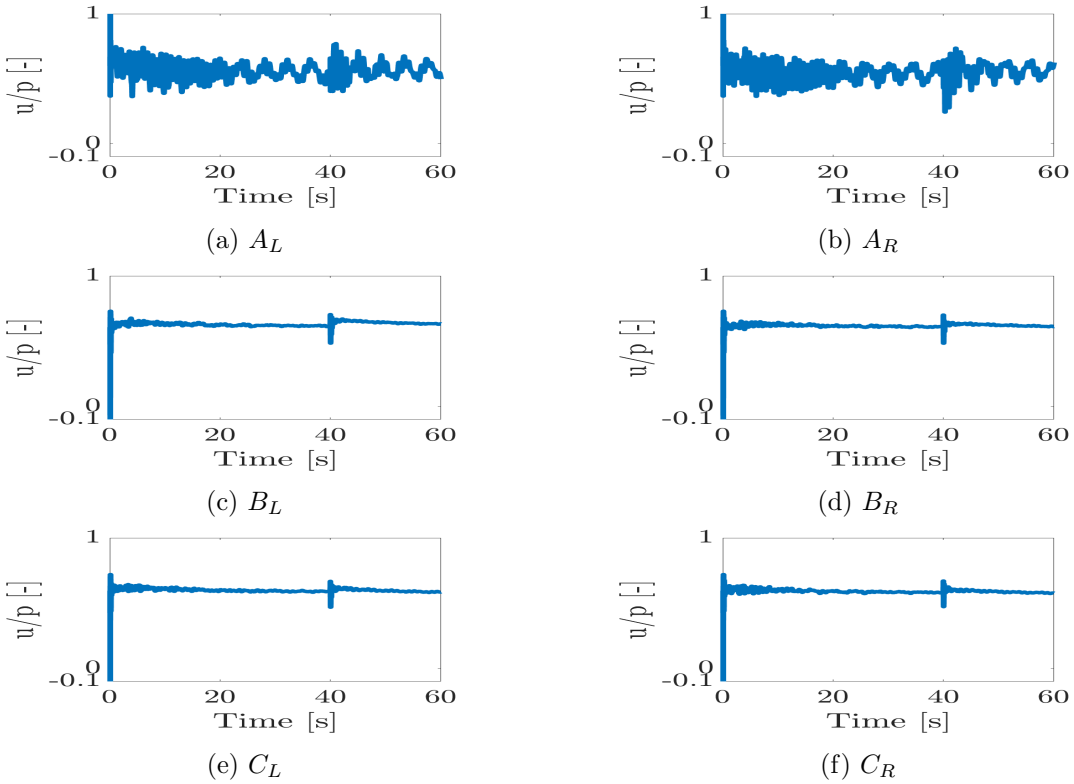

(a) A_L (b) A_R

(c) B_L (d) B_R

(e) C_L (f) C_R

Figure 35: u/p for all control points, 255gal.

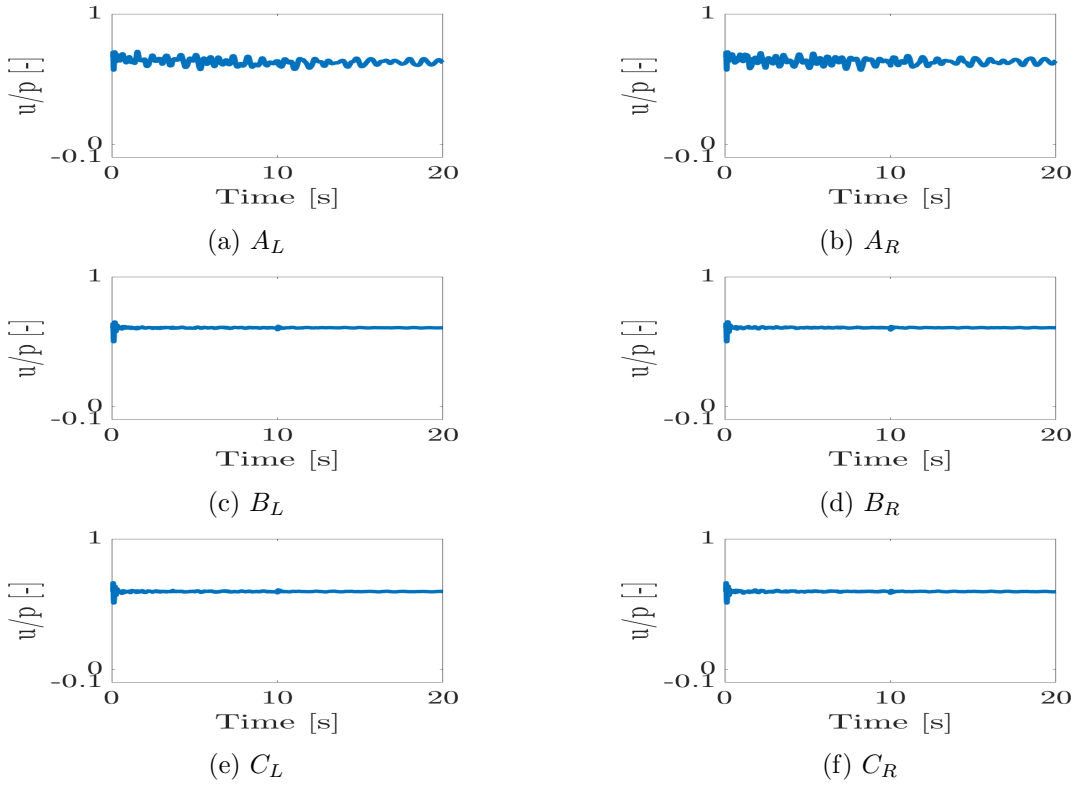

(a) A_L (b) A_R

(c) B_L (d) B_R

(e) C_L (f) C_R

Figure 36: u/p for all control points, 125gal.

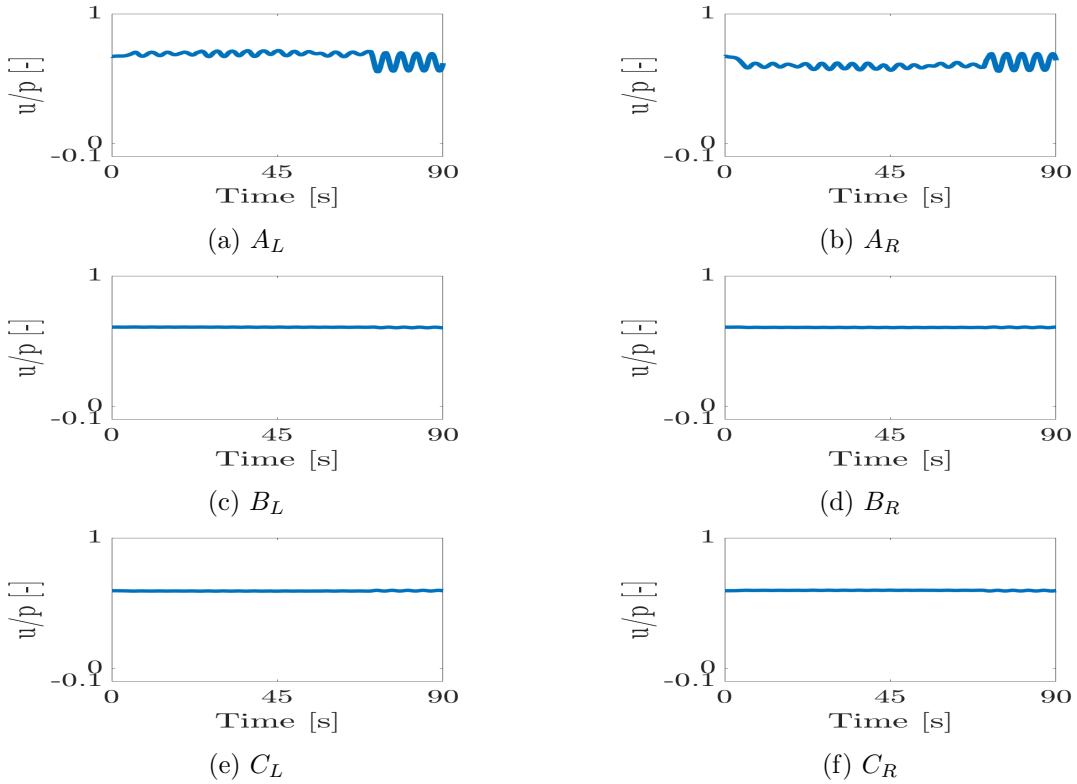

(a) A_L (b) A_R

(c) B_L (d) B_R

(e) C_L (f) C_R

Figure 37: u/p for all control points, environmental loading.

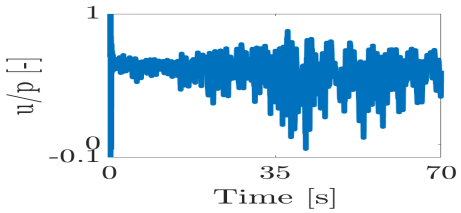

(a) Earthquake only

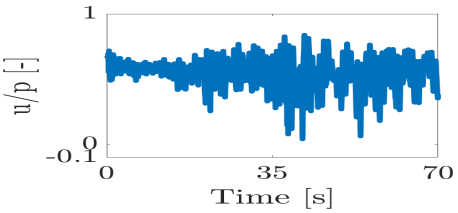

(b) Horizontal component only

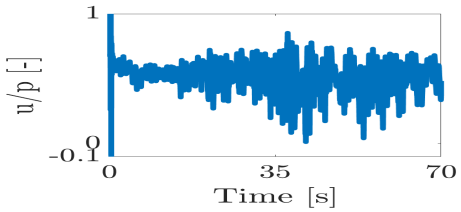

(c) Earthquake combined with environmental

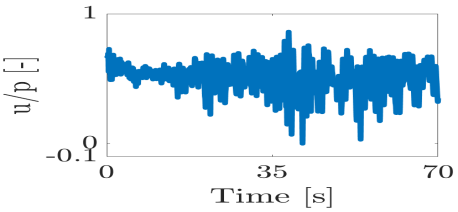

(d) Horizontal component combined with environmental

Figure 38: u/p for control point A_R, loading scenarios involving Tohoku earthquake.

As one would expect, the biggest pore pressure fluctuation is during the strong loading period (30s-40s), going to a negative u/p ratio. A negative u/p ratio suggests that the negative excess pore pressures generated are bigger than the steady state compressive pore pressure. It is important to notice that even if the excess pressure goes negative, there is no prediction of cavitation, as the water column above the mudline is 30 metres. Also, the frequency content of the earthquake with both components active is richer than the frequency content of horizontal component only. That is because the vertical component agitates directly the pore water pressures, while the horizontal one influences it through plasticity.

Spatial distribution of pore pressures The transient evolution of pore pressures shows similar behaviour across all earthquakes at the control points considered. The control points are located one fourth of a monopile diameter away from the monopile and, thus, experience heavy loading during the scenarios. In order to obtain a clear picture on the influence area of the monopile, the pore pressure field for the 3 different earthquakes is depicted Figure 39. It is evident that the width of the pile influence area is directly affected by the PGA of the seismic motion. The narrowness and wideness of the pore pressure field should be attributed to the capacity and stiffness of the surrounding soil. Depending on the stiffness and capacity of the soil, it will tend to distribute the stresses caused by the loads in a larger or smaller area in order to reach equilibrium.

Stress paths The stress response of the soil to the three earthquakes and environmental loading separately can be seen in Figures 40, 41, 42 and 43. By taking a closer look at the figures, it can be seen that the only earthquake that has caused the effective stress to get close to zero is the Tohoku Earthquake during the 30-40 seconds interval of the earthquake, where the highest amplitudes of the motion are concentrated. This is caused by the monopile head having high displacements and shearing the soil. At the end of the high motion interval, due to the soils dilative nature, it regains its strength, ending the simulation at a higher p' than the one experienced during the strong shaking. The soil around the top control points experiences plastic deformations during this shearing phase, which is confirmed by the figures from the postprocessor. At the other control points, the soil does not experience drops in mean effective stress to such low levels. The environmental loads in such a stiff soil are close to irrelevant, if one was to compare their effect to the earthquake loads. This will be proven during the rest of the report.

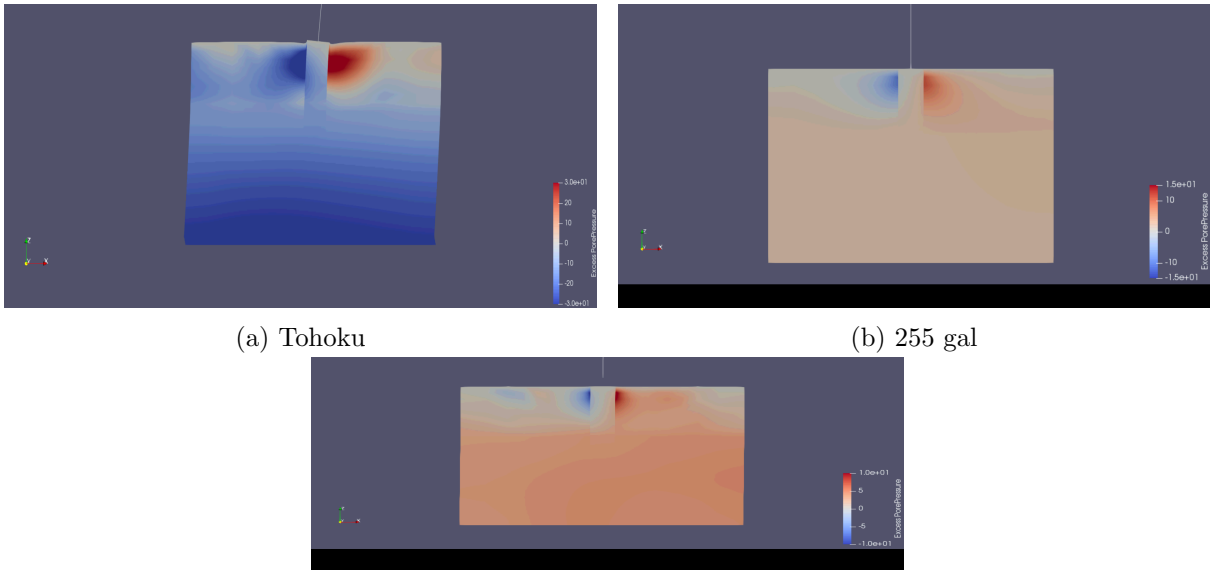

(a) Tohoku (b) 255 gal

(c) 125 gal

Figure 39: Monopile influence area

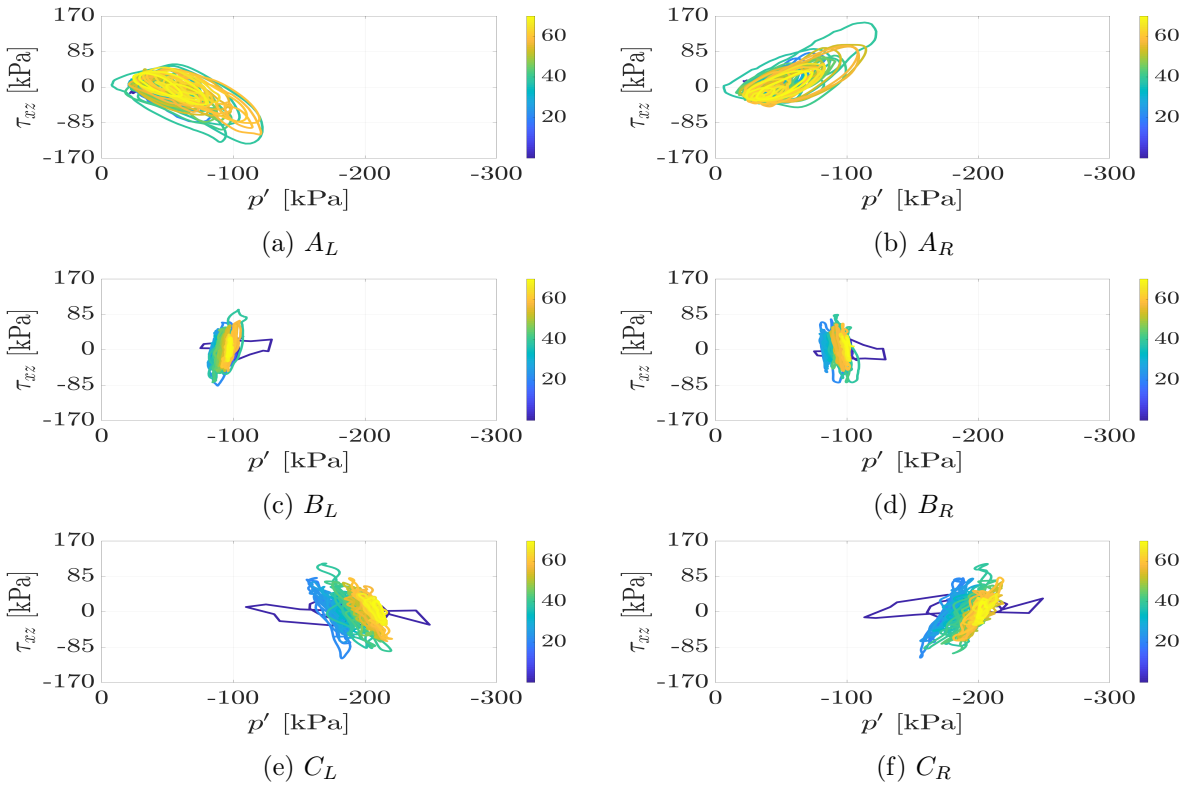

(a) A_L (b) A_R

(c) B_L (d) B_R

(e) C_L (f) C_R

Figure 40: Stress paths of $\tau_{xz} - p'$ for all control points, Tohoku. The colobars indicate time.

In order to study the influence of the presence of the vertical component and the environmental loads, let us plot $\tau_{xz} - p'$ at control point A_R for all the 4 cases involving the Tohoku Earthquake.

As it can be seen in Figure 44, there is no significant difference between the 4 cases. The presence of wind and waves bring only a slight change in the result, increasing shear stress.

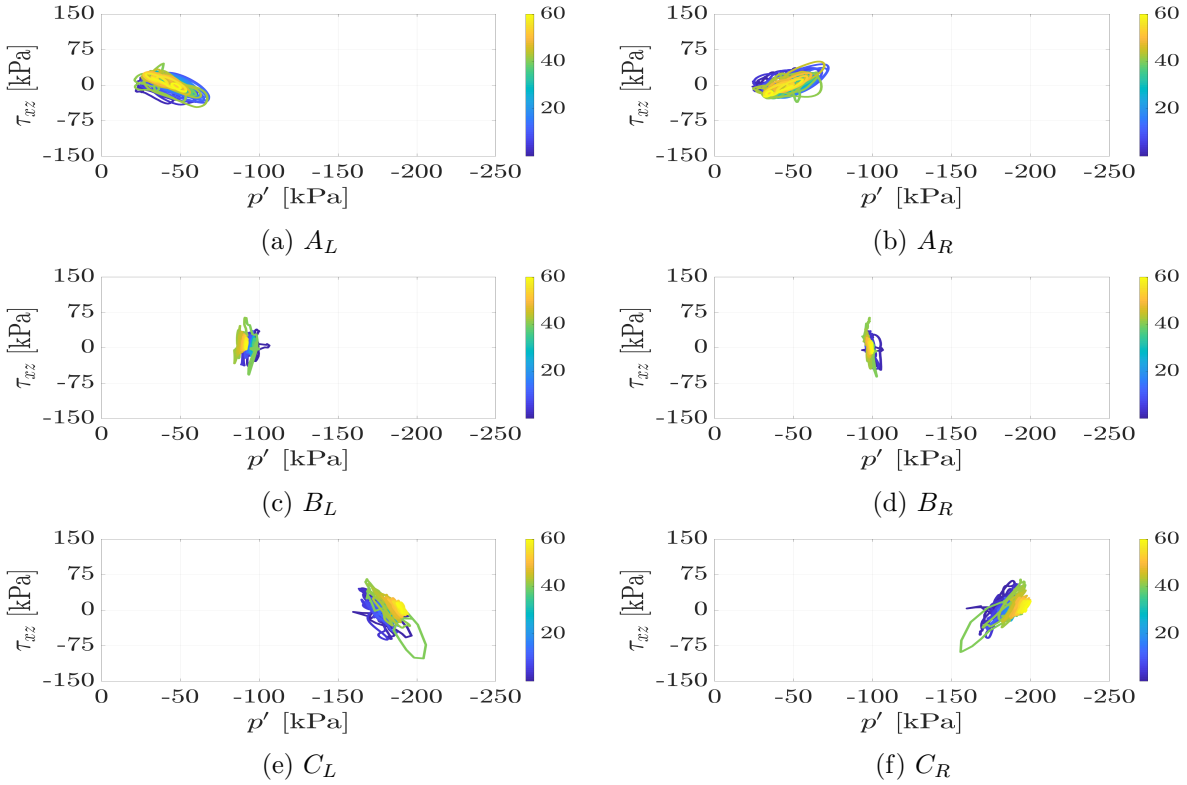

(a) A_L (b) A_R

(c) B_L (d) B_R

(e) C_L (f) C_R

Figure 41: Stress paths of $\tau_{xz} - p'$ for all control points, 255gal. The colobars indicate time.

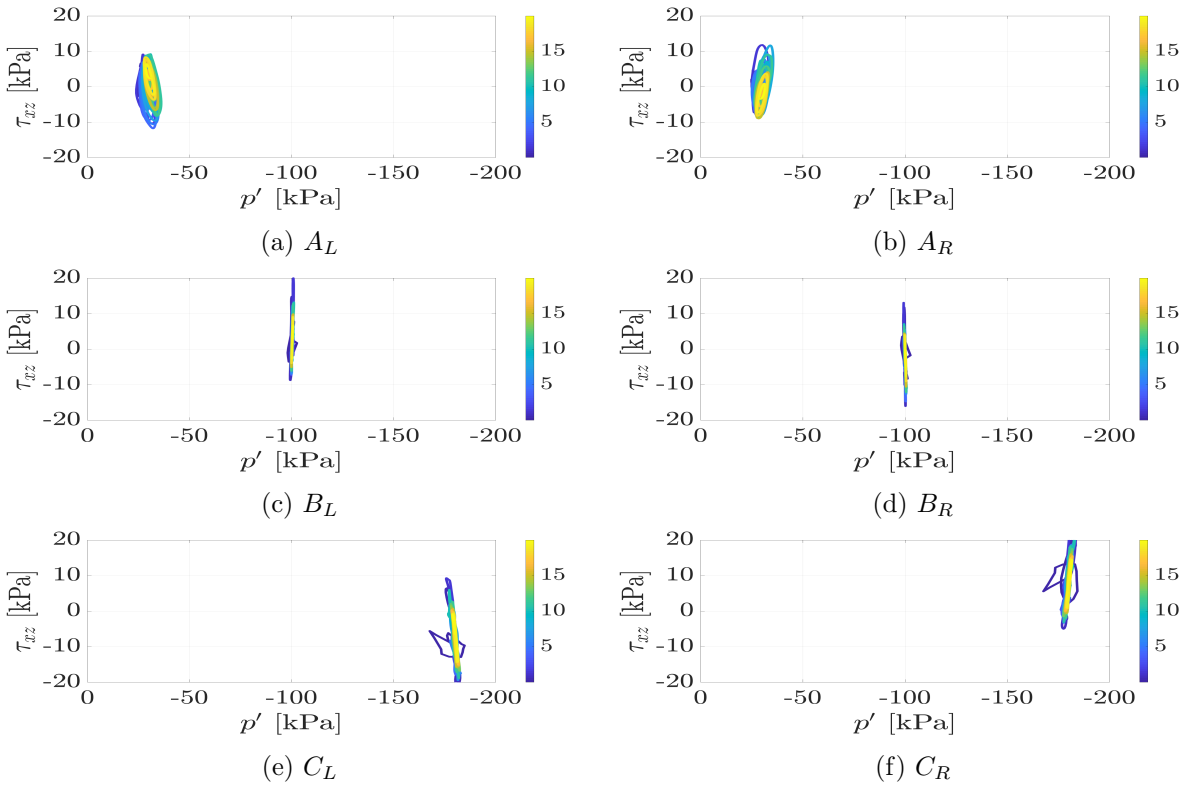

(a) A_L (b) A_R

(c) B_L (d) B_R

(e) C_L (f) C_R

Figure 42: Stress paths of $\tau_{xz} - p'$ for all control points, 125gal. The colobars indicate time.

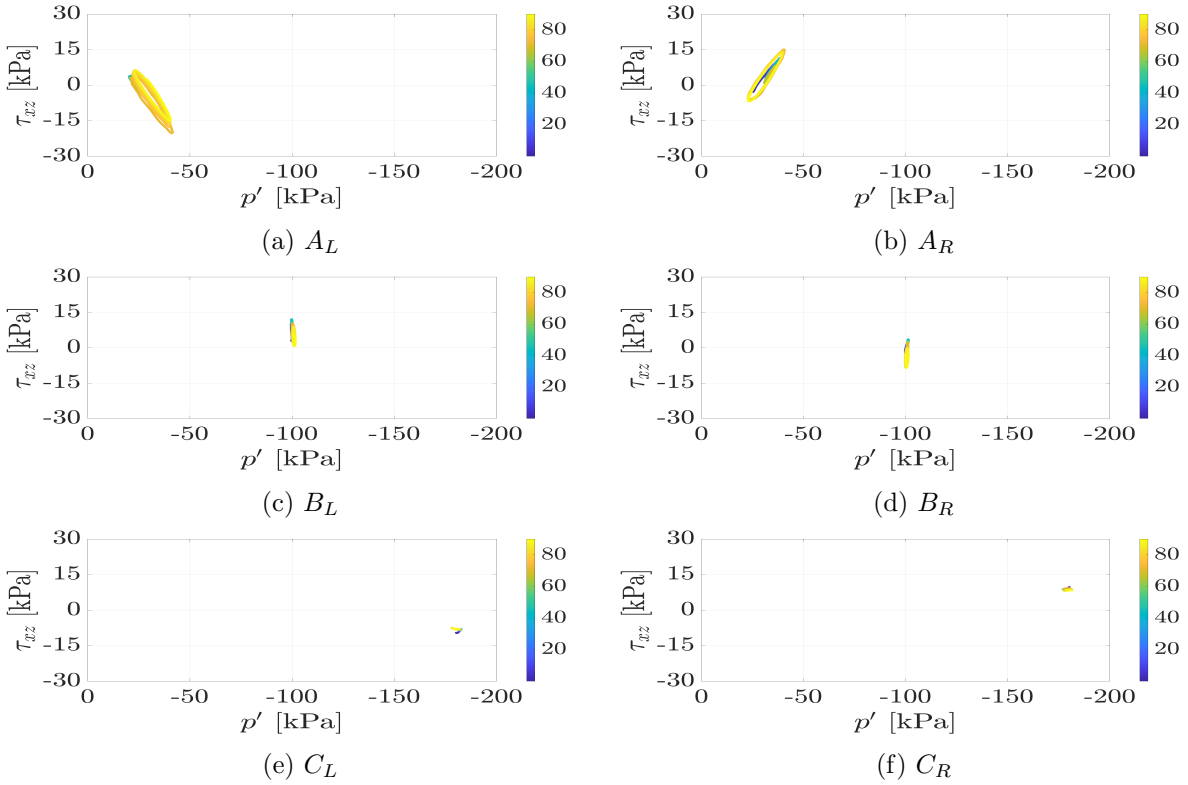

(a) A_L (b) A_R

(c) B_L (d) B_R

(e) C_L (f) C_R

Figure 43: Stress paths of $\tau_{xz} - p'$ for all control points, environmental loading. The colobars indicate time.

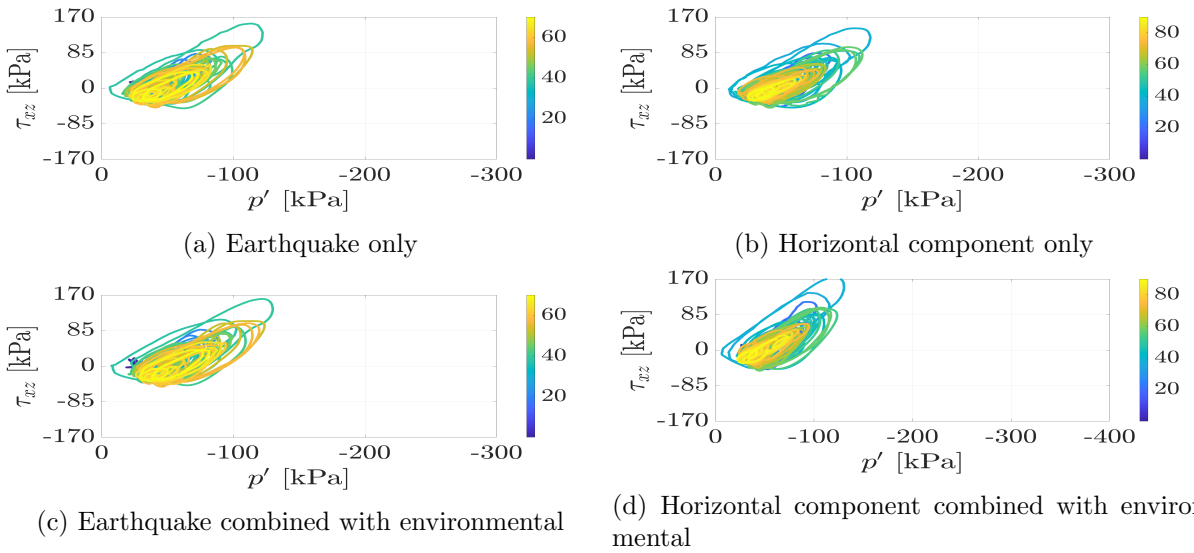

(a) Earthquake only (b) Horizontal component only

(c) Earthquake combined with environmental

(d) Horizontal component combined with environmental

Figure 44: Stress paths of $\tau_{xz} - p'$ for control point A_R, loading scenarios involving Tohoku earthquake. The colobars indicate time.

Stress-strain Stress strain response of the soil at the control points is depicted by $\tau_{xz} - \gamma_{xz}$ plots seen in Figures 45, 46, 47, 48, 49.

As it can be seen in the figures just mentioned, the soil response is very stiff for all cases except the Tohoku Earthquake. There is no non-linearity in the environmental response, while very little non-linearity is present near the pile head for the 255 gal earthquake. In the case of the Tohoku

earthquake, the response near the pile head is highly non-linear, proven by the slope changes at control points A_L and A_R and the postprocessor. The slope of the graph is almost horizontal during the strong shaking interval of the Tohoku Earthquake. The area around the pilehead sunk, due to plasticity induced by shearing.

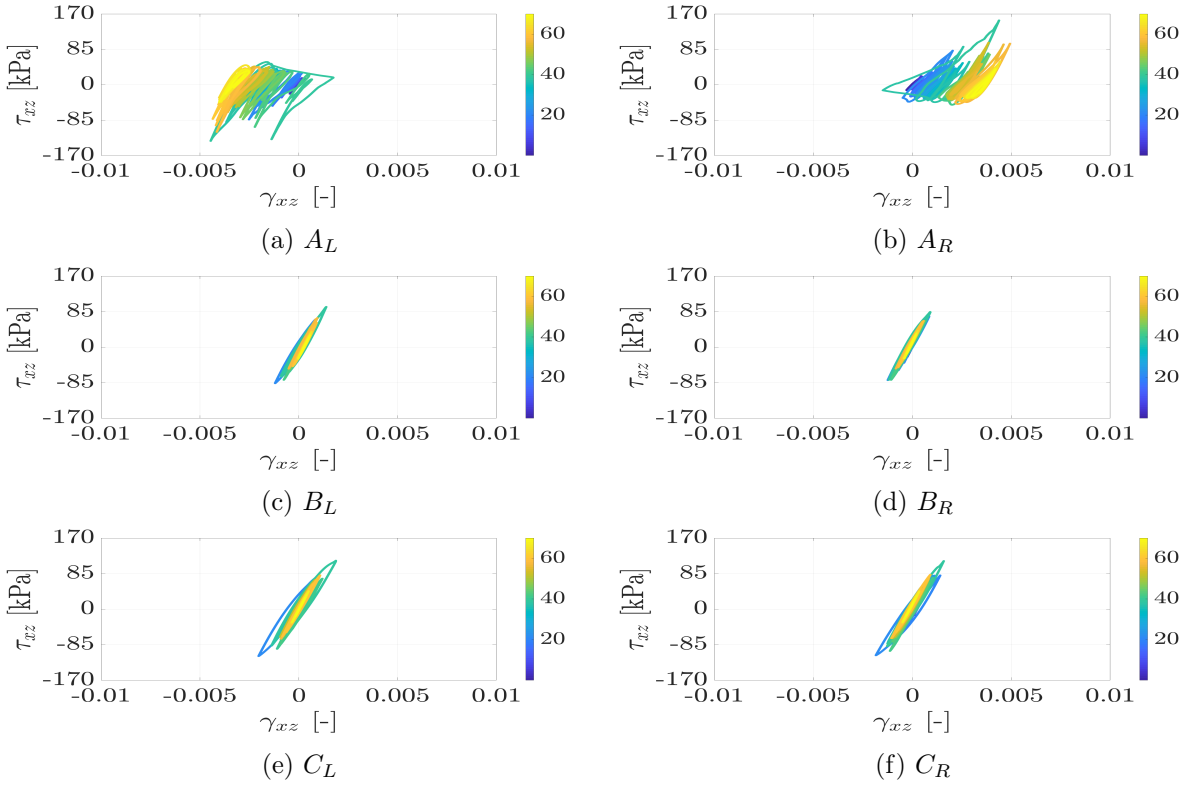

(a) A_L (b) A_R

(c) B_L (d) B_R

(e) C_L (f) C_R

Figure 45: Stress paths of $\tau_{xz} - \gamma_{xz}$ for all control points, Tohoku. The colobars indicate time.

Similarly to the stress path procedure, let us plot $\tau_{xz} - \gamma xz$ at control point A_R for all the 4 cases involving the Tohoku Earthquake.

6.2.1 Hub response

An interesting thing to look at is the hub displacement, in order to see if earthquakes could generate considerable displacements in comparison with standard environmental loads. A comparison between the three earthquakes and environmental loads can be seen in Figure 50

By looking at Figure 50, an interest remark can be drawn. An earthquake with a big enough PGA can trigger hub displacements similar to that of SLS wind conditions. In order to have a better understanding of these results, let us look into the dynamic of this system.

Kementzetzidis (2017) performed an eigenanalysis for this specific turbine, in fixed base conditions. The results are reported in Table 7

In order to get an understanding of the dynamics of the system, let us start with the Stockwell transform of the seismic input shown in Figures 51 and 52.

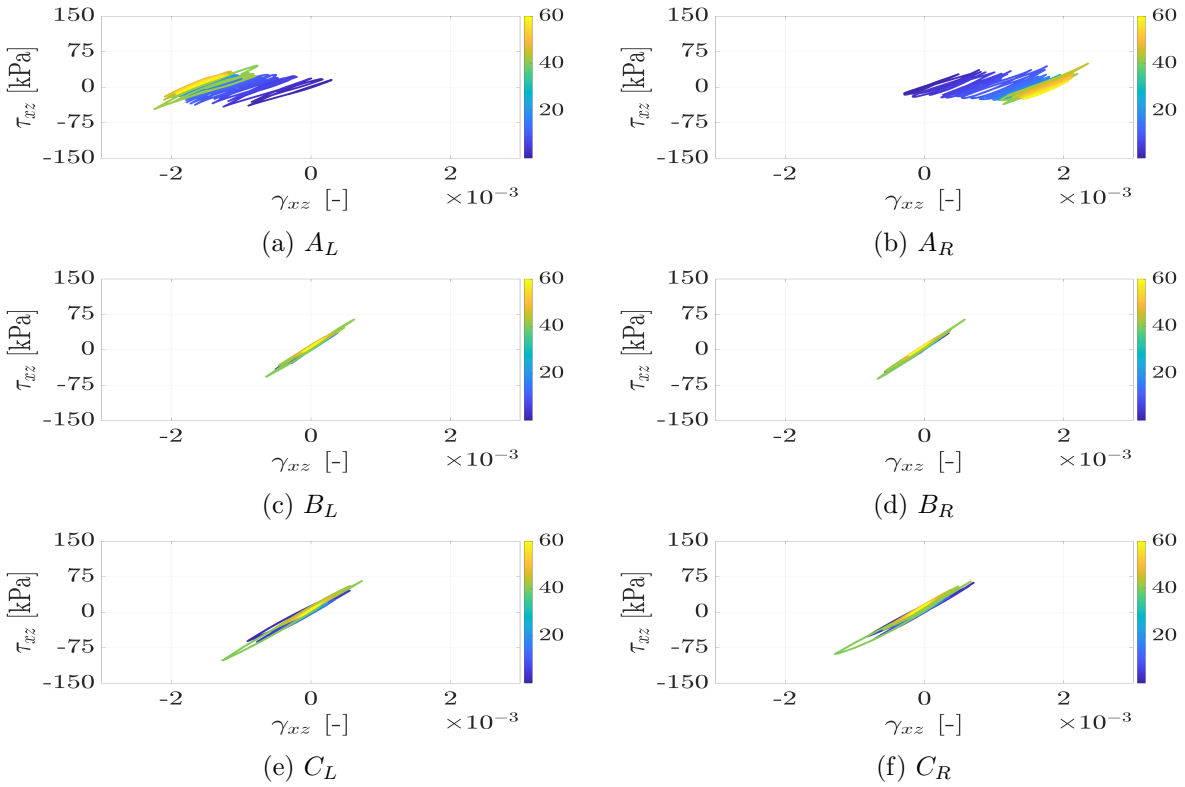

(a) A_L (b) A_R

(c) B_L (d) B_R

(e) C_L (f) C_R

Figure 46: Stress paths of $\tau_{xz} - \gamma_{xz}$ for all control points, 255gal. The colobars indicate time.

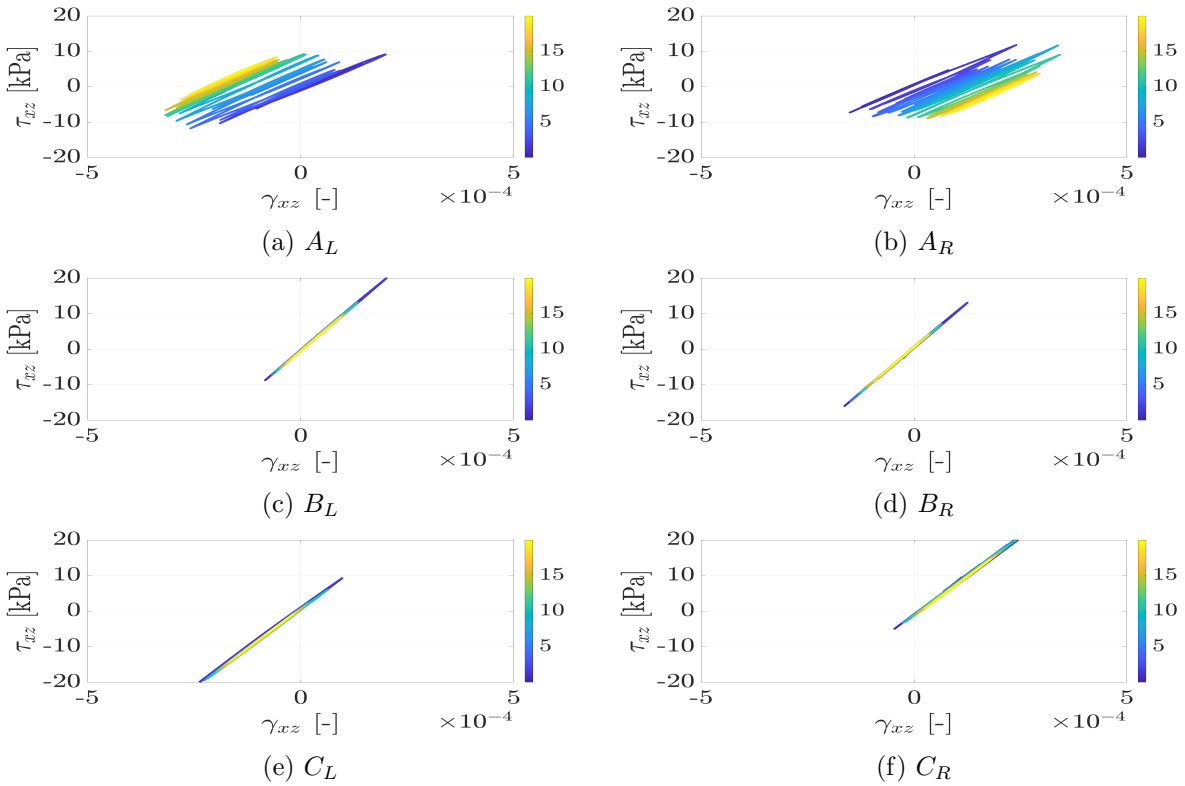

(a) A_L (b) A_R

(c) B_L (d) B_R

(e) C_L (f) C_R

Figure 47: Stress paths of $\tau_{xz} - \gamma_{xz}$ for all control points, 125gal. The colobars indicate time.

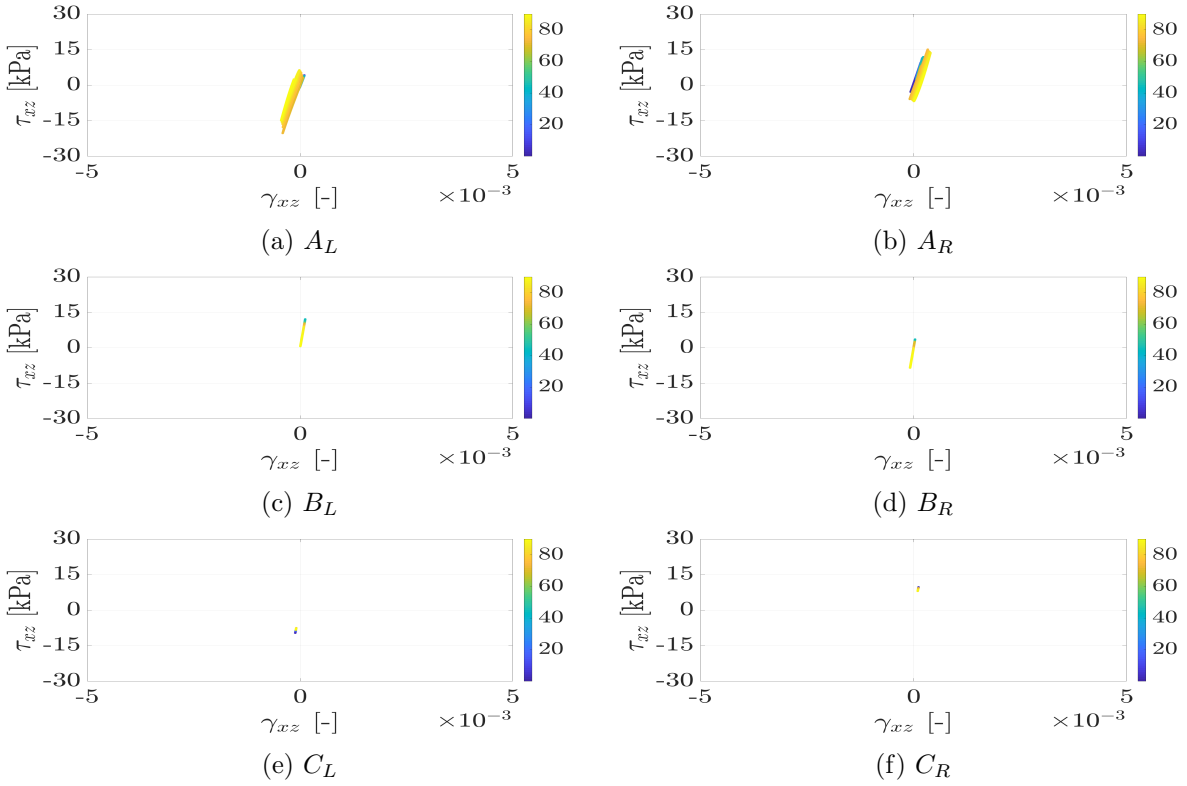

(a) A_L (b) A_R

(c) B_L (d) B_R

(e) C_L (f) C_R

Figure 48: Stress paths of $\tau_{xz} - \gamma_{xz}$ for all control points, environmental loading. The colobars indicate time.

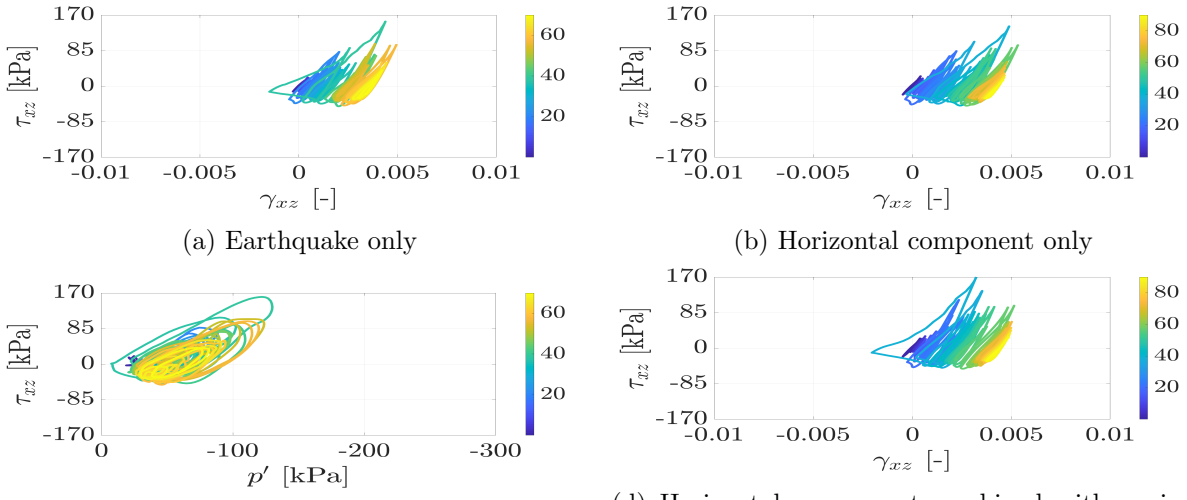

(a) Earthquake only (b) Horizontal component only

(c) Earthquake combined with environmental (d) Horizontal component combined with environmental

Figure 49: Stress paths of $\tau_{xz} - \gamma_{xz}$ for control point A_R, loading scenarios involving Tohoku earthquake. The colobars indicate time.

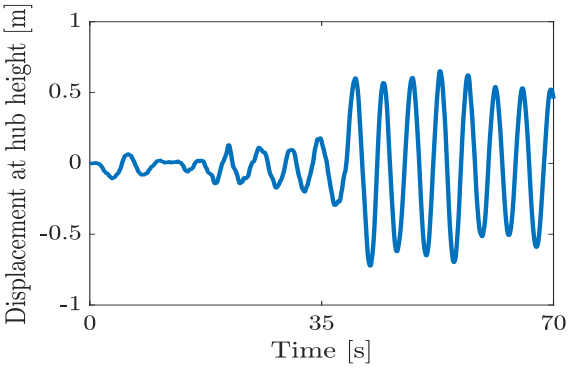

(a) Tohoku

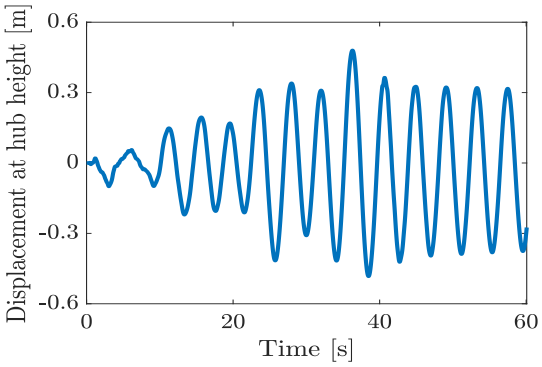

(b) 255 gal

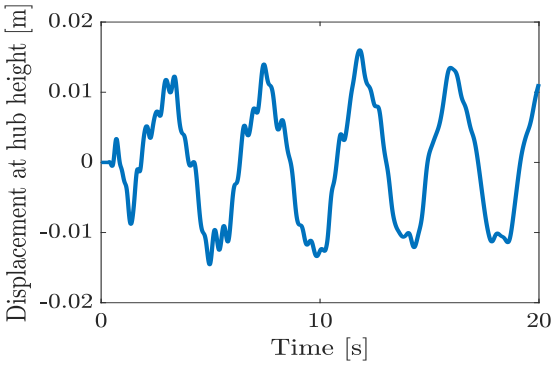

(c) 125 gal

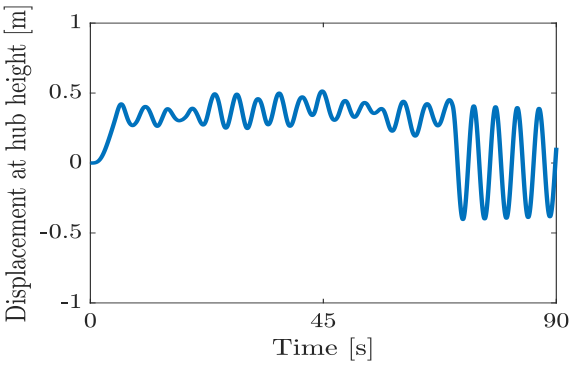

(d) environmental

Figure 50: Hub displacement horizontal direction

Table 7: System eigenperiods

Mode	Period (s)
1	4.59
2	0.83
3	0.40
4	0.20
5	0.16

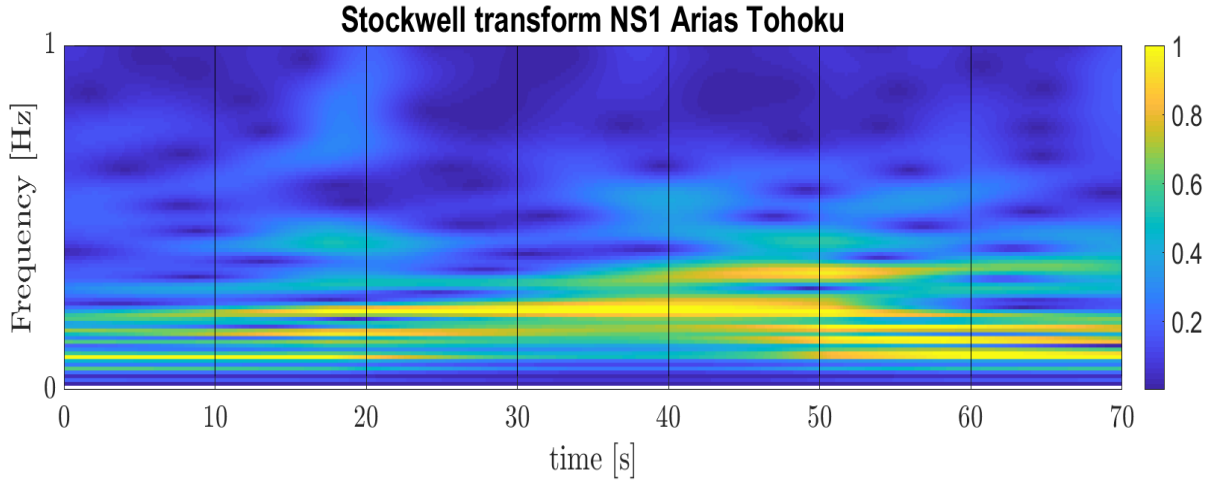

(a) Tohoku

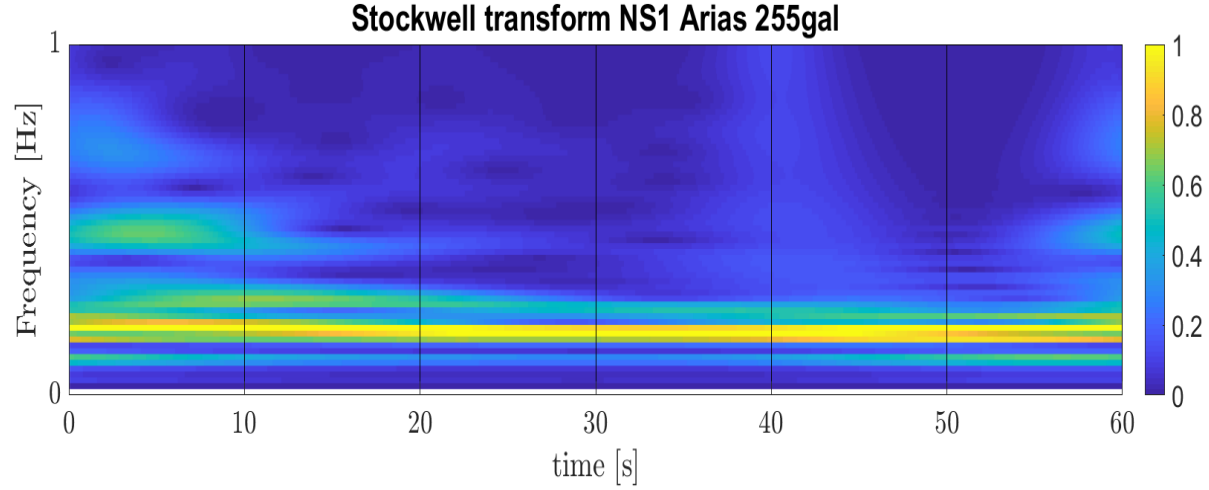

(b) 255 gal

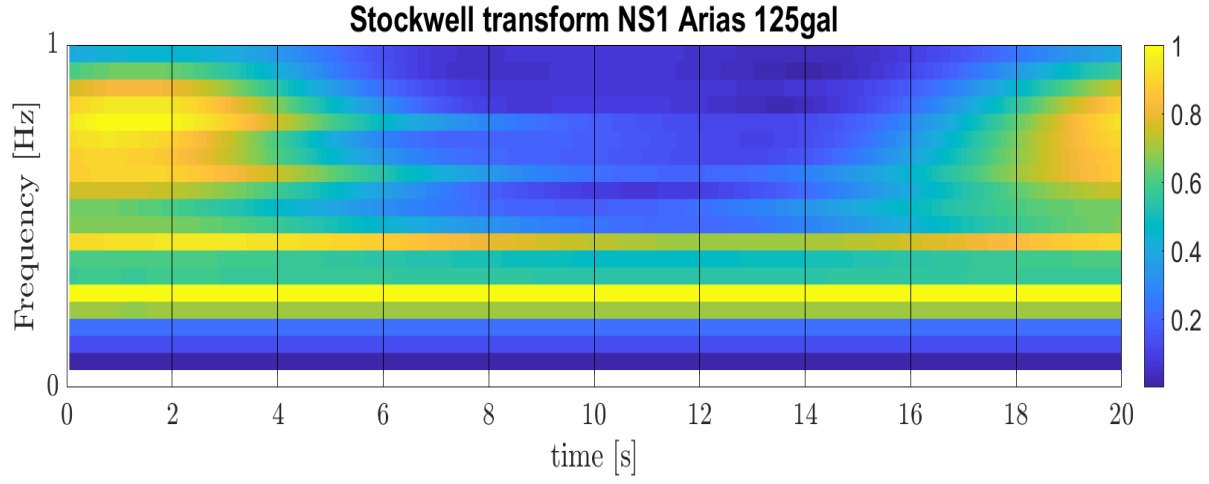

(c) 125 gal

Figure 51: Stockwell transforms of the input motion NS direction. Colorbar indicates normalised magnitude

Considering that the input motions for the system are displacement, the Stockwell transform has been plotted only until 1Hz, because, as shown in previous sections, the frequency content of

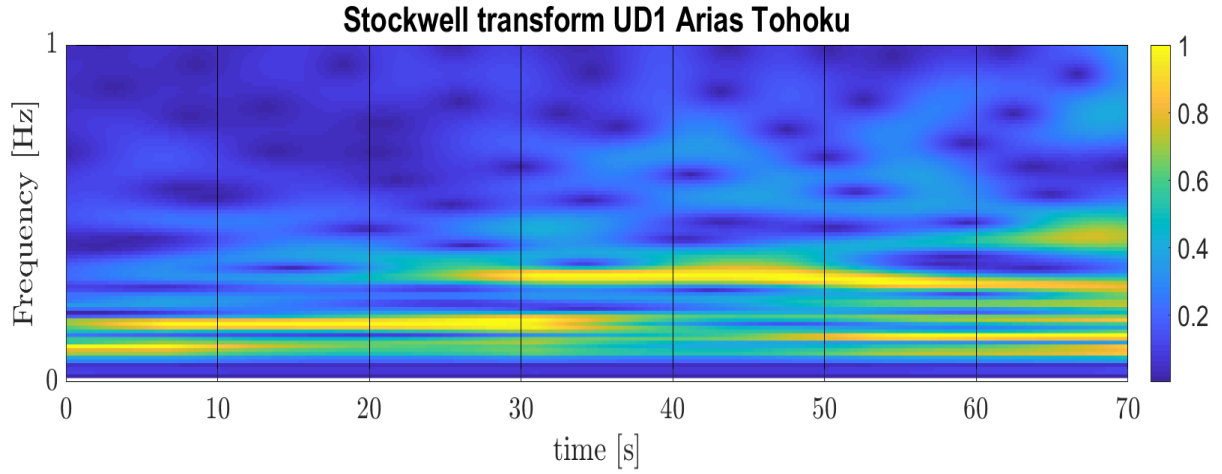

(a) Tohoku

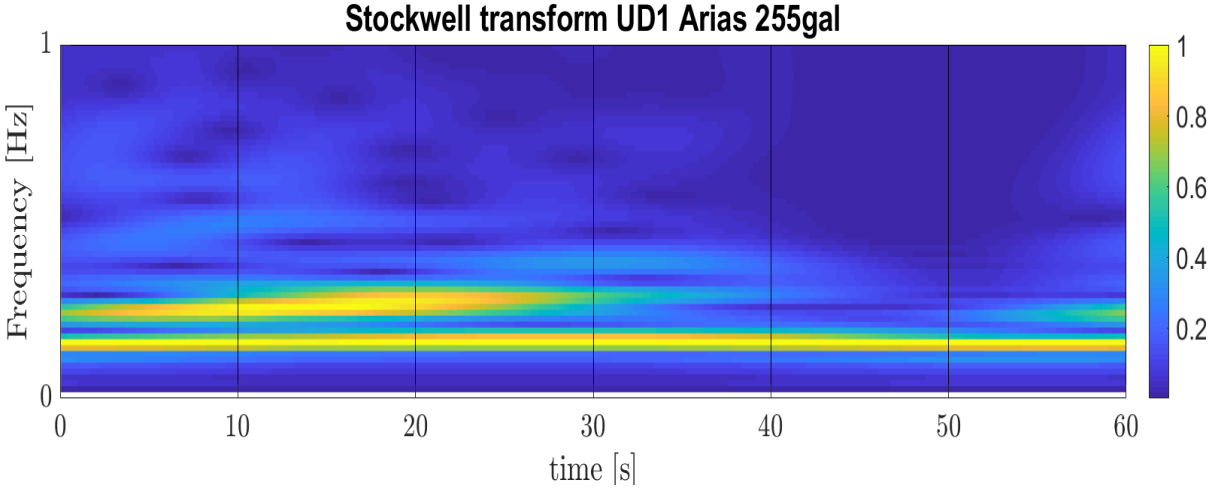

(b) 255 gal

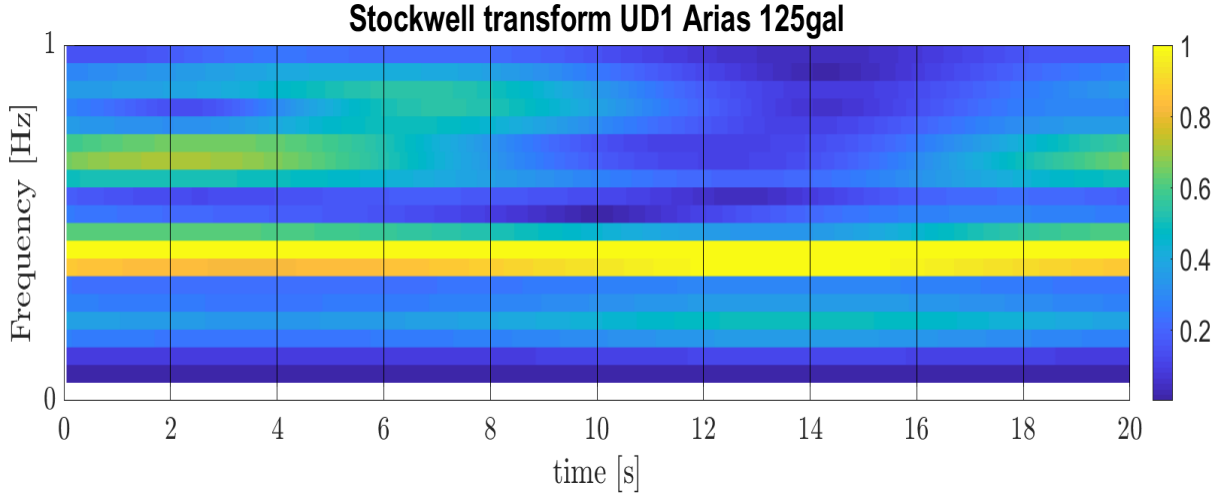

(c) 125 gal

Figure 52: Stockwell transforms of the input motion UD direction.The colobars indicate normalised magnitude

the displacement time histories cap around 1 Hz. The Tohoku earthquake is rich in frequencies around 0.5 Hz, while the 255 gal earthquake is more constant in frequencies around 0.2 Hz. The 125 gal motion is the richest in frequency content, containing frequencies close to 1 Hz. This can be confirmed by the hub displacement in the case of the 125 gal earthquake which has a very "jiggly nature".

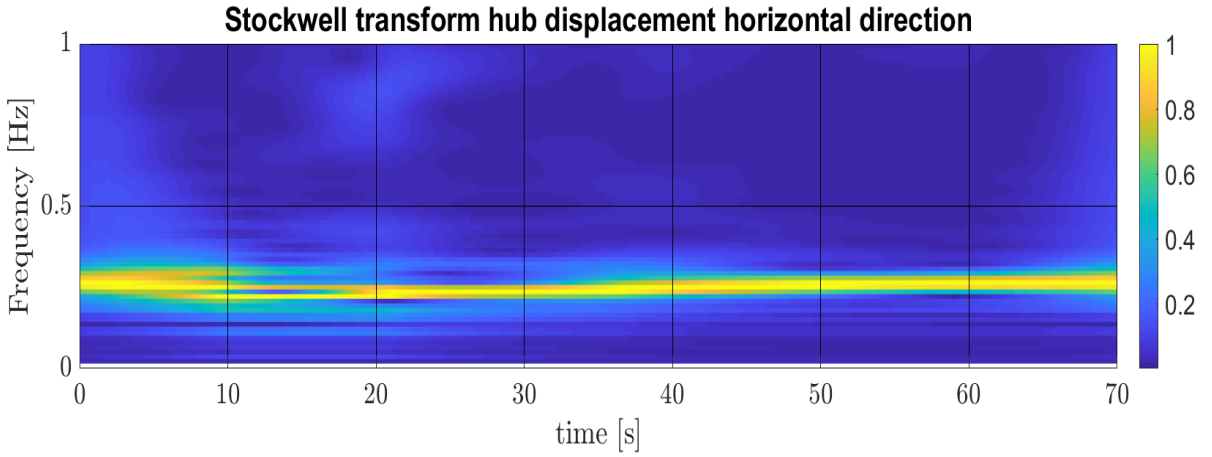

(a) Tohoku

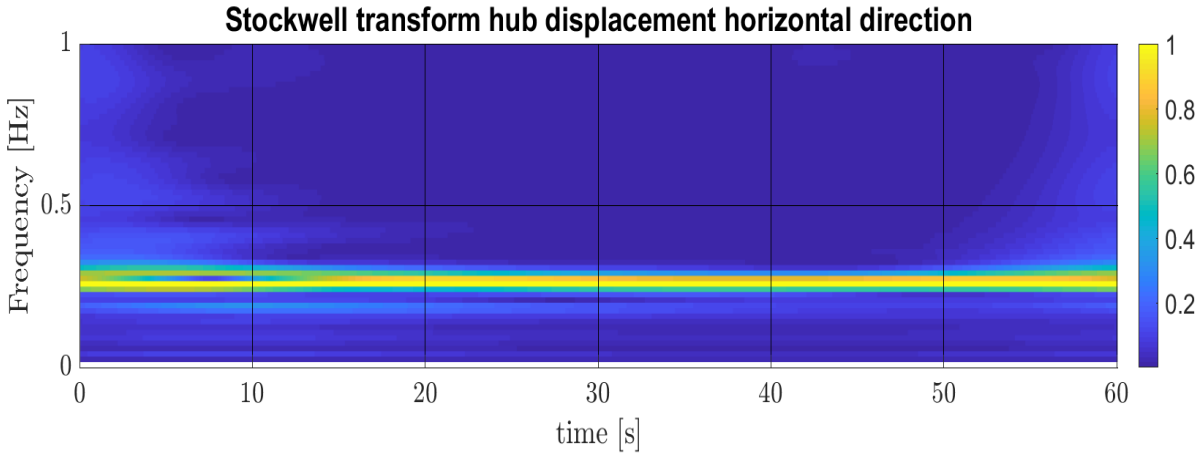

(b) 255 gal

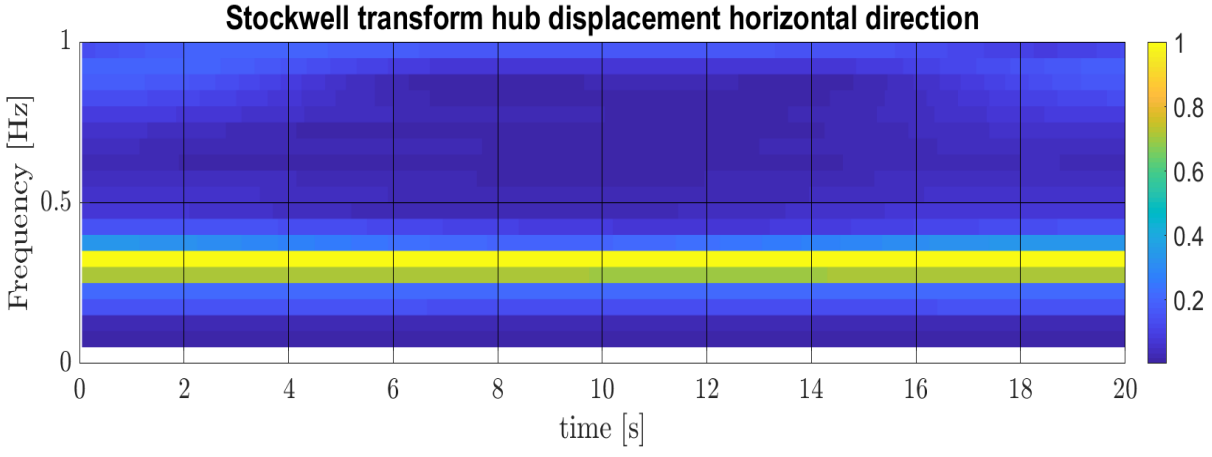

(c) 125 gal

Figure 53: Stockwell transforms of the hub displacement in the horizontal direction

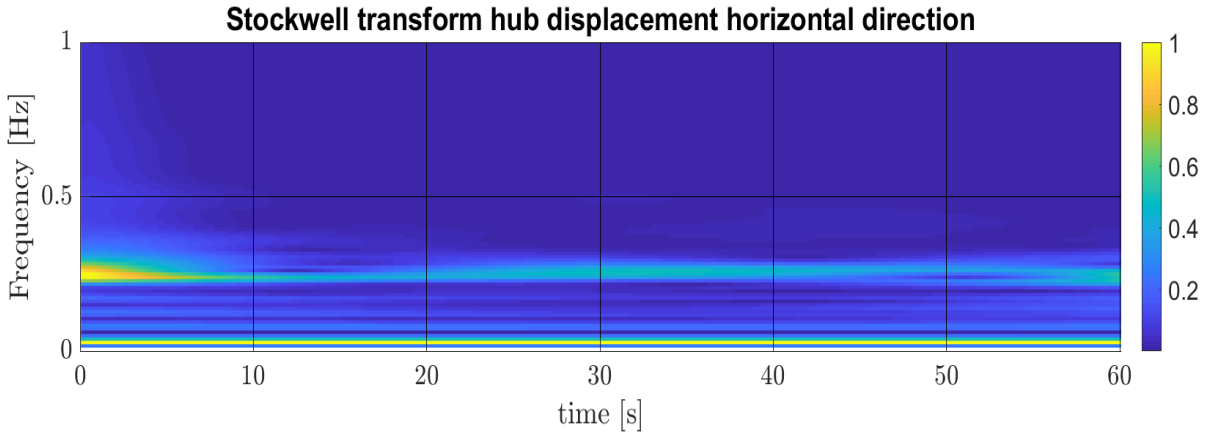

Figure 54: Stockwell transforms of the hub displacement in the horizontal direction environmental loading

In Figures 53 and 54, the S-transform of the hub displacement in the horizontal direction is presented for the earthquakes and the environmental loading separately.

In all the cases, the response is dominated by the first mode of the turbine. That is to be expected, due to it being a cantilever-like structure with the biggest mass lumped at the top. For this geometry, horizontal displacement at the top will always be dominated by the first mode. An interesting observation is that in the 255 gal and 125 gal cases, there is no significant shift in the resonance of the system, while in the Tohoku case, there is a clear increase in natural frequency after the heavy loading of the 30-40 seconds interval, which causes high dilative pore pressures to develop, stiffening the system. The response patterns are very stable in time for the 125gal and 255 gal earthquakes together with environmental loading, due to not much soil non-linearity being mobilised.For the environmental load, one can see that the energy is no longer concentrated in the first mode. That is due to the frequency content of the environmental loads, that do not coincide with those of the excited system. Even if there is amplification in the transfer function of the turbine at that frequency, the energy content of that input at that frequency is not significant, resulting in a not so strong response at that frequency. Let us remind that in order to do a complete wind and wave analysis, a 600 seconds analysis should be run, so our wind time history does not contain all the frequencies necessary for an accurate response.

As in previous sections, inclusion of environmental loads, or analyzing the horizontal component only does not induce a big difference in response from a dynamic point of view.

6.2.2 Monopile head response

Of crucial interest from a geotechnical engineering perspective is the pile-head response. The pile-head displacements in the case of earthquakes and environmental loads only can be seen in Figure 55.

An interesting thing to notice in Figures 55 and 56 is how insignificant the environmental load is in comparison with a medium PGA ground motion. In terms of forces, the force experienced at the pile head is 20 times smaller in comparison to the Tohoku Earthquake (20mN vs 1 mN) and the displacement is 4mm in comparison with 25 cm. Is is noticeable that the force-displacement plots are "messier" in the seismic case due to higher inertial effects transmitted by the superstructure (inertial interaction). That is not the case for slow environmental motion.

Similarly, one can look at the Pilehead rotation, depicted in Figure 56.

Non-linearity is evident from Figure 56. There are clear changes of slope in the Tohoku graph. Stiffness is lost during the strong shaking, but regained shorty after due to the dilative behaviour

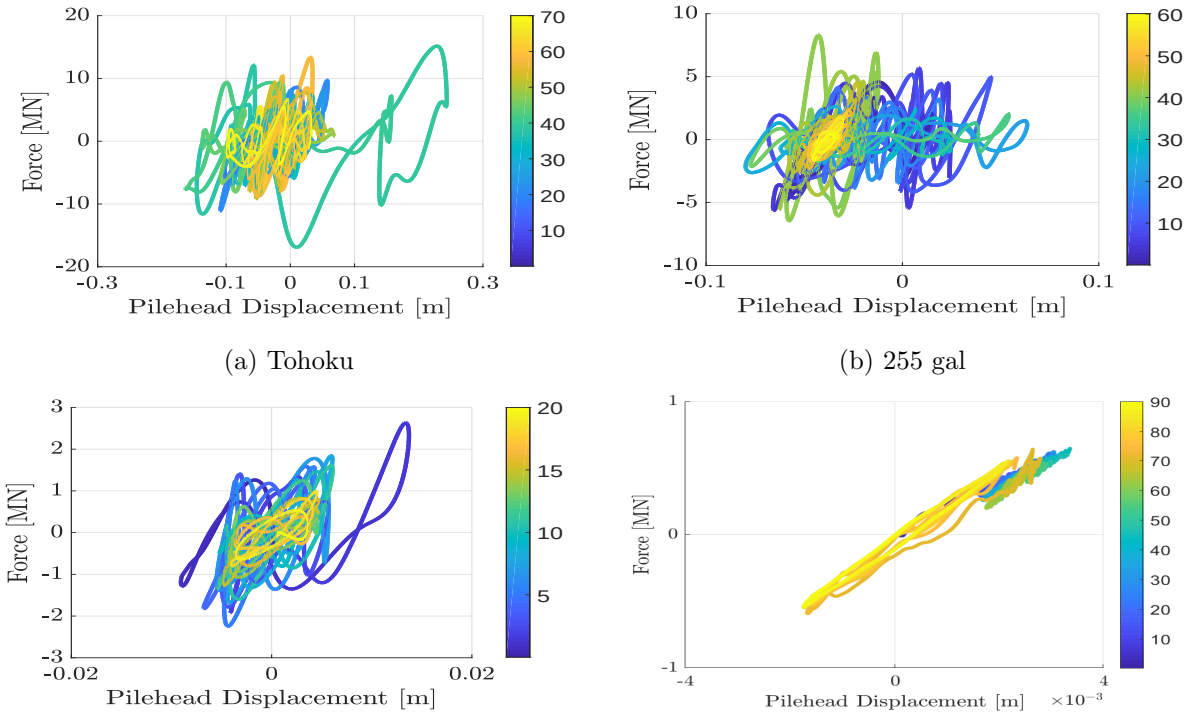

(a) Tohoku (b) 255 gal

(c) 125 gal (d) environmental

Figure 55: Monopile head Force-displacement diagram. The colorbars indicate time.

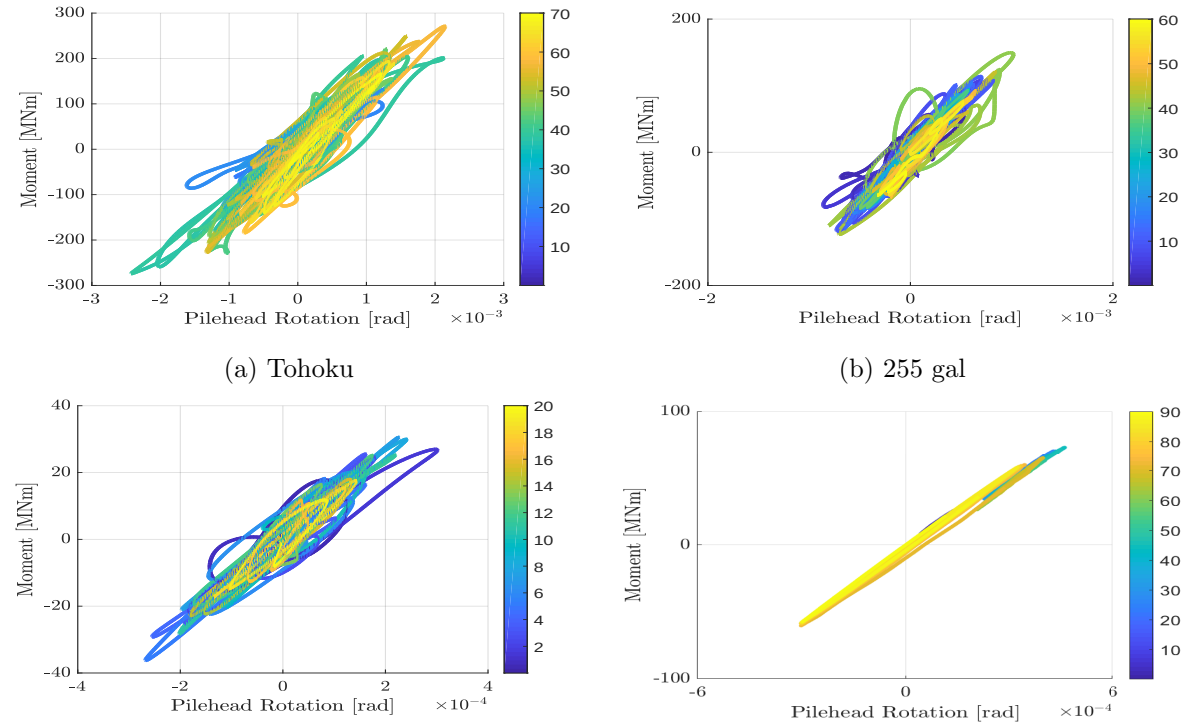

(a) Tohoku (b) 255 gal

(c) 125 gal (d) environmental

Figure 56: Monopile head Moment-rotation diagram. The colorbars indicate time.

of the soil. Again, the moment at the pilehead is 4 times bigger in case of the Tohoku Earthquake,

while the rotation is an order of magnitude bigger as well.

Too see the dynamic response at the pile-head, let us look into the S-transforms of the displacements.

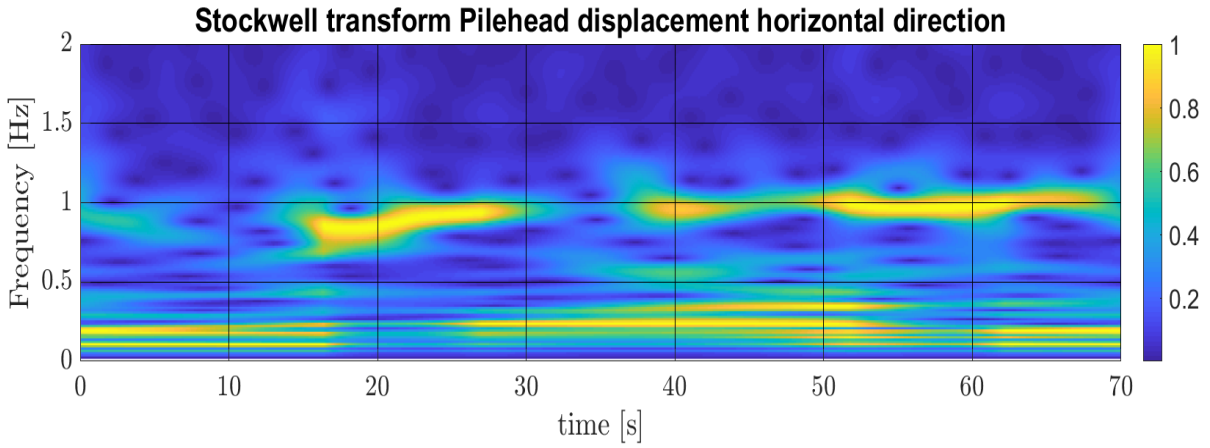

(a) Tohoku

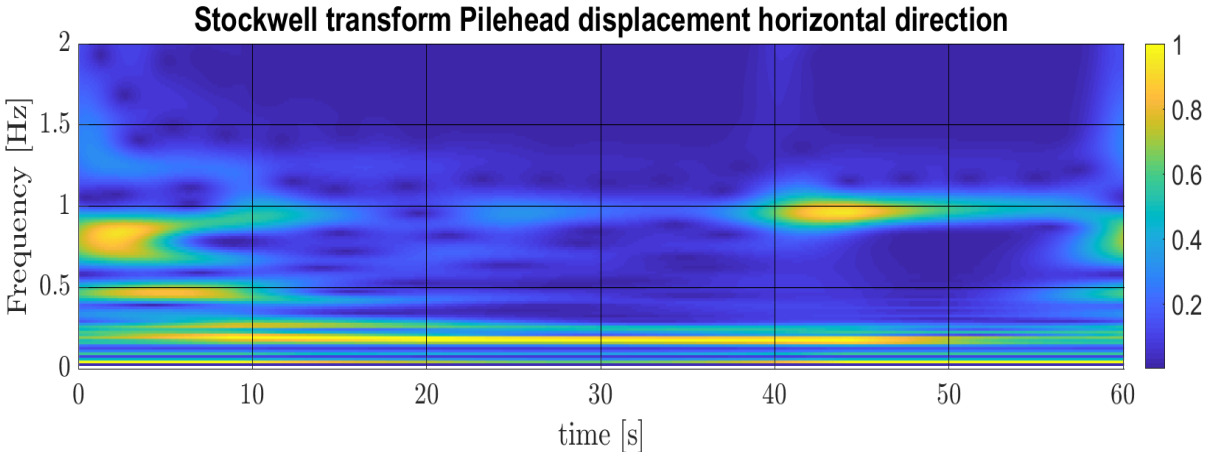

(b) 255 gal

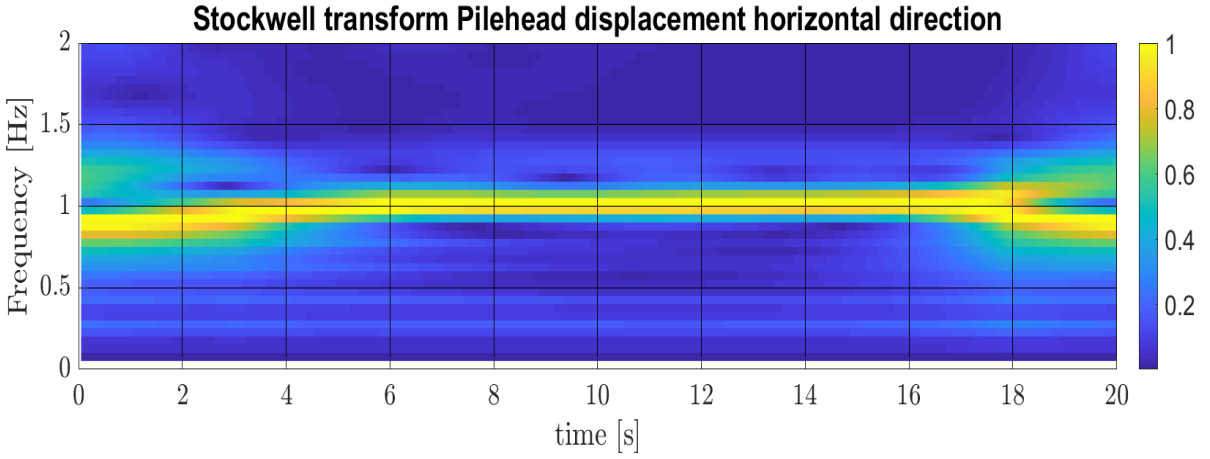

(c) 125 gal

Figure 57: Stockwell transforms of the monopile head displacement in the horizontal direction

What is very interesting to see in the S-transforms of the pile head is how they differ from those of the hub. Instead of the response being dominated by the first mode, one can see higher

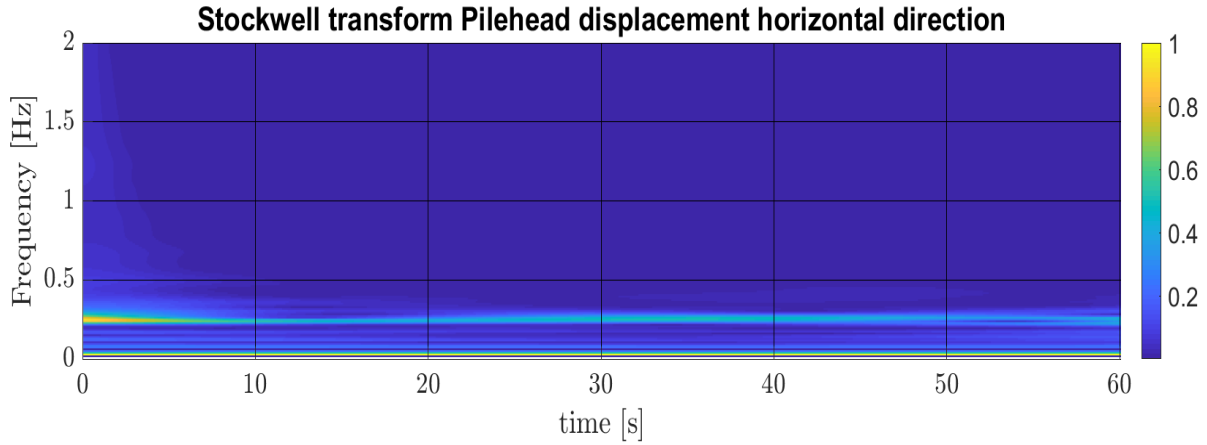

Figure 58: Stockwell transforms of the monopile head displacement in the horizontal direction environmental loading

order modes having a significant impact, especially mode 2 (around 1 Hz). This is explainable by the fact that our system is a cantilever with a big mass lumped at top, and also mass along its height. The mass along its height is composed of the distributed mass of the beams and the lumped masses of the equipment. The further one goes down the beam, the more contribution the higher order modes will have, with the maximum contribution from higher order modes being at the bottom. In a canti-lever like structure, the first mode does not dominate the response at the base, but the response at the top. These findings confirm the soundness of the analysis. Also, in the S-transform of the 125 gal response, one can see that the second mode dominates. This is explainable by the fact that the S-transform of the 125 gal input signal has a lot of its energy concentrated around 1 Hz, so the second mode gets activated in the transfer function. In the Tohoku response, one can see shifts from first mode dominance to second mode dominance (i.e. 15-25 seconds). This is explained by the fact that new waves are arriving at that time periods, with frequency content closer to the second mode of the structure. In the case of the environmental loads, same story as the one for the hub applies. The frequencies there are not close to 1Hz, so there will not be a significant response from the second mode.

7 Conclusions

This study sheds some light on the behaviour of offshore wind turbines under seismic loading in non-liquefiable soils. The conclusions that can be drawn are presented below:

- OWTs are not immune to earthquake loading. Motions of medium to high PGAs can trigger high non linearity in the soil around the monopile head, leading to high displacements;
- SLS wind and wave loads have a close to irrelevant contribution in the presence of a significant ground motion. The ground motion causes much higher forces and displacements at the pile head;
- Including the vertical motion in the analysis leads to higher frequency responses, but not much different in amplitude. Its effects is mostly pronounced on the pore pressure field, but it does not impact horizontal displacements significantly;
- The vertical component of the earthquake can cause high accelerations at the rotor-nacelle assembly, leading to damage to the fine tuned equipment there. Depending on the PGA of

the vertical component, different equipment can be affected. In the case of this study, the generators are affected.

- Earthquakes can lead to high stresses in the tower. Even though yielding might not be reached, buckling should be investigated thoroughly.

- Earthquakes have a strong impact on the pore pressure field around the monopile, leading to shifts in the natural frequency of the system;

- The response of the foundation is not governed by the first mode, higher order modes playing a very significant role. Designing foundations with respect to the first mode will lead to unsatisfactory results.

8 Recommendations

Even though this thesis generated 250 gb of data, there is still a lot of research to be carried on from here. Some of the main suggestions I have are presented below:

- Study the response of OWTs to earthquake loading in liquefiable soils. The soil characteristics used in this thesis have been obtained by matching the recorded and computed response at the top of the borehole considering as input the recorded ground motion at the bottom of the borehole. Even though the results are satisfactory, the matching has been done on a rather "mathematical" basis by playing with the parameters. A standard Manzari Dafias set of soil parameters that has already been calibrated and accepted by the scientific community should be used in the next study, and the relative density of the soil should be alternated in order to analyze different levels of liquefiability;

- Be more selective with the choice of ground motions. For this thesis, the only selection criterion has been PGA. One should try to include ground motions with different frequency contents (Far-field vs Near-field, shallow vs deep, etc.);

- Look into an area where the SLS wind speeds are higher than Offshore Japan in order to decide if those should be considered together with the earthquake when designing the turbine;

- Check steel tower for buckling thoroughly;

- Run a probabilistic analysis over the lifetime of an OWT, using as input seismic data from the region (PGA maps, return periods, etc.). It would be interesting to see if during the lifetime of a turbine, enough strong ground motions could occur that would lead to enough plastic deformation in order for the turbine to be no longer operational. This one is an interesting proposal, but computational time and power would be a big hindrance.

References

Achmus, M., Kuo, Y.-S., Abdel-Rahman, K., 2009. Behavior of monopile foundations under cyclic lateral load. Computers and Geotechnics 36 (5), 725–735.

Anastasopoulos, I., Theofilou, M., 2016. Hybrid foundation for offshore wind turbines: Environmental and seismic loading. Soil Dynamics and Earthquake Engineering 80, 192 – 209.
URL http://www.sciencedirect.com/science/article/pii/S0267726115002559

Andrianopoulos, K. I., Papadimitriou, A. G., Bouckovalas, G. D., 2010. Bounding surface plasticity model for the seismic liquefaction analysis of geostructures. Soil Dynamics and Earthquake Engineering 30 (10), 895–911.

Babuška, I., 1973. The finite element method with Lagrangian multipliers. Numerische Mathematik 20 (3), 179–192.

Bazeos, N., Hatzigeorgiou, G., Hondros, I., Karamaneas, H., Karabalis, D., Beskos, D., 2002. Static, seismic and stability analyses of a prototype wind turbine steel tower. Engineering Structures 24 (8), 1015 – 1025.
URL `http://www.sciencedirect.com/science/article/pii/S0141029602000214`

Been, K., Jefferies, M., 1985. A state parameter for sands. Géotechnique 35 (2), 99–112.

Borja, R., Amies, A., 1994. Multiaxial cyclic plasticity model for clays. Journal of Geotechnical Engineering 120 (6), 1051–1070.

Brezzi, F., 1974. On the existence, uniqueness and approximation of saddle-point problems arising from Lagrangian multipliers. Revue française d'automatique, informatique, recherche opérationnelle. Analyse numérique 8 (2), 129–151.

Carlson, N. N., Miller, K., 1998. Design and application of a gradient-weighted moving finite element code. SIAM Journal on Scientific Computing 19 (3), 728–798.

Chopra, A. K., 1995. Dynamics of Structures. Vol. 3. Prentice Hall New Jersey.

Corciulo, S., Zanoli, O., Pisanò, F., 2017. Transient response of offshore wind turbines on monopiles in sand: role of cyclic hydro–mechanical soil behaviour. Computers and Geotechnics 83, 221–238.

Corti, R., Diambra, A., Wood, D. M., Escribano, D. E., Nash, D. F., 2016. Memory surface hardening model for granular soils under repeated loading conditions. Journal of Engineering Mechanics 142 (12), 04016102.

Cuéllar, P., Mira, P., Pastor, M., Fernández-Merodo, J. A., Baeßler, M., Rücker, W., 2014. A numerical model for the transient analysis of offshore foundations under cyclic loading. Computers and Geotechnics 59, 75–86.

Dafalias, Y., Taiebat, M., 2016. Sanisand-z: zero elastic range sand plasticity model. Geotechnique 66 (12), 999–1013.

Dafalias, Y. F., Manzari, M. T., 2004. Simple plasticity sand model accounting for fabric change effects. Journal of Engineering mechanics 130 (6), 622–634.

Dafalias, Y. F., Manzari, M. T., Papadimitriou, A. G., 2006. SANICLAY: simple anisotropic clay plasticity model. International Journal for Numerical and Analytical Methods in Geomechanics 30 (12), 1231–1257.

Damgaard, M., Zania, V., Andersen, L., Ibsen, L., 2014. Effects of soilstructure interaction on real time dynamic response of offshore wind turbines on monopiles. Engineering Structures 75, 388–401.

De Borst, R., Crisfield, M. A., Remmers, J. J., Verhoosel, C. V., 2012. Nonlinear finite element analysis of solids and structures. John Wiley & Sons.

di Prisco, C. G., Wood, D. M., 2012. Mechanical Behaviour of Soils Under Environmentally-Induced Cyclic Loads. Springer.

Dueas-Osorio, L., Basu, B., 2008. Unavailability of wind turbines due to wind-induced accelerations. Engineering Structures 30 (4), 885 – 893.
URL http://www.sciencedirect.com/science/article/pii/S0141029607002027

Elgamal, A., Yang, Z., Parra, E., Ragheb, A., 2003. Modeling of cyclic mobility in saturated cohesionless soils. International Journal of Plasticity 19 (6), 883–905.

En, B., 1991. 1-4: 2005 eurocode 1: Actions on structuresgeneral actionswind actions.

Evans, M. D., Zhou, S., 1995. Liquefaction behavior of sand-gravel composites. Journal of Geotechnical Engineering 121 (3), 287–298.

Gajo, A., Wood, D. M., 1999. A kinematic hardening consitutive model for sands: the multiaxial formulation. International Journal for Numerical and Analytical methods in Geomechanics 23, 925 – 965.

Goodman, R. E., Taylor, R. L., Brekke, T. L., 1968. A model for the mechanics of jointed rock. Journal of Soil Mechanics & Foundations Division 94 (3), 637–659.

Griffiths, D. V., 1985. Numerical modeling of interfaces using conventional finite elements. In: Proceedings of 5th International Conference on Numerical Methods in Geomechanics. Nagoya, Japan. pp. 837–844.

Helnwein, P., 2001. Some remarks on the compressed matrix representation of symmetric second-order and fourth-order tensors. Computer methods in applied mechanics and engineering 190 (22), 2753–2770.

Houlsby, G. T., Mortara, G., 2004. A continuous hyperplasticity model for sands under cyclic loading. In: Proceedings of the International Conference on Cyclic Behaviour of Soils and Liquefaction Phenomena. Bochum, Germany. Vol. 31. pp. 21–26.

Huang, M., Yue, Z. Q., Tham, L. G., Zienkiewicz, O. C., September 2004. On the stable finite element procedures for dynamic problems of saturated porous media. International Journal for Numerical Methods in Engineering 61 (9), 1421–1450.

Hughes, T. J. R., 1987. The Finite Element Method: linear static and dynamic finite element analysis. Prentice-Hall.

Ishihara, K., Tatsuoka, F., Yasuda, S., 1975. Undrained deformation and liquefaction of sand under cyclic stresses. Soils and Foundations - Japanese Society of Soil Mechanics and Foundation Engineering 15 (1), 29–44.

Jeremić, B., Cheng, Z., Taiebat, M., Dafalias, Y. F., 2008. Numerical simulation of fully saturated porous materials. International Journal for Numerical and Analytical Methods in Geomechanics 32 (13), 1635–1660.

Jeremić, B., Jie, G., Preisig, M., Tafazzoli, N., 2009. Time domain simulation of soil–foundation–structure interaction in non–uniform soils. Earthquake Engineering and Structural Dynamics 38 (5), 699–718.

Katsanos, E. I., Thns, S., Georgakis, C. ., 2016. Wind turbines and seismic hazard: a state-of-the-art review. Wind Energy 19 (11), 2113–2133.
URL https://onlinelibrary.wiley.com/doi/abs/10.1002/we.1968

Kaynia, A. M., 2018. Seismic considerations in design of offshore wind turbines. Soil Dynamics and Earthquake Engineering.
URL http://www.sciencedirect.com/science/article/pii/S0267726117309363

Kementzetzidis, E., 2017. Geotechnical Aspects of Offshore Wind Turbine Dynamics Emerging from 3D Sand-Monopile Non-Linear Simulations.

Kiyomiya, O., Rikiji, T., Van Gelder, P., 2002. Dynamic response analysis of onshore wind energy power units during earthquakes and wind. In: Chung, J., Sayed, M., Kashiwagi, M., Setoguchi, T., Hong, S. (Eds.), Proceedings of the International Offshore and Polar Engineering Conference. Vol. 12. pp. 520–526.

Kjørlaug, R., 2013. Seismic Response of Wind Turbines. Ph.D. thesis, Norwegian University of Science and Technology.

Kourkoulis, R., Lekkakis, P., Gelagoti, F., Kaynia, A., 2014. Suction caisson foundations for offshore wind turbines subjected to wave and earthquake loading: effect of soilfoundation interface. Gotechnique 64 (3), 171–185.
URL `https://doi.org/10.1680/geot.12.P.179`

Kramer, S., Sideras, S., Greenfield, M., 2016. The timing of liquefaction and its utility in liquefaction hazard evaluation. Soil Dynamics and Earthquake Engineering 91, 133–146.

Leblanc, C., Tarp-Johansen, N. J., 2010. Monopiles in sand. stiffness and damping.

Li, X., Dafalias, Y. F., 2000. Dilatancy for cohesionless soils. Geotechnique 50 (4), 449–460.

Lombardi, D., Bhattacharya, S., Wood, D. M., 2013. Dynamic soilstructure interaction of monopile supported wind turbines in cohesive soil. Soil Dynamics and Earthquake Engineering 49, 165 – 180.
URL `http://www.sciencedirect.com/science/article/pii/S0267726113000171`

López-Querol, S., Fernández-Merodo, J. A., Mira, P., Pastor, M., 2008. Numerical modelling of dynamic consolidation on granular soils. International journal for numerical and analytical methods in geomechanics 32 (12), 1431–1457.

Manzari, M. T., Dafalias, Y. F., 1997. A critical state two-surface plasticity model for sands. Geotechnique 47 (2), 255–272.

McGann, C. R., Arduino, P., Mackenzie-Helnwein, P., 2012. Stabilized single-point 4-node quadrilateral element for dynamic analysis of fluid saturated porous media. Acta Geotechnica 7 (4), 297–311.

McGann, C. R., Arduino, P., Mackenzie-Helnwein, P., 2015. A stabilized single-point finite element formulation for three-dimensional dynamic analysis of saturated soils. Computers and Geotechnics 66, 126–141.

Mróz, Z., Norris, V. A., Zienkiewicz, O. C., 1978. An anisotropic hardening model for soils and its application to cyclic loading. International Journal for Numerical and Analytical Methods in Geomechanics 2, 203–221.

Nasser, S., 1980. On behavior of granular materials in simple shear. SOILS AND FOUNDATIONS 20 (3), 59–73.

Nemat-Nasser, S., Tobita, Y., 1982. Influence of fabric on liquefaction and densification potential of cohesionless sand. Mechanics of Materials 1 (1), 43 – 62.
URL `http://www.sciencedirect.com/science/article/pii/0167663682900230`

Newman, J. N., 1977. Marine hydrodynamics. MIT press.

Newmark, N. M., 1959. A method of computation for structural dynamics. ASCE Journal of Engineering Mechanics Division 85 (3), 67–94.

Papadimitriou, A. G., Bouckovalas, G. D., 2002. Plasticity model for sand under small and large cyclic strains: a multiaxial formulation. Soil Dynamics and Earthquake Engineering 22 (3), 191–204.

Pastor, M., Zienkiewicz, O. C., Leung, K. H., 1985. Simple model for transient soil loading in earthquake analysis. II: Non-associative models for sands. International journal for numerical and analytical methods in geomechanics 9 (5), 477–498.

Pastor, M., Zienkiewicz, O. C., Li, T., Xiaoqing, L., Huang, M., 1999. Stabilized finite elements with equal order of interpolation for soil dynamics problems. Archives of Computational Methods in Engineering 6 (1), 3–33.

Pisanò, F., Jeremić, B., 2014. Simulating stiffness degradation and damping in soils via a simple visco-elastic–plastic model. Soil Dynamics and Earthquake Engineering 63, 98–109.

Preisig, M., Prévost, J. H., 2011. Stabilization procedures in coupled poromechanics problems: A critical assessment. International Journal for Numerical and Analytical Methods in Geomechanics 35 (11), 1207–1225.

Prévost, J. H., 1985. A simple plasticity theory for frictional cohesionless soils. International Journal of Soil Dynamics and Earthquake Engineering 4 (1), 9–17.

Prévost, J. H., Popescu, R., October 1996. Constitutive relations for soil materials. Electronic Journal of Geotechnical Engineering.

Puzrin, A. M., Houlsby, G. T., 2001. Fundamentals of kinematic hardening hyperplasticity. International journal of solids and structures 38 (21), 3771–3794.

Risi, R. D., Bhattacharya, S., Goda, K., 2018. Seismic performance assessment of monopile-supported offshore wind turbines using unscaled natural earthquake records. Soil Dynamics and Earthquake Engineering 109, 154 – 172.
URL http://www.sciencedirect.com/science/article/pii/S0267726117309454

Roten, D., Fah, D., Bonilla, L., 12 2014. Quantification of cyclic mobility parameters in liquefiable soils from inversion of vertical array records. Bulletin of the Seismological Society of America 104, 3115–3138.

Scott, M. H., Fenves, G. L., 2003. A Krylov subspace accelerated Newton algorithm. In: Proceedings of 2003 ASCE Structures Congress. Seattle, Washington, USA.

Seidalinov, G., Taiebat, M., 2014. Bounding surface SANICLAY plasticity model for cyclic clay behavior. International Journal for Numerical and Analytical Methods in Geomechanics 38 (7), 702–724.

Shirzadeh, R., Devriendt, C., Bidakhvidi, M. A., Guillaume, P., 2013. Experimental and computational damping estimation of an offshore wind turbine on a monopile foundation. Journal of Wind Engineering and Industrial Aerodynamics 120, 96–106.

Sloan, S. W., 1987. Substepping schemes for the numerical integration of elastoplastic stress–strain relations. International Journal for Numerical Methods in Engineering 24 (5), 893–911.

Stockwell, R. G., Mansinha, L., Lowe, R., 1996. Localization of the complex spectrum: the s transform. IEEE transactions on signal processing 44 (4), 998–1001.

Taborda, D. M. G., Zdravković, L., Kontoe, S., Potts, D. M., 2014. Computational study on the modification of a bounding surface plasticity model for sands. Computers and Geotechnics 59, 145–160.

Taiebat, M., Dafalias, Y. F., 2008. SANISAND: Simple anisotropic sand plasticity model. International Journal for Numerical and Analytical Methods in Geomechanics 32 (8), 915–948.

Tarp-Johansen, N. J., Andersen, L., Christensen, E. D., Mørch, C., Frandsen, S., Kallesøe, B., 2009. Comparing sources of damping of cross-wind motion. In: The European Offshore Wind Conference & Exhibition. The European Wind Energy Association.

Tasiopoulou, P., Gerolymos, N., 2016. Constitutive modeling of sand: Formulation of a new plasticity approach. Soil Dynamics and Earthquake Engineering 82, 205–221.

Tatsuoka, F., Ishihara, K., 1974. Drained deformation of sand under cyclic stresses reversing direction. Soils and Foundations - Japanese Society of Soil Mechanics and Foundation Engineering 14 (3), 51–65.

Tsuchiya, M., Ishihara, T., Fukumoto, Y., 01 2006. The wind observation on the pacific ocean for offshore wind farm.

Valamanesh, V., Myers, A., 2014a. Aerodynamic damping and seismic response of horizontal axis wind turbine towers. Journal of Structural Engineering 140 (11), 04014090.

Valamanesh, V., Myers, A. T., 2014b. Aerodynamic damping and seismic response of horizontal axis wind turbine towers. Journal of Structural Engineering 140 (11), 04014090.
URL https://ascelibrary.org/doi/abs/10.1061/%28ASCE%29ST.1943-541X.0001018

Wang, Z.-L., Dafalias, Y. F., Shen, C.-K., 1990. Bounding surface hypoplasticity model for sand. Journal of engineering mechanics 116 (5), 983–1001.

Watanabe, K., Pisanò, F., Jeremić, B., 2016. Discretization effects in the finite element simulation of seismic waves in elastic and elastic-plastic media. Engineering with Computers, 1–27.
URL http://dx.doi.org/10.1007/s00366-016-0488-4

WindEnergie, G. L., 2005. Guideline for the certification of offshore wind turbines. Germanischer Lloyd Rules and Guidelines, IVIndustrial Services, Part.

Witcher, D., 2005. Seismic analysis of wind turbines in the time domain. Wind Energy 8 (1), 81–91.
URL https://onlinelibrary.wiley.com/doi/abs/10.1002/we.135

Wood, D. M., Belkheir, K., Liu, D. F., 1994. Strain softening and state parameter for sand modelling. Géotechnique 44 (2), 335–339.

Yang, Z., Elgamal, A., 2008. Multi-surface cyclic plasticity sand model with Lode angle effect. Geotechnical and Geological Engineering 26 (3), 335–348.

Zahmatkesh, A., Janalizadeh Choobbasti, A., 2017. Calibration of an advanced constitutive model for babolsar sand accompanied by liquefaction analysis. Journal of Earthquake Engineering 21 (4), 679–699.

Zhang, Y., Pedroso, D. M., Li, L., 2016. FDM and FEM solutions to linear dynamics of porous media: stabilised, monolithic and fractional schemes. International Journal for Numerical Methods in Engineering.

Zienkiewicz, O. C., Best, B., Dullage, C., Stagg, K. G., 1970. Analysis of non-linear problems in Rock Mechanics with particular reference to jointed rock systems. In: Proceedings of 2nd Congress of the International Society for Rock Mechanics. Belgrad, Yugoslavia. pp. 501–509.

Zienkiewicz, O. C., Chan, A. H. C., Pastor, M., Schrefler, B. A., Shiomi, T., 1999. Computational geomechanics. Wiley Chichester.

Zienkiewicz, O. C., Chang, C. T., Bettess, P., 1980. Drained, undrained, consolidating and dynamic behaviour assumptions in soils. Géotechnique 30 (4), 385–395.

Zienkiewicz, O. C., Leung, K. H., Pastor, M., 1985. Simple model for transient soil loading in earthquake analysis. I. Basic model and its application. International Journal for Numerical and Analytical Methods in Geomechanics 9 (5), 453–476.

Zienkiewicz, O. C., Shiomi, T., 1984. Dynamic behaviour of saturated porous media; the generalized Biot formulation and its numerical solution. International Journal for Numerical and Analytical Methods in Geomechanics 8 (1), 71–96.

Zienkiewicz, O. C., Taylor, R. L., 2000. The Finite Element Method. Volume 1: The Basis, 5th Edition. Butterworth-Heinemann.

A Appendix

A.1 Vertical acceleration hub

As mentioned in Section 1, vertical accelerations at hub can cause damage to the fine tuned equipment located there. According to Dueas-Osorio and Basu (2008) there is evidence from the field of earthquake engineering that the functionality of industrial equipment can be impaired by moderate to high accelerations.

For instance, the functionality of generators can be affected in the range $5 - 10m/s^2$, inverters in the range $10 - 15m/s^2$, and electrical controls in the range $15 - 20m/s^2$.

In Figure 59, one can see that the vertical acceleration in the case of the Tohoku ground motion peaks around $8m/s^2$, therefore the generators might experience damage. In the case of stronger ground motions, the accelerations can be higher, thus being dangerous to other equipment as well.

In conclusion, vertical accelerations at the hub induced by ground motion pose a realistic threat to the fine tuned equipment located there.

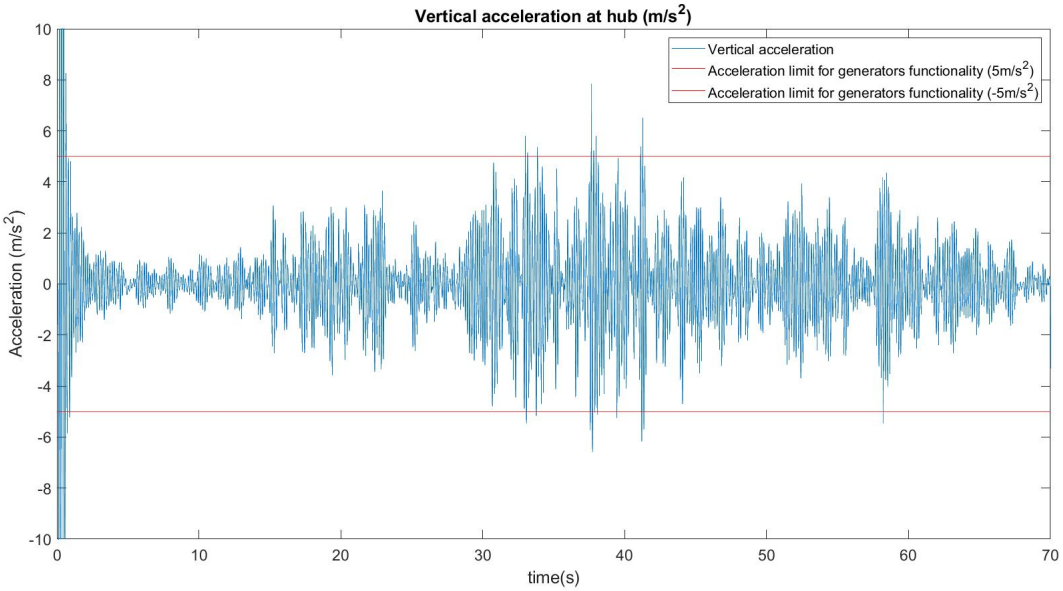

Figure 59: Vertical acceleration hub Tohoku

A.2 Moment capacity

It is worth checking if the Tohoku ground motion would be able to trigger yielding in the steel tower. For this, the bending moment capacity of the tower has been compared with the actual moment induced by the ground motion. Due to the variable sections along the height of the tower, the plastic moment capacity has been calculated in each of those with the following equation:

$$\begin{aligned} M_p &= Sfy \\ S &= \frac{4(R^3 - r^3)}{3} \end{aligned} \tag{22}$$

where S is the plastic section modulus, f_y is the yield stress of steel taken as $355N/mm^2$, R is the external radius and r is the internal radius of the section.

According to Figure 60, the capacity is significantly higher than the demand towards the base, where the section is the biggest. As expected, with the decrease in section size, the capacity gets smaller and smaller towards the hub, the factor of safety being low as the hub is being approached. Another interesting thing to highlight is the shape of the moment diagram. For a classical cantilever structure, one would expect this to have a more "triangular shape", but due to this being a multi degree of freedom system with lumped masses along its height, the shape is different.

Even though the moment capacity is satisfied, one should take into account that steel structures generally fail due to buckling before reaching their ultimate capacity in bending. A buckling check should be done, as compressive forces in the system are very high due to the high mass of the system, especially the dominant mass on top, acting together with the downwards component of the vertical seismic motion. This combination of effects leads to very high compressive forces in the tower.

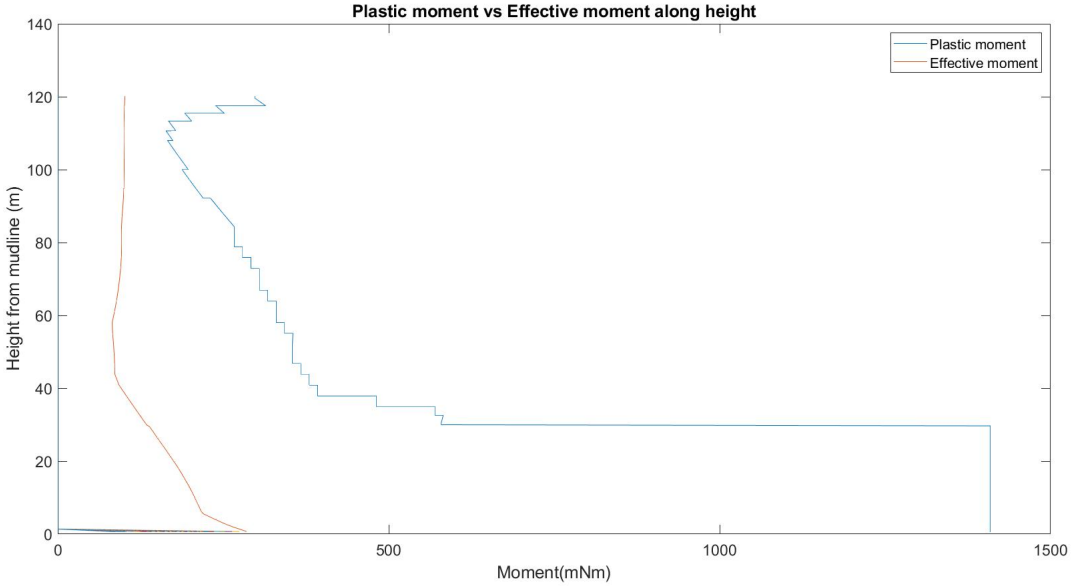

Figure 60: Effective vs plastic moment along tower height